Semiclassical Time Propagation and the Raman Spectrum of Periodic Systems

Citation

Permanent link

Terms of Use

Share Your Story

Semiclassical Time Propagation and the Raman Spectrum of Periodic Systems

A dissertation presented

by

Lucas Kocia

to

The Department of Chemistry and Chemical Biology

in partial fulfillment of the requirements

for the degree of

Doctor of Philosophy

in the subject of

Chemical Physics

Harvard University

Cambridge, Massachusetts

April 2016

Dissertation Advisor: Professor Eric J. Heller   Lucas Kocia

Semiclassical Time Propagation and the Raman Spectrum of Periodic Systems

Abstract

The first half of this thesis introduces the time-dependent W.K.B. approximation of quantum mechanics from basic principles in classical and quantum mechanics. After discussing the van Vleck-Morette-Gutzwiller propagator, the real-trajectory time-dependent W.K.B. approximation of a coherent state is introduced. This is also called the off-center "thawed" Gaussian approximation and has a closed-form solution consisting of a Gaussian with time-dependent position and momentum, dispersion, and position-momentum correlation. This result is then extended to third order in the classical action of guiding real trajectories - a parabolization in phase space, and equivalently, a uniformization over two saddle points - allowing for the novel treatment of non-linearity in its underlying classical dynamics. The result is another simple closed-form solution, but this time made up of Airy functions and their derivatives multiplied by an exponential. Unlike the lower-order treatment, which stopped at linearization of phase space, this expression is able to capture global as well as local non-linear dynamics at finite Planck's constant.

We then proceed to discuss another uniformization of the semiclassical primitive propagator: the Heller-Herman-Kluk-Kay (H.H.K.K.) propagator. The H.H.K.K. involves an integral over all of phase space which can be trimmed down to only a one-dimensional integral, regardless of the dimensions of the system, by appealing to similar guiding manifold techniques discussed in the previous section. This is the basis for the directed H.H.K.K. propagator which we investigate. Though many possibilities for speeding up the semiclassical evaluation of H.H.K.K. been examined over the years, few have focused on using the actual dynamics of underlying trajectories to simplify its computation. Our findings offer encouraging evidence about the promise of this direction.

The second half of this thesis is concerned with describing the Raman spectrum of graphene within the Born-Oppenheimer approximation using the Kramers-Heisenberg-Dirac (K.H.D.) formalism. The electronic and vibrational properties of graphene are introduced, along with simple tight-binding methods of calculating them. With these tools, K.H.D. is then applied to explain the origin of the unique and few prominent peaks in graphene's Raman spectrum. Here, the dominant

effect of graphene's linear Dirac cone in its electronic dispersion is easily seen. The latter leads to novel electron-light-phonon "sliding transitions" that explain the brightness of the overtone 2D peak.

Finally, some more minor results on the subject of the asymptotic zeros of orthogonal polynomials are presented.

Contents

1 Acknowledgments

I would like to thank Rick, for being a phenomenal adviser and teacher; Heller Group members, with whom I enjoyed and learned so much working with: Anna Klales, Byron Drury, Yuan Yang, Matt Schram and Suzanne Pittman; my parents, sister, family and friends for putting up with me from the get-go; and Alyssa Wilson for putting up with me now.

2 Publications

This thesis is based on the following publications:

Lucas Kocia, Anna Klales. "Semiclassical Treatment of Quantum Propagation with Non-Linear Classical Dynamics: A Third Order Thawed Gaussian Approximation" [In preparation].

Heller, E.J., Yang, Y., Kocia, L., Chen, W., Fang, S., Borunda, M. and Kaxiras, E. "Theory of Graphene Raman Scattering." ACS nano. 10.2 (2016): 2803–2818.

Kocia, Lucas, and Eric J. Heller. "Directed HK propagator." The Journal of Chemical Physics 143.12 (2015): 124102.

Kocia, Lucas. "Asymptotic Equation for Zeros of Hermite Polynomials from the Holstein-Primakoff Representation." arXiv preprint arXiv:1506.00541 (2015).

Heller, Eric J., Yuan Yang, and Lucas Kocia. "Raman Scattering in Carbon Nanosystems: Solving Polyacetylene." ACS Central Science 1.1 (2015): 40-49.

Kocia, Lucas, and Eric J. Heller. "Communication: HK propagator uniformized along a one-dimensional manifold in weakly anharmonic systems." The Journal of Chemical Physics 141.18 (2014): 181102.

Kocia, Lucas, and Eric J. Heller. "Generalized dephasing relation for fidelity and application as an efficient propagator." The Journal of Chemical Physics 139.12 (2013): 124110.

3 Introduction

This thesis is broadly split into two main sections: 1. semiclassical time propagation, and 2. Raman spectra of extended periodic 1d and 2d systems within the Born-Oppenheimer approximation.

The overarching subject joining these disparate fields is classical and quantum mechanics.

4   An Introduction into Semiclassical Time Propagation

In this chapter, we largely follow Tannor's *Introduction to Quantum Mechanics A Time-Dependent Perspective*[1] as well as my advisor Rick Heller's as-yet unpublished book, provisionally titled *The Semiclassical Way to Dynamics and Spectroscopy*.

4.1   Lagrangian Mechanics

We posit that our system is characterized by its position $\boldsymbol{q}(t)$ and velocity $\dot{\boldsymbol{q}}(t)$. We assume that the two contribute to our system's dynamics in a separable manner, and we call such a system "mechanical":

$$L = T(\dot{\boldsymbol{q}}) - V(\boldsymbol{q}). \tag{4.1}$$

$$\frac{\mathrm{d}}{\mathrm{d}t}\left(\frac{\partial L}{\partial \dot{\boldsymbol{q}}}\right) - \frac{\partial L}{\partial \boldsymbol{q}} = 0. \tag{4.2}$$

When $T = m\frac{\dot{\boldsymbol{q}}^2}{2}$, Lagrange's equations reduce to

$$m\frac{\mathrm{d}^2\boldsymbol{q}}{\mathrm{d}t^2} = -\frac{\partial V}{\partial \boldsymbol{q}}. \tag{4.3}$$

These are Newton's equations.

Notice that $\boldsymbol{q}(t)$ and $\dot{\boldsymbol{q}}(t)$ are explicitly dependent on the time t and $L(\dot{\boldsymbol{q}}, \boldsymbol{q}, t)$ is explicitly dependent on $\boldsymbol{q}$ and $\dot{\boldsymbol{q}}$. It may also be explicitly dependent on t if, for instance $V(\boldsymbol{q}, t)$ is explicitly dependent on t. Importantly, $L(\dot{\boldsymbol{q}}, \boldsymbol{q}, t)$ is also *implictly* dependent on t too since $\boldsymbol{q}(t)$ and $\dot{\boldsymbol{q}}(t)$ are explicitly dependent on t. Thus,

$$\frac{\mathrm{d}L}{\mathrm{d}t} = \frac{\partial L}{\partial t} + \frac{\partial L}{\partial \boldsymbol{q}}\dot{\boldsymbol{q}} + \frac{\partial L}{\partial \dot{\boldsymbol{q}}}\ddot{\boldsymbol{q}}. \tag{4.4}$$

4.2 Hamiltonian Mechanics

We perform a Lagrange transformation to obtain the Hamiltonian:

$$H = \frac{\partial L}{\partial \dot{\boldsymbol{q}}} \cdot \dot{\boldsymbol{q}} - L, \tag{4.5}$$

where $\frac{\partial L}{\partial \dot{q}} \equiv \boldsymbol{p}$.

We have thus replaced our velocity $\dot{\boldsymbol{q}}$ with momentum $\boldsymbol{p}$. Instead of a second-order partial differential equation of motion, we now have two first-order ordinary differential equations of motion:

$$\frac{\mathrm{d}\boldsymbol{x}}{\mathrm{d}t} = \boldsymbol{\Lambda} \cdot \boldsymbol{x}, \tag{4.6}$$

where

$$\boldsymbol{\Lambda} = \begin{pmatrix} 0 & -\mathbb{I}_{N \times N} \\ \mathbb{I}_{N \times N} & 0 \end{pmatrix} \tag{4.7}$$

and

$$\boldsymbol{x} = \begin{pmatrix} \boldsymbol{p} \\ \boldsymbol{q} \end{pmatrix}, \tag{4.8}$$

for $\boldsymbol{p}, \boldsymbol{q} \in \mathbb{R}^N$. $\boldsymbol{\Lambda}$ is the symplectic matrix and it defines the dynamics of $\boldsymbol{p}$ and $\boldsymbol{q}$; Hamiltonian dynamics are a symplectic - and relatedly, area preserving - transformation.

4.2.1 Principal Functions

The action

$$S(\boldsymbol{q}, t) \equiv S[\boldsymbol{q}(t)](q_t, q_0, t) = \int_0^t \mathrm{d}t' L(\boldsymbol{q}(t), \dot{\boldsymbol{q}}(t), t'). \tag{4.9}$$

Our short-form sets $q_t = q$ and $q_0 = 0$ (the latter we don't bother showing in our function arguments).

Hamilton's principal function

$$R(q, E) \equiv R[q(t)](q_E, q_0, E) = \int_0^E \mathrm{d}E' L(\boldsymbol{q}(t), \dot{\boldsymbol{q}}(t), E'). \tag{4.10}$$

4.2.2 Variations of the Principal Functions

To find classical trajectories, we solve for the solutions $q(t)$ of

$$\delta S(\boldsymbol{q}, t)|_{\boldsymbol{q}(t)} = 0. \tag{4.11}$$

This is equivalent to Lagrange's equations of motion and to Hamilton's equations.

It is also often useful to know

$$\boldsymbol{p}_t = \left. \frac{\partial S}{\partial \boldsymbol{q}_t} \right|_{\boldsymbol{q}_0, t}, \tag{4.12}$$

$$-\boldsymbol{p}_0 = \left. \frac{\partial S}{\partial \boldsymbol{q}_0} \right|_{\boldsymbol{q}_t, t}, \tag{4.13}$$

and

$$- E = \left. \frac{\partial S}{\partial t} \right|_{\boldsymbol{q}_0, \boldsymbol{q}_t}. \tag{4.14}$$

3

4.3 Propagators

4.3.1 Feynman Propagator

Propagating quantum states in time requires finding their Green's functions. The path integral formulation of the Green's function in quantum mechanics is called the Feynman propagator and is:

$$\langle q' | e^{-i\frac{Ht}{\hbar}} | q \rangle = \left(\frac{m}{2\pi i \hbar t} \right)^{1/2} \int \mathcal{D}[q(t)] e^{i\frac{S(q,q',t)}{\hbar}}. \tag{4.15}$$

This expression involves a functional integral over all pathways, be they classical or "virtual", between q' and q in time t. A cartoon of such paths is shown in Figure 4.1. Classical paths make up a set of measure zero of all the paths that must be considered therein.

Feynman Propagator Applied to the Harmonic Oscillator Hamiltonian
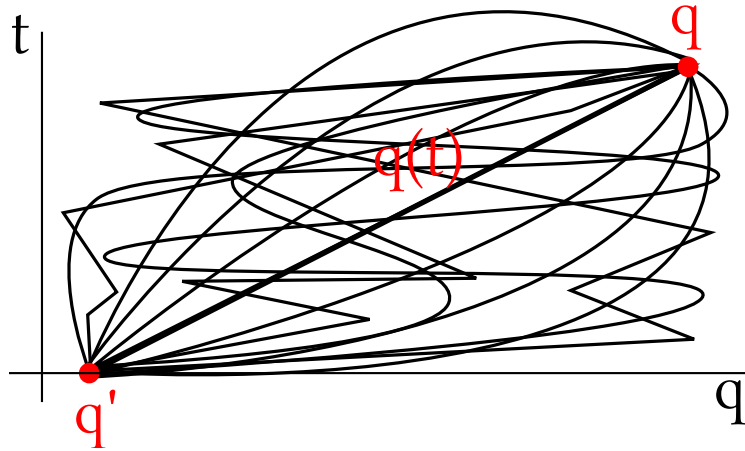
Figure 4.1: Examples of paths between q' and q in time t that must be included in the path integral of Eq. 4.15.

For a harmonic oscillator,

$$\langle q | e^{-iHt} | q' \rangle = \sqrt{\frac{m\omega}{2\pi i \sin \omega t}} \exp \left[\frac{im\omega}{2} \frac{(q^2 + q'^2) \cos \omega t - 2qq'}{\sin \omega t} \right].$$

4

For $m = \omega = 1$ and $q' = 1$ Figure 4.2 shows one period of motion from this formula.
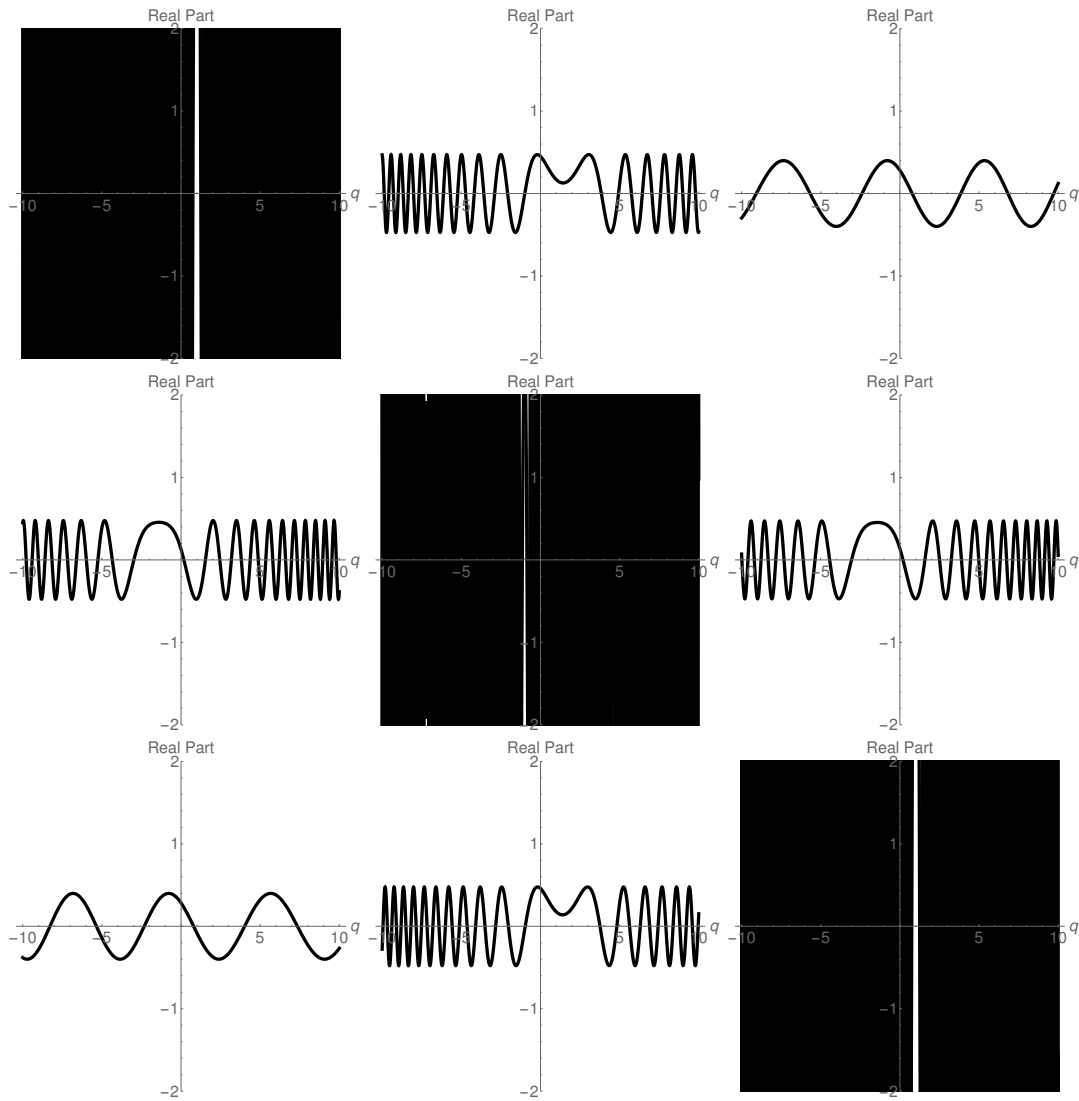
Figure 4.2: $t = 0, \frac{\pi}{4}, \frac{\pi}{2}, \ldots, \frac{8\pi}{4}$.

This has a very nice correspondence to the evolution of a completely classical position manifold q' in phase space. Figure 4.3 shows how such a manifold looks during the first half of its orbit. Since it is exactly known in q-space, it is completely undetermined in p-space, which agrees with the quantum uncertainty principle or Fourier relations.
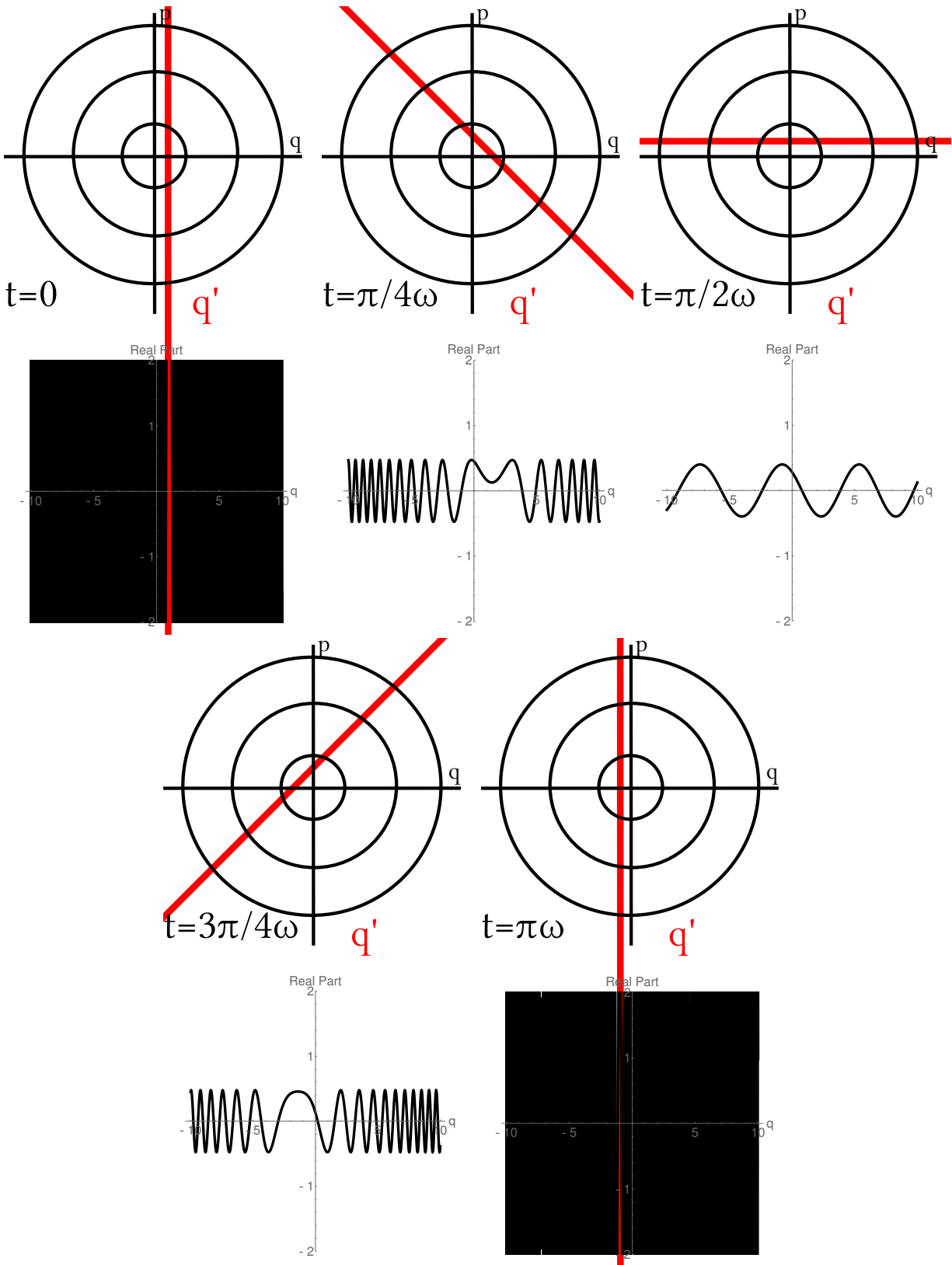
Figure 4.3: $t = 0, \frac{\pi}{4}, \frac{\pi}{2}, \frac{3\pi}{4}, \frac{8\pi}{4}$.

7

It can be shown that the prefactor of this expression is proportional to the classical overlap of the intersection between the q and q' manifolds. Also, the phase of this propagator is equal to the classical action of the harmonic oscillator. Figure 4.4 shows a cartoon of this correspondence. This suggests that a (semi-)classical analog to the quantum propagator might exist that only depends on classical paths.
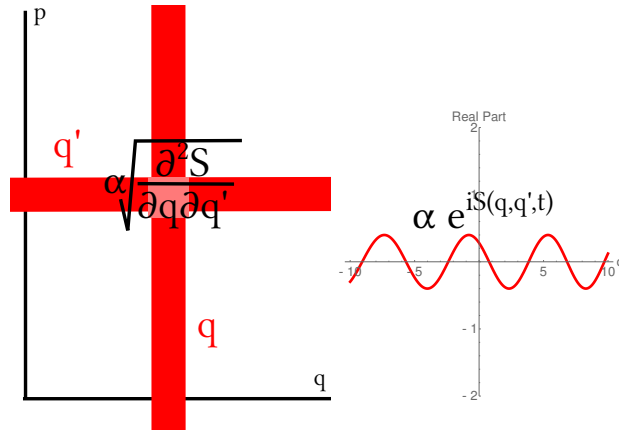
Figure 4.4:

It turns out that, up to order $\hbar^2$, this correspondence is exact for all Hamiltonians and other representations of the propagator (other than the position state representation).

Feynman Propagator Applied to a Coherent State

Let our initial state be a coherent state:

$$\Psi_\beta(q,t) = \sqrt[4]{\frac{2}{\pi\sigma^2}} \exp\left[ip_\beta\left(q - q_\beta\right) - \frac{1}{\sigma^2}\left(q - q_\beta\right)^2\right], \tag{4.16}$$

where $\sigma \in \mathbb{R} > 0$ is proportional to the spread in position space, p_β is its central momentum, q_β is its central position.

This state will be dealt with more formally at the end of this chapter. We choose to examine its propagation right now for the simple reason that it is easier to visualize in phase space since it is localized in both p and q.
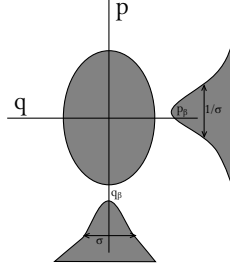
Figure 4.5: A coherent state in phase space and projected onto position and momentum space.

Applying the Feynman propagator to this state produces:

$$
\int_{-\infty}^{\infty} \mathrm{d}q' \, \langle q | e^{-iHt} | q' \rangle \, \langle q' | \Psi_\beta \rangle \tag{4.17}
$$

$$
= \frac{\sqrt{-im\omega \csc(t\omega)} \exp\left(\frac{-i\sigma^2\left(m^2q^2\omega^2 + \mathrm{p}\beta^2\right) - 2m\omega\cot(t\omega)\left(q^2 + \mathrm{q}\beta\left(\mathrm{q}\beta + i\mathrm{p}\beta\sigma^2\right)\right) + 2mq\omega\left(2\mathrm{q}\beta + i\mathrm{p}\beta\sigma^2\right)\csc(t\omega)}{2m\sigma^2\omega\cot(t\omega) + 4i}\right)}{\sqrt{\frac{2}{\sigma^2} - im\omega\cot(t\omega)}}.
$$

For $m = \omega = \sigma = 1$ and $(p_\beta, q_\beta) = (0, 1)$ Figure 4.6 shows one period of motion from this formula.

Figure 4.6: $t = 0, \frac{\pi}{4}, \frac{\pi}{2}, \ldots, \frac{8\pi}{4}$.

10
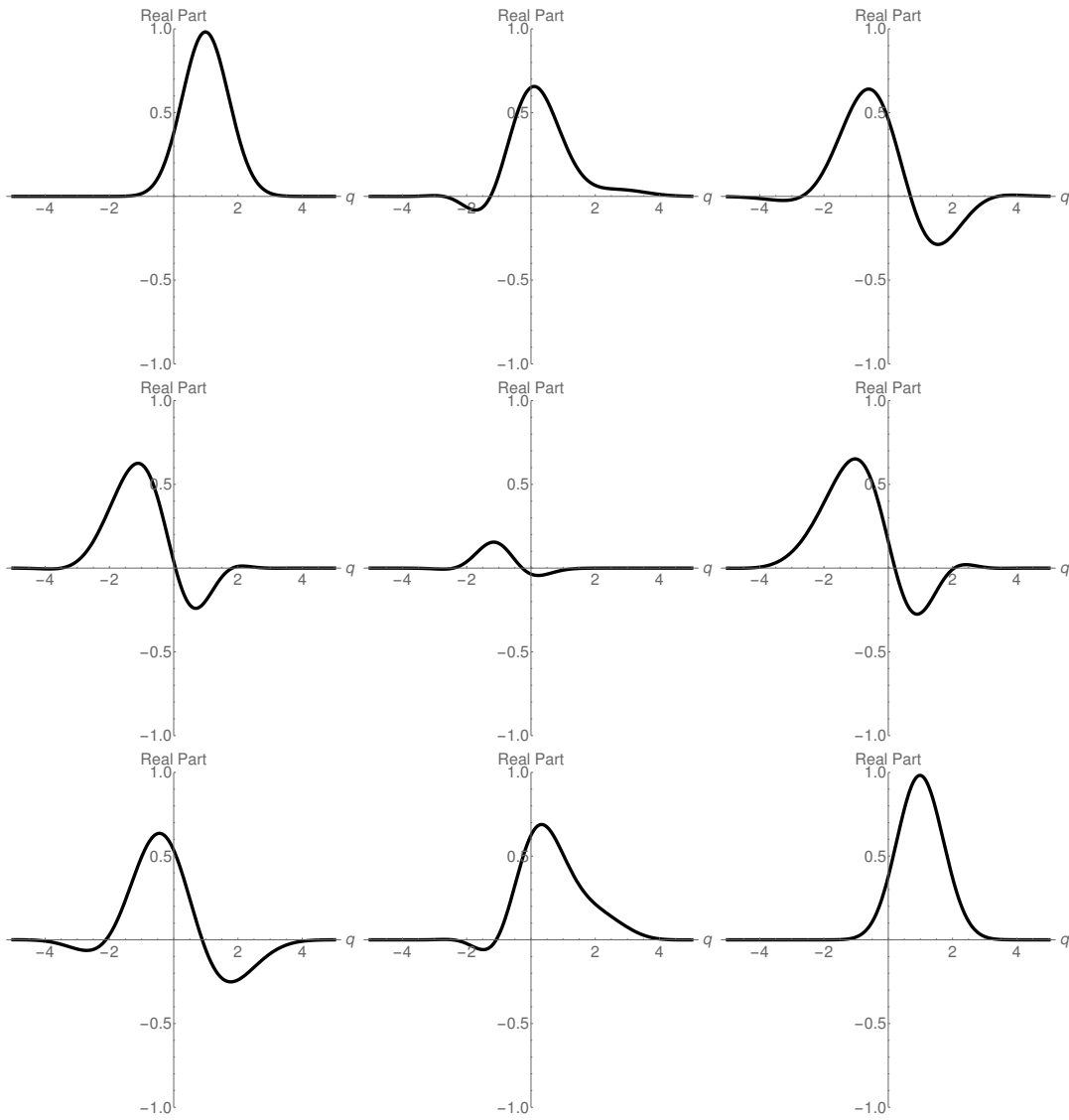
Again, this propagation correspondences exactly to the evolution of its corresponding classical density in phase space. Figure 4.3 shows a confidence inverval of this density drawn in red, also equivalent to the coherent state's Wigner representation. Since it is partly known in q-space, the coherent state is partly undetermined in p-space - again in agreement with the quantum uncertainty principle or Fourier relations. The first half of its orbit is depicted in the Figure.
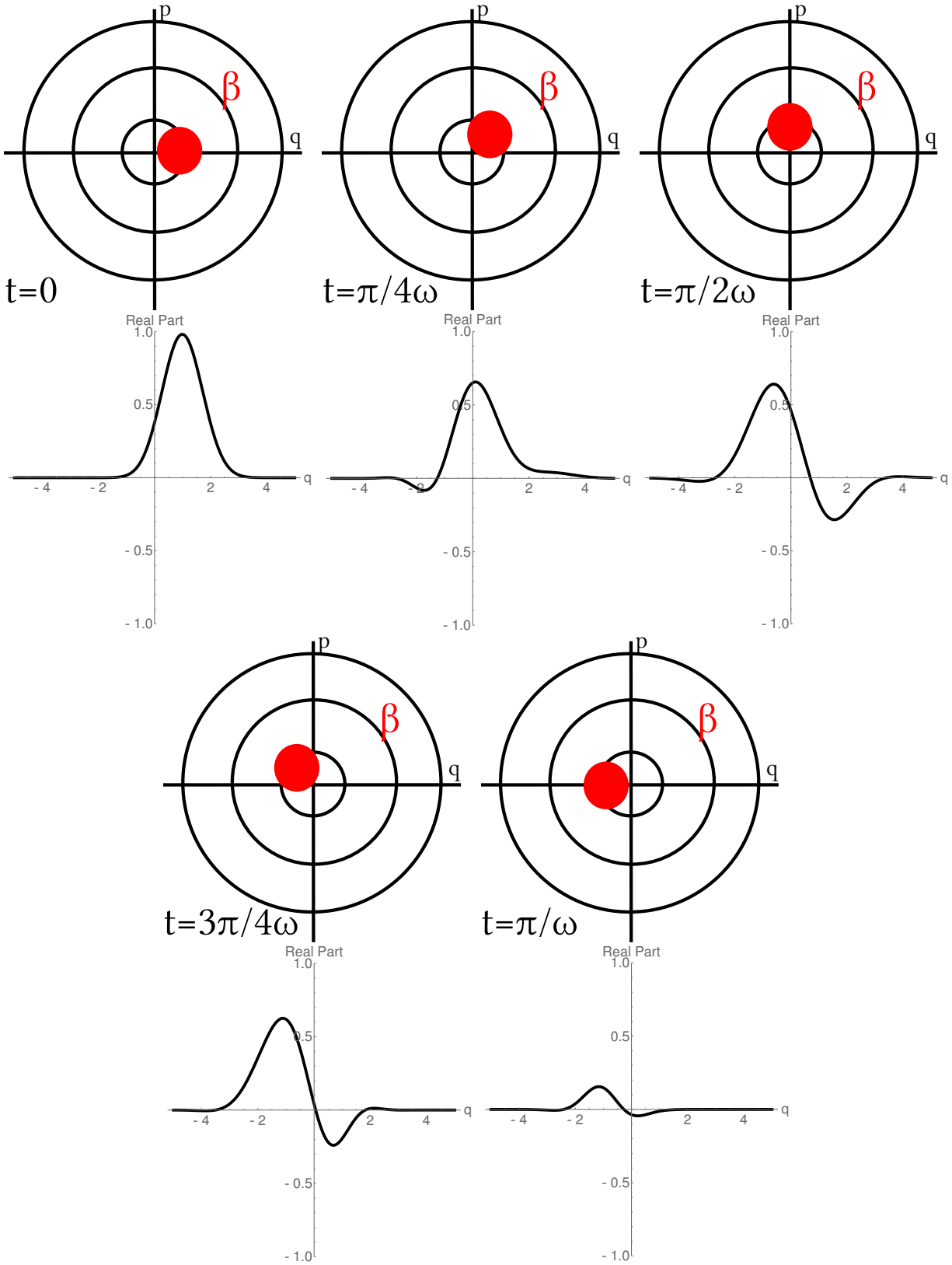
Figure 4.7: $t = 0, \frac{\pi}{4}, \frac{\pi}{2}, \frac{3\pi}{4}, \frac{8\pi}{4}$.

4.3.2 Van Vleck-Morette-Gutzwiller Propagator

Having thus motivated the classical correspondence of the Feynman path integral, we can summarize by writing that up to order $\hbar^2$

$$\text{semiclassical amplitude} \approx$$

$$\sum_{\text{intersections}} \sqrt{\text{classical probability density of intersection}}$$

$$\times \exp\left(i \times \text{classical action of intersecting trajectory}\right)$$

Formally, as can be proven rigorously, this is:

$$\implies \langle q' | e^{-i\frac{Ht}{\hbar}} | q \rangle = \sum_{\text{all classical paths}} \sqrt{-\frac{\frac{\partial^2 S}{\partial q' \partial q}}{2\pi i \hbar}} e^{i\frac{S}{\hbar}}. \tag{4.18}$$

This is the van Vleck-Morette-Gutzwiller (v.V.M.G.) propagator.

4.4 Stationary Phase

All semiclassics boils down to integration by stationary phase, or for complex arguments in exponentials, the method of steepest descents. We summarize it here and use the approach by Ursell '57[2].

$$\int \mathrm{d}z\, g(z) \exp\left[\frac{1}{\hbar} f(z, \alpha)\right] \tag{4.19}$$

$$-\frac{1}{2}u^2 = f(z) - f(z_0) = \frac{1}{2}(z - z_0)^2 f''(z_0) + \ldots, \tag{4.20}$$

where

$$f'(z)\frac{\mathrm{d}z}{\mathrm{d}u} = -u. \tag{4.21}$$

Since $f''(z_0) \neq 0$, this transformation is regular and one-to-one in a domain about $z = z_0$. Hence, there is an expansion of the form

$$g(z)\frac{\mathrm{d}z}{\mathrm{d}u} = -g(z)\frac{u(z)}{f'(z)} = \sum_m c_m u^m, \tag{4.22}$$

valid in small circles $|z - z_0| \leq R_z$ and $|u| \leq R_u$

Hence,

$$\exp\left[\frac{1}{\hbar}f(z_0)\right] \int_{C(U)} g(z) \exp\left[\frac{1}{\hbar}f(z)\right] \mathrm{d}z \tag{4.23}$$

$$= \int_{-U}^{U} g(z)\frac{\mathrm{d}z}{\mathrm{d}u} \exp\left(-\frac{1}{2\hbar}u^2\right) \mathrm{d}u \tag{4.24}$$

$$= \int_{-U}^{U} \left(\sum_m c_m u^m\right) \exp\left(-\frac{1}{2\hbar}u^2\right) \mathrm{d}u \tag{4.25}$$

$$= \sum_m \hbar^{\frac{1}{2}(m+1)} \int_{-\hbar^{-\frac{1}{2}}U}^{\hbar^{-\frac{1}{2}}U} v^m \exp\left(-\frac{1}{2}v^2\right) \mathrm{d}v. \tag{4.26}$$

The contour of integration in the u-plane is now chosen to be the real axis near $u = 0$. Letting $\hbar \to 0$ changes the limits of integration such that they range from $-\infty$ to ∞. This corresponds to the curve of steepest descent:

$$\int g(z) \exp\left[\frac{1}{\hbar}f(z)\right] \mathrm{d}z \approx \exp\left[\frac{1}{\hbar}f(z_0)\right] \sum_m c_m \hbar^{\frac{1}{2}(m+1)} \int_{-\infty}^{\infty} v^m \exp\left(-\frac{1}{2}v^2\right) \mathrm{d}v. \tag{4.27}$$

a convergent expansion in terms of incomplete factorial functions.

Summing over all saddle points, which contribute dominantly, evaluates this integral if they are well separated; the area that the integral encompasses between must be larger than $\hbar$.

4.5 Uniformization

Uniformization refers to extending the approach presented above such that it is "uniformly" convergent even when two (or more) saddle points are coalescing. Once again we use the approach by Ursell '57[2].

If there are two convergent saddle points as $\alpha \to 0$, the polynomial in $f(z)$ must be kept to one order higher. Let us try, then, to represent $f(z, \alpha)$ by the cubic

$$f(z, \alpha) = \frac{1}{3}u^3 - \zeta(\alpha)u + A(\alpha). \tag{4.28}$$

$$g(z)\frac{\mathrm{d}z}{\mathrm{d}u} = \sum_m p_m(\alpha)(u^2 - \zeta)^m + \sum_m q_m(\alpha)u(u^2 - \zeta)^m. \tag{4.29}$$

Then,

$$\exp\left[-\frac{1}{\hbar}A(\alpha)\right]\int g(z)\exp\left[\frac{1}{\hbar}f(z, \alpha)\right]\mathrm{d}z \tag{4.30}$$

$$\approx \sum_m p_m \int (u^2 - \zeta)^m \exp\left[\frac{1}{\hbar}\left(\frac{1}{3}u^3 - \zeta u\right)\right]\mathrm{d}u + \sum_m q_m \int u(u^2 - \zeta)^m \exp\left[\frac{1}{\hbar}\left(\frac{1}{3}u^3 - \zeta u\right)\right]\mathrm{d}u \tag{4.31}$$

It remains to evaluate the integrals

$$F_m(\zeta, \hbar, C_j) = \frac{1}{2\pi i}\int_{C_j}\mathrm{d}z\,(z^2 - \zeta)^m \exp\left(\frac{z^3}{3} - \zeta z\right), \tag{4.32}$$

$$G_m(\zeta, \hbar, C_j) = \frac{1}{2\pi i}\int_{C_j}\mathrm{d}z\,z(z^2 - \zeta)^m \exp\left(\frac{z^3}{3} - \zeta z\right), \tag{4.33}$$

where the contours of integration are C_1 from $\infty e^{-\frac{1}{3}\pi i}$ to $\infty e^{\frac{1}{3}\pi i}$, C_2 from $\infty e^{\frac{1}{3}\pi i}$ to $\infty e^{\pi i}$, and C_3 from $\infty e^{\pi i}$ to $\infty e^{-\frac{1}{3}\pi i}$.

The contours of integration ensure that each $F(C_j)$ and $G(C_j)$ is linearly dependent on the other two such that

$$F_m(\zeta, \hbar, C_1) + F_m(\zeta, \hbar, C_2) + F_m(\zeta, \hbar, C_3) = 0, \tag{4.34}$$

and the same with the G_ms.

Furthermore,

$$F_m(\zeta, \hbar, C_2) = \exp\left(\frac{4}{3}m\pi i + \frac{2}{3}\pi i\right) F_m(\zeta e^{\frac{2}{3}\pi i}, \hbar, C_1), \tag{4.35}$$

$$G_m(\zeta, \hbar, C_2) = \exp\left(\frac{4}{3}m\pi i + \frac{4}{3}\pi i\right) G_m(\zeta e^{\frac{2}{3}\pi i}, \hbar, C_1), \tag{4.36}$$

and

$$F_m(\zeta, \hbar, C_3) = \exp\left(\frac{4}{3}m\pi i + \frac{2}{3}\pi i\right) F_m(\zeta e^{\frac{2}{3}\pi i}, \hbar, C_2), \tag{4.37}$$

$$G_m(\zeta, \hbar, C_3) = \exp\left(\frac{4}{3}m\pi i + \frac{4}{3}\pi i\right) G_m(\zeta e^{\frac{2}{3}\pi i}, \hbar, C_2). \tag{4.38}$$

With these identities, the contour integrals in Eqs 6.21 and 6.22 can be evaluated, and their results are shown in Table 4.1 for the different contours C_j.

j	$F_0(\zeta, \hbar, C_j)$	$F_1(\zeta, \hbar, C_j)$	$G_0(\zeta, \hbar, C_j)$	$G_1(\zeta, \hbar, C_j)$
1	$\hbar^{\frac{1}{3}} \mathscr{A}\left(\frac{\zeta}{\hbar^{\frac{2}{3}}}\right)$	0	$-\hbar^{\frac{2}{3}} \mathscr{A}'\left(\frac{\zeta}{\hbar^{\frac{2}{3}}}\right)$	$-\hbar^{\frac{4}{3}} \mathscr{A}\left(\frac{\zeta}{\hbar^{\frac{2}{3}}}\right)$
2	$e^{\frac{4\pi i}{3}} \hbar^{\frac{1}{3}} \mathscr{B}\left(\frac{e^{\frac{2\pi i}{3}}\zeta}{\hbar^{\frac{2}{3}}}\right)$	0	$-e^{\frac{4\pi i}{3}} \hbar^{\frac{2}{3}} \mathscr{B}'\left(\frac{e^{\frac{2\pi i}{3}}\zeta}{\hbar^{\frac{2}{3}}}\right)$	$-e^{\frac{8\pi i}{3}} \hbar^{\frac{4}{3}} \mathscr{B}\left(\frac{e^{\frac{2\pi i}{3}}\zeta}{\hbar^{\frac{2}{3}}}\right)$
3	$-\hbar^{\frac{1}{3}} \left[\mathscr{A}\left(\frac{\zeta}{\hbar^{\frac{2}{3}}}\right) + e^{\frac{4\pi i}{3}} \mathscr{B}\left(\frac{e^{\frac{2\pi i}{3}}\zeta}{\hbar^{\frac{2}{3}}}\right)\right]$	0	$\hbar^{\frac{2}{3}} \left[\mathscr{A}'\left(\frac{\zeta}{\hbar^{\frac{2}{3}}}\right) + e^{\frac{4\pi i}{3}} \mathscr{B}'\left(\frac{e^{\frac{2\pi i}{3}}\zeta}{\hbar^{\frac{2}{3}}}\right)\right]$	$\hbar^{\frac{4}{3}} \left[\mathscr{A}\left(\frac{\zeta}{\hbar^{\frac{2}{3}}}\right) + e^{\frac{8\pi i}{3}} \mathscr{B}\left(\frac{e^{\frac{2\pi i}{3}}\zeta}{\hbar^{\frac{2}{3}}}\right)\right]$

Table 4.1:

4.6   Coherent States

Following Heller '91[3], we consider the operator

$$\hat{a} \equiv \frac{1}{\sqrt{2\hbar m\omega}}(m\omega\hat{x} + i\hat{p}). \tag{4.39}$$

A coherent state $|\alpha\rangle$ is defined as the eigenstate of this operator:

$$\hat{a}|\alpha\rangle = \alpha|\alpha\rangle, \tag{4.40}$$

where

$$\alpha = \frac{1}{\sqrt{2\hbar m\omega}}(m\omega q_\alpha + ip_\alpha). \tag{4.41}$$

In position space this becomes,

$$\langle q|\hat{a}|\alpha\rangle = \alpha\langle q|\alpha\rangle \tag{4.42}$$

$$= \frac{1}{\sqrt{2\hbar m\omega}}\left(m\omega q + \hbar\frac{\partial}{\partial q}\right)\langle q|\alpha\rangle. \tag{4.43}$$

The solution to this differential equation is:

$$\Psi_\alpha(q) \equiv \langle q|\alpha\rangle = \left(\frac{m\Re\omega}{\pi\hbar}\right)^{1/4}\exp\left[-\frac{m\omega}{2\hbar}(q-q_\alpha)^2 + \frac{i}{\hbar}p_\alpha(q-q_\alpha)\right]. \tag{4.44}$$

This is a Gaussian wavepacket with average position $\langle\alpha|\hat{q}|\alpha\rangle = q_\alpha$, average momentum $\langle\alpha|\hat{p}|\alpha\rangle = p_\alpha$.

The term "coherent state" is intimately tied to the underlying harmonic Hamiltonian for which it is the ground state. Namely, if we write $\frac{m\omega}{2\hbar} \equiv \frac{a+ib}{2\hbar}$, coherent states are only those for which $b = 0$. All others, for this combination of m and ω, are generally called squeezed states. However, in general, one deals with "coherent states" in anharmonic systems (without a necessarily clear harmonic analogue or m and ω) and the term is still used.

The term "squeezed state" is clear upon examining the uncertainties of the two conjugate degrees of freedom:

$$\Delta x^2 = \left\langle \alpha \left| (\hat{x} - x_\alpha)^2 \right| \alpha \right\rangle = \frac{\hbar}{2a}, \tag{4.45}$$

$$\Delta p^2 = \left\langle \alpha \left| (\hat{p} - p_\alpha)^2 \right| \alpha \right\rangle = \frac{a\hbar}{2} + \frac{b^2\hbar}{2a}, \tag{4.46}$$

$$\Delta x \Delta p = \frac{\hbar}{2}\sqrt{1 + \frac{b^2}{a^2}}. \tag{4.47}$$

With b finite, the uncertainty relation $\Delta x \Delta p$ is not at its lower bound. An equivalent definition of a coherent state is one for which its uncertainty relation is minimized. Clearly, in order to "minimize" something you need a parameter (in this case ω), and so a corresponding harmonic potential is again necessary for the term "coherent state" to have its traditional meaning. In this thesis, we will refer to anything that is a Gaussian in position space as a "coherent state", hedging on the fact that a corresponding harmonic oscillator can always be made to correspond to its "ω".

As a final point, coherent states are a fine basis set, just like q-states and p-states, except they are overcomplete and not orthogonal to each other:

$$\mathbb{I} = \frac{1}{2\pi\hbar} \int \int \mathrm{d}q_\alpha \mathrm{d}p_\alpha \left| \alpha \right\rangle \left\langle \alpha \right| \tag{4.48}$$

$$= \frac{1}{\pi} \int \int \mathrm{d}(\Re\alpha)\mathrm{d}(\Im\alpha) \left| \alpha \right\rangle \left\langle \alpha \right| \tag{4.49}$$

$$= \frac{1}{\pi} \int \mathrm{d}^2\alpha \left| \alpha \right\rangle \left\langle \alpha \right|. \tag{4.50}$$

5 The (Off-Center) Thawed Gaussian Approximation

5.1 Introduction

In this chapter we present the off-center thawed Gaussian approximation (OCTGA), a semiclassical wavepacket method, for multiple dimensions. Its accuracy and performance calculating Gaussian autocorrelations is examined and it is demonstrated that only a single trajectory is sufficient per overlap (in phase space) for every timestep regardless of the dimensionality of the model system, as long as the underlying saddle points are sufficiently separated. This stands in stark contrast to HK's exponential proliferation of trajectories (and associated stability matrices) with increasing degrees of freedom. Furthermore, the selection of the appropriate OCTGA trajectories is shown to be a "soft" root-finding problem that can be exploited to find a simpler one-dimensional manifold of trajectories which to follow. Thus, OCTGA can be a very useful semiclassical method in harmonic and excited anharmonic many-body systems.

Semiclassical quantum wave packet evolution[4, 5, 6] is a powerful method to evolve quantum states using classical trajectories. Many efficient methods exist but perhaps the most widely used is the Herman-Kluk (HK) propagator[7], based on frozen Gaussians[8]. In brief, the HK propagator is a stationary phase approximation of the quantum coherent state propagator evaluated in an uniformized initial value representation. Every time step requires the calculation of the overlap of a "swarm" of "frozen" Gaussians, often selected by Monte Carlo-based sampling dependent on the

Gaussian initial state. The propagation of every such Gaussian is governed by its central classical trajectory and each Gaussian's contribution to the propagator's value at a timestep is dependent on the classical action of its central trajectory as well as elements of its stability matrix. In practice, computation of these elements, first order differentials of final position and momenta with respect to initial position and momenta, is the most numerically intensive part of the procedure.

Unfortunately, HK suffers from an exponentially growing number of trajectories being necessary for convergence as the number of degrees of freedom increases. The calculation of every trajectory's associated stability matrix elements is thus doubly confounded: Not only do the number of matrix elements grow exponentially with degrees of freedom, the number of times these elements must be calculated also proliferates with the growing number of trajectories. Efforts have been made to address this issue, the most notable of which are cellular dynamics[9] and Filinov filtering[10]. However, these methods have proven ineffective in integrable systems and only reduce the growth of trajectories necessary to a point.

One way around this unfavorable scaling is to take a more targeted approach in selecting trajectories and allowing the coherent states to evolve internally under some potential instead of remaining "frozen". Such a method was described for the case of one particle in two dimensions, a chaotic system by this group in Ref. [11], and in integrable systems in Ref. [12], called the off-center thawed Gaussian approximation (OCTGA). A short review of the OCTGA can be found in Ref. [13]. By exploiting the fact that the classical and quantum distribution of Gaussians remains the same in phase space, the OCTGA is able to locally approximate a part of a larger quantum wave function by a Gaussian wave packet propagated under an appropriately chosen time-dependent potential.

For the case of auto and cross-correlation functions, essential to many measurables such as spectra[6], the wave function's overlap with its initial state at a range of times constitute the local regions of interest. At one end of the spectrum, this problem could be solved semiclassically through the use of the Van Vleck-Gutzwiller propagator, employed in a uniformizing way by integrating it (not by stationary phase) over initial and final wave functions[14]. At the other end

20

of the spectrum and far simpler to execute, this overlap could be captured by propagating a single Gaussian initial state via a classical trajectory defined by its expectation values of positions and momenta, and the environs of that trajectory. This is the "thawed Gaussan" wave packet method (TGA). Unfortunately, for anharmonic potentials, selecting such a classical trajectory centered in the middle of the Gaussian leads to results that are a poor approximation to the evolving wave function at even moderate times.

The OCTGA is an easy extension of the thawed Gaussian method where the Gaussian wavepacket is propagated under the potential expanded to second order around a guiding classical trajectory that is generally *not* at the center of the Gaussian. Several guiding trajectories, along with their corresponding guided wavepackets may be needed, one for each separate classical overlap contribution to the correlation function. There may be zero, one, or many of these zones at any one time. The guiding trajectory begins inside the phase space distribution of the initial state and travels to the center of the overlap in phase space at the time step of interest (see Figure 5.1 for a typical picture of overlaps in phase space).

The off-center guiding approach was initially applied for perhaps the worst imaginable case one would think: chaotic systems[11]. It has since been very successfully extended to an integrable two-dimensional system[12].

Given the large literature and growing activity in wavepacket based propagation schemes, it is very surprising that the OCTGA approach has not seen more development. The promise it holds of needing so few trajectories and wavepackets as opposed to typically hundreds of thousands or millions for HK, is alluring. Will it work in many dimensions, and does it have the promise of becoming a much faster (and more intuitive) semiclassical propagation scheme? Regarding many dimensions: off center guiding still requires only one trajectory per family of arriving trajectories in any number of dimensions, and no other trajectories at all for parts of the wave function that have not approached the target vicinity.

The purpose of this paper therefore is to extend the work of Ref [11, 12], the so called "off-center thawed Gaussian approximation", to many dimensions. In an effort to demonstrate

OCTGA's clear advantages in higher dimensions, we compare the two methods's performance with a model system containing many degrees of freedom and show that the OCTGA offers a strong semiclassical wavepacket alternative to HK.

5.2 Derivations

In this derivation vectors will be denoted by lowercase bold letters while matrices will be denoted by uppercase bold letters (ie. $\boldsymbol{a}$ and $\boldsymbol{A}$ respectively), be they greek or latin.

We present two equivalent derivations:

5.2.1 Derivation #1

$$G^{\mathrm{VVMG}}(\boldsymbol{q}, \boldsymbol{q}', t) = (2\pi i)^{-\frac{N}{2}} \sum_{\mathrm{paths}} \left(\det \frac{\partial^2 S(\boldsymbol{q}, \boldsymbol{q}')}{\partial \boldsymbol{q} \partial \boldsymbol{q}'} \right)^{1/2} \exp\left[iS(\boldsymbol{q}, \boldsymbol{q}', t) \right], \qquad (5.1)$$

where $\boldsymbol{q}'$ and $\boldsymbol{q}$ are the initial and final positions respectively for time t ($\hbar = 1$ throughout).

$$\Psi_\beta(\boldsymbol{q}, 0) = \left[\left(\frac{2}{\pi} \right)^N \det \boldsymbol{\Sigma} \right]^{1/4} \exp\left\{ \frac{i}{\hbar} \left[\boldsymbol{\xi} \cdot (\boldsymbol{q} - \boldsymbol{q}_\beta) + (\boldsymbol{q} - \boldsymbol{q}_\beta) \cdot \boldsymbol{\Sigma} \cdot (\boldsymbol{q} - \boldsymbol{q}_\beta) + \gamma \right] \right\}. \qquad (5.2)$$

$\boldsymbol{\Sigma}_{ii}^{-\frac{1}{2}} = \left(\boldsymbol{\Sigma}_{ii}^{-\frac{1}{2}} \right)^T$ and is proportional to the spread of the Gaussian along q_i, $\boldsymbol{\Sigma}_{ij}$ for $i \neq j$ describes q_i-q_j correlation, $\Re \boldsymbol{\xi}$ is equal to the central momentum while $\Im \boldsymbol{\xi}$ describes $\boldsymbol{p}$-$\boldsymbol{q}$ correlation.

Instead of the full semiclassical propagator, let us apply the harmonically approximated semiclassical (h.s.c.) propagator,

$$G^{\mathrm{hsc}}(\boldsymbol{q}, \boldsymbol{q}', t) = \sum_{\mathrm{paths}} \left[\left(\frac{\partial^2 S(\boldsymbol{q}, \boldsymbol{q}')}{\partial \boldsymbol{q} \partial \boldsymbol{q}'} \right)^{1/2} \right]^{\mathrm{har}} \exp\left[iS^{\mathrm{har}}(\boldsymbol{q}, \boldsymbol{q}', t) \right], \qquad (5.3)$$

to this initial state,

$$\Psi_\beta^{\mathrm{hsc}}(\boldsymbol{q}, t) = \int_{-\infty}^{\infty} \mathrm{d}\boldsymbol{q}' \, G^{\mathrm{hsc}}(\boldsymbol{q}, \boldsymbol{q}', t) \Psi_\beta(\boldsymbol{q}', 0), \qquad (5.4)$$

where we have expanded the action $S(\boldsymbol{q}, \boldsymbol{q}')$ up to second order around an initial $\boldsymbol{q}_0$ and its time evolute $\boldsymbol{q}_t$:

$$
\begin{aligned}
S^{\text{har}}(\boldsymbol{q}, \boldsymbol{q}', t) \;=\; & S(\boldsymbol{q} = \boldsymbol{q}_t, \boldsymbol{q}' = \boldsymbol{q}_0) + \left(\frac{\partial S}{\partial \boldsymbol{q}_t}\right)_{\boldsymbol{q}=\boldsymbol{q}_t, \boldsymbol{q}'=\boldsymbol{q}_0} \cdot (\boldsymbol{q} - \boldsymbol{q}_t) + \left(\frac{\partial S}{\partial \boldsymbol{q}_0}\right)_{\boldsymbol{q}=\boldsymbol{q}_t, \boldsymbol{q}'=\boldsymbol{q}_0} \cdot (\boldsymbol{q}' - \boldsymbol{q}_0) \\
& + \frac{1}{2}(\boldsymbol{q} - \boldsymbol{q}_t) \cdot \left(\frac{\partial^2 S}{\partial \boldsymbol{q}_t^2}\right)_{\boldsymbol{q}=\boldsymbol{q}_t, \boldsymbol{q}'=\boldsymbol{q}_0} \cdot (\boldsymbol{q} - \boldsymbol{q}_t) + \frac{1}{2}(\boldsymbol{q}' - \boldsymbol{q}_0) \cdot \left(\frac{\partial^2 S}{\partial \boldsymbol{q}_0^2}\right)_{\boldsymbol{q}=\boldsymbol{q}_t, \boldsymbol{q}'=\boldsymbol{q}_0} \cdot (\boldsymbol{q}' - \boldsymbol{q}_0) \\
& + (\boldsymbol{q}' - \boldsymbol{q}_0) \cdot \left(\frac{\partial^2 S}{\partial \boldsymbol{q}_0 \partial \boldsymbol{q}_t}\right)_{\boldsymbol{q}=\boldsymbol{q}_t, \boldsymbol{q}'=\boldsymbol{q}_0} \cdot (\boldsymbol{q} - \boldsymbol{q}_t).
\end{aligned}
$$

Substituting in the expanded action in Eq. 5.4 yields,

$$\Psi_\beta^{\text{hsc}}(\boldsymbol{q}, t) \tag{5.5}$$

$$= (2\pi i)^{-\frac{N}{2}} \left[\left(\frac{2}{\pi} \right)^N \det \boldsymbol{\Sigma} \right]^{1/4} \sum_{\text{paths}} \left(\det \frac{\partial^2 S}{\partial \boldsymbol{q}_t \partial \boldsymbol{q}_0} \right)^{1/2} \int_{-\infty}^{\infty} \mathrm{d}\boldsymbol{q}' \tag{5.6}$$

$$\times \exp \left\{ i \left[S(\boldsymbol{q}_t, \boldsymbol{q}_0) + \left(\frac{\partial S}{\partial \boldsymbol{q}_t} \right)_{\boldsymbol{q}_0} \cdot (\boldsymbol{q} - \boldsymbol{q}_t) + \left(\frac{\partial S}{\partial \boldsymbol{q}_0} \right)_{\boldsymbol{q}_t} \cdot (\boldsymbol{q}' - \boldsymbol{q}_0) \right. \right.$$

$$+ \frac{1}{2} (\boldsymbol{q} - \boldsymbol{q}_t) \cdot \left(\frac{\partial^2 S}{\partial \boldsymbol{q}_t^2} \right)_{\boldsymbol{q}_0} \cdot (\boldsymbol{q} - \boldsymbol{q}_t) + \frac{1}{2} (\boldsymbol{q}' - \boldsymbol{q}_0) \cdot \left(\frac{\partial^2 S}{\partial \boldsymbol{q}_0^2} \right)_{\boldsymbol{q}_t} \cdot (\boldsymbol{q}' - \boldsymbol{q}_0)$$

$$\left. \left. + (\boldsymbol{q}' - \boldsymbol{q}_0) \cdot \left(\frac{\partial^2 S}{\partial \boldsymbol{q}_0 \partial \boldsymbol{q}_t} \right) \cdot (\boldsymbol{q} - \boldsymbol{q}_t) + \boldsymbol{\xi} \cdot (\boldsymbol{q}' - \boldsymbol{q}_\beta) + (\boldsymbol{q}' - \boldsymbol{q}_\beta) \cdot \boldsymbol{\Sigma} \cdot (\boldsymbol{q}' - \boldsymbol{q}_\beta) + \gamma \right] \right\}$$

$$= (2\pi i)^{-\frac{N}{2}} \left[\left(\frac{2}{\pi} \right)^N \det \boldsymbol{\Sigma} \right]^{1/4} \sum_{\text{paths}} \left(\det \frac{\partial^2 S}{\partial \boldsymbol{q}_t \partial \boldsymbol{q}_0} \right)^{1/2} \int_{-\infty}^{\infty} \mathrm{d}\boldsymbol{q}' \tag{5.7}$$

$$\times \exp \left\{ i \left[S(\boldsymbol{q}_t, \boldsymbol{q}_0) + \left(\frac{\partial S}{\partial \boldsymbol{q}_t} \right)_{\boldsymbol{q}_0} \cdot (\boldsymbol{q} - \boldsymbol{q}_t) - \left(\frac{\partial S}{\partial \boldsymbol{q}_0} \right)_{\boldsymbol{q}_t} \cdot \boldsymbol{q}_0 \right. \right.$$

$$+ \frac{1}{2} (\boldsymbol{q} - \boldsymbol{q}_t) \cdot \left(\frac{\partial^2 S}{\partial \boldsymbol{q}_t^2} \right)_{\boldsymbol{q}_0} \cdot (\boldsymbol{q} - \boldsymbol{q}_t) + \frac{1}{2} \boldsymbol{q}_0 \cdot \left(\frac{\partial^2 S}{\partial \boldsymbol{q}_0^2} \right)_{\boldsymbol{q}_t} \cdot \boldsymbol{q}_0$$

$$\left. \left. - \boldsymbol{q}_0 \cdot \left(\frac{\partial^2 S}{\partial \boldsymbol{q}_0 \partial \boldsymbol{q}_t} \right) \cdot (\boldsymbol{q} - \boldsymbol{q}_t) - \boldsymbol{\xi} \cdot \boldsymbol{q}_\beta + \boldsymbol{q}_\beta \cdot \boldsymbol{\Sigma} \cdot \boldsymbol{q}_\beta + \gamma \right] \right\}$$

$$\times \exp \left\{ i \left[\left(\frac{\partial S}{\partial \boldsymbol{q}_0} \right)_{\boldsymbol{q}_t} + (\boldsymbol{q} - \boldsymbol{q}_t) \cdot \left(\frac{\partial^2 S}{\partial \boldsymbol{q}_0 \partial \boldsymbol{q}_t} \right) - \boldsymbol{q}_0 \cdot \left(\frac{\partial^2 S}{\partial \boldsymbol{q}_0^2} \right)_{\boldsymbol{q}_t} + \boldsymbol{\xi} - 2\boldsymbol{q}_\beta \cdot \boldsymbol{\Sigma} \right] \cdot \boldsymbol{q}' \right.$$

$$\left. + i\boldsymbol{q}' \cdot \left[\boldsymbol{\Sigma} + \frac{1}{2} \left(\frac{\partial^2 S}{\partial \boldsymbol{q}_0^2} \right)_{\boldsymbol{q}_t} \right] \cdot \boldsymbol{q}' \right\}$$

$$= (2\pi i)^{-\frac{N}{2}} \left[\left(\frac{2}{\pi} \right)^N \det \boldsymbol{\Sigma} \right]^{1/4} \sum_{\text{paths}} \left(\det \frac{\partial^2 S}{\partial \boldsymbol{q}_t \partial \boldsymbol{q}_0} \right)^{1/2} \tag{5.8}$$

$$\times \exp \left\{ i \left[S(\boldsymbol{q}_t, \boldsymbol{q}_0) + \left(\frac{\partial S}{\partial \boldsymbol{q}_t} \right)_{\boldsymbol{q}_0} \cdot (\boldsymbol{q} - \boldsymbol{q}_t) - \left(\frac{\partial S}{\partial \boldsymbol{q}_0} \right)_{\boldsymbol{q}_t} \cdot \boldsymbol{q}_0 \right. \right.$$

$$+ \frac{1}{2} (\boldsymbol{q} - \boldsymbol{q}_t) \cdot \left(\frac{\partial^2 S}{\partial \boldsymbol{q}_t^2} \right)_{\boldsymbol{q}_0} \cdot (\boldsymbol{q} - \boldsymbol{q}_t) + \frac{1}{2} \boldsymbol{q}_0 \cdot \left(\frac{\partial^2 S}{\partial \boldsymbol{q}_0^2} \right)_{\boldsymbol{q}_t} \cdot \boldsymbol{q}_0$$

$$\left. \left. - \boldsymbol{q}_0 \cdot \left(\frac{\partial^2 S}{\partial \boldsymbol{q}_0 \partial \boldsymbol{q}_t} \right) \cdot (\boldsymbol{q} - \boldsymbol{q}_t) - \boldsymbol{\xi} \cdot \boldsymbol{q}_\beta + \boldsymbol{q}_\beta \cdot \boldsymbol{\Sigma} \cdot \boldsymbol{q}_\beta + \gamma \right] \right\}$$

$$\times \left(\frac{\pi^N}{\det \boldsymbol{A}} \right)^{\frac{1}{2}} \exp \left(-\frac{1}{4} \boldsymbol{b} \cdot \boldsymbol{A}^{-1} \cdot \boldsymbol{b} \right),$$

where

$$\boldsymbol{A} = i\left[\boldsymbol{\Sigma} + \frac{1}{2}\left(\frac{\partial^2 S}{\partial \boldsymbol{q}_0^2}\right)_{\boldsymbol{q}_t}\right], \tag{5.9}$$

and

$$\boldsymbol{b} = i\left[\left(\frac{\partial S}{\partial \boldsymbol{q}_0}\right)_{\boldsymbol{q}_t} + (\boldsymbol{q} - \boldsymbol{q}_t)\cdot\left(\frac{\partial^2 S}{\partial \boldsymbol{q}_0 \partial \boldsymbol{q}_t}\right) - \boldsymbol{q}_0\cdot\left(\frac{\partial^2 S}{\partial \boldsymbol{q}_0^2}\right)_{\boldsymbol{q}_t} + \boldsymbol{\xi} - 2\boldsymbol{q}_\beta\cdot\boldsymbol{\Sigma}\right]. \tag{5.10}$$

This can be reexpressed as a Gaussian in terms of $(\boldsymbol{q} - \boldsymbol{q}_t)$:

$$\Psi_\beta(\boldsymbol{q}, t)$$

$$= (2\pi i)^{-\frac{N}{2}}\left[\left(\frac{2}{\pi}\right)^N \det\boldsymbol{\Sigma}\right]^{1/4}\sum_{\text{paths}}\left(\det\frac{\partial^2 S}{\partial \boldsymbol{q}_t \partial \boldsymbol{q}_0}\right)^{1/2}\left(\frac{\pi^N}{i^N \det\left[\boldsymbol{\Sigma} + \frac{1}{2}\left(\frac{\partial^2 S}{\partial \boldsymbol{q}_0^2}\right)_{\boldsymbol{q}_t}\right]}\right)^{\frac{1}{2}} \tag{5.11}$$

$$\times \exp\left\{(\boldsymbol{q} - \boldsymbol{q}_t)\cdot\left[-\frac{i}{4}\left(\frac{\partial^2 S}{\partial \boldsymbol{q}_0 \partial \boldsymbol{q}_t}\right)\cdot\left(\boldsymbol{\Sigma} + \frac{1}{2}\left(\frac{\partial^2 S}{\partial \boldsymbol{q}_0^2}\right)_{\boldsymbol{q}_t}\right)^{-1}\cdot\left(\frac{\partial^2 S}{\partial \boldsymbol{q}_0 \partial \boldsymbol{q}_t}\right)\right]\cdot(\boldsymbol{q} - \boldsymbol{q}_t)\right.$$

$$+ i\left[\boldsymbol{p}_t - \boldsymbol{q}_0\cdot\left(\frac{\partial^2 S}{\partial \boldsymbol{q}_0 \partial \boldsymbol{q}_t}\right) - \frac{1}{2}\left(-\boldsymbol{p}_0 - \boldsymbol{q}_0\cdot\left(\frac{\partial^2 S}{\partial \boldsymbol{q}_0^2}\right)_{\boldsymbol{q}_t} + \boldsymbol{\xi} - 2\boldsymbol{q}_\beta\cdot\boldsymbol{\Sigma}\right)\cdot\left(\boldsymbol{\Sigma} + \frac{1}{2}\left(\frac{\partial^2 S}{\partial \boldsymbol{q}_0^2}\right)_{\boldsymbol{q}_t}\right)^{-1}\cdot\left(\frac{\partial^2 S}{\partial \boldsymbol{q}_0 \partial \boldsymbol{q}_t}\right)\right]\cdot(\boldsymbol{q} - \boldsymbol{q}_t)$$

$$+ i\left(S(\boldsymbol{q}_t, \boldsymbol{q}_0) + \boldsymbol{p}_0\cdot\boldsymbol{q}_0 + \frac{1}{2}\boldsymbol{q}_0\cdot\left(\frac{\partial^2 S}{\partial \boldsymbol{q}_0^2}\right)_{\boldsymbol{q}_t}\cdot\boldsymbol{q}_0 - \boldsymbol{\xi}\cdot\boldsymbol{q}_\beta + \boldsymbol{q}_\beta\cdot\boldsymbol{\Sigma}\cdot\boldsymbol{q}_\beta + \gamma\right)$$

$$\left. -\frac{i}{4}\left[-\boldsymbol{p}_0 - \boldsymbol{q}_0\cdot\left(\frac{\partial^2 S}{\partial \boldsymbol{q}_0^2}\right)_{\boldsymbol{q}_t} + \boldsymbol{\xi} - 2\boldsymbol{q}_\beta\cdot\boldsymbol{\Sigma}\right]\left[\boldsymbol{\Sigma} + \frac{1}{2}\left(\frac{\partial^2 S}{\partial \boldsymbol{q}_0^2}\right)_{\boldsymbol{q}_t}\right]^{-1}\left[-\boldsymbol{p}_0 - \boldsymbol{q}_0\cdot\left(\frac{\partial^2 S}{\partial \boldsymbol{q}_0^2}\right)_{\boldsymbol{q}_t} + \boldsymbol{\xi} - 2\boldsymbol{q}_\beta\cdot\boldsymbol{\Sigma}\right]\right\}.$$

$$\boldsymbol{M}(t) = \begin{pmatrix} \boldsymbol{M}(t)_{11} & \boldsymbol{M}(t)_{12} \\ \boldsymbol{M}(t)_{21} & \boldsymbol{M}(t)_{22} \end{pmatrix} = \begin{pmatrix} \left(\frac{\partial \boldsymbol{p}_t}{\partial \boldsymbol{p}_0}\right)_{\boldsymbol{q}_0} & \left(\frac{\partial \boldsymbol{p}_t}{\partial \boldsymbol{q}_0}\right)_{\boldsymbol{p}_0} \\ \left(\frac{\partial \boldsymbol{q}_t}{\partial \boldsymbol{p}_0}\right)_{\boldsymbol{q}_0} & \left(\frac{\partial \boldsymbol{q}_t}{\partial \boldsymbol{q}_0}\right)_{\boldsymbol{p}_0} \end{pmatrix}. \tag{5.12}$$

In terms of $\boldsymbol{M}$,

$$\left(\frac{\partial^2 S}{\partial \boldsymbol{q}_0^2}\right)_{\boldsymbol{q}_t} = \boldsymbol{M}_{22}\cdot\boldsymbol{M}_{21}^{-1}, \quad \frac{\partial^2 S}{\partial \boldsymbol{q}_0 \partial \boldsymbol{q}_t} = -\boldsymbol{M}_{21}^{-1}, \quad \left(\frac{\partial^2 S}{\partial \boldsymbol{q}_t^2}\right)_{\boldsymbol{q}_0} = \boldsymbol{M}_{11}\cdot\boldsymbol{M}_{21}^{-1}, \tag{5.13}$$

where we dropped the t argument for brevity's sake and $\boldsymbol{M}(0) = \mathbb{I}_{2N \times 2N}$.

Determining the second order derivatives of the action can be accomplished symplectically by solving for the stability matrix $\boldsymbol{M}(t)$ of the guiding trajectory $(\boldsymbol{q}_0, \boldsymbol{q}_t)$ with the equation of motion

$$\dot{\boldsymbol{M}}(t) = \boldsymbol{K}(t) \cdot \boldsymbol{M}(t), \tag{5.14}$$

where

$$\boldsymbol{K}(t) = \begin{pmatrix} -\frac{\partial^2 H}{\partial \boldsymbol{q} \partial \boldsymbol{p}} & -\frac{\partial^2 H}{\partial \boldsymbol{q}^2} \\ \frac{\partial^2 H}{\partial \boldsymbol{p}^2} & \frac{\partial^2 H}{\partial \boldsymbol{p} \partial \boldsymbol{q}} \end{pmatrix}. \tag{5.15}$$

5.2.2 Derivation #2

Since the semiclassical propagator is exact for harmonic potentials, the off-centered thawed Gaussian approximation can be equivalently derived straight from the full Schrödinger equation wit its potential quadratically expanded around a guiding trajectory. This is how the formalism was actually first derived in the 70s.

Recalling the time-dependent Schrödinger equation:

$$i\frac{\partial \Psi_\beta(\boldsymbol{q}, t)}{\partial t} = -\frac{1}{2}\frac{\partial^2 \Psi_\beta(\boldsymbol{q}, t)}{\partial \boldsymbol{q}^2} + V(\boldsymbol{q})\Psi_\beta(\boldsymbol{q}, t). \tag{5.16}$$

Let us consider the potential only up to second order, such that,

$$V(\boldsymbol{q}) = V(\boldsymbol{q}_t) + \left.\frac{\partial V(\boldsymbol{q})}{\partial \boldsymbol{q}}\right|_{\boldsymbol{q}=\boldsymbol{q}_t} \cdot (\boldsymbol{q} - \boldsymbol{q}_t) + \frac{1}{2}(\boldsymbol{q} - \boldsymbol{q}_t) \cdot \left.\frac{\partial^2 V(\boldsymbol{q})}{\partial \boldsymbol{q}^2}\right|_{\boldsymbol{q}=\boldsymbol{q}_t} \cdot (\boldsymbol{q} - \boldsymbol{q}_t) \tag{5.17}$$

and let

$$\Psi_\beta(\boldsymbol{q}, t) = A \exp\left\{i\left[\boldsymbol{\xi}_t \cdot (\boldsymbol{q} - \boldsymbol{q}_t) + (\boldsymbol{q} - \boldsymbol{q}_t) \cdot \boldsymbol{A}_t \cdot (\boldsymbol{q} - \boldsymbol{q}_t) + \gamma_t\right]\right\}. \tag{5.18}$$

Substituting Eqs. 5.17 and 6.2 into Eq. 5.16 and equating like powers of $(\boldsymbol{q} - \boldsymbol{q}_t)$ yields the ordinary differential equations

$$\dot{\boldsymbol{A}}_t \;=\; -2\boldsymbol{A}_t \cdot \boldsymbol{A}_t - \frac{1}{2}\frac{\partial^2 V(\boldsymbol{q})}{\partial \boldsymbol{q}^2}\bigg|_{\boldsymbol{q}=\boldsymbol{q}_t} \tag{5.19}$$

$$\dot{\boldsymbol{\xi}}_t \;=\; 2\dot{\boldsymbol{q}}_t \cdot \boldsymbol{A}_t - 2\boldsymbol{\xi}_t \cdot \boldsymbol{A}_t - \frac{\partial V(\boldsymbol{q})}{\partial \boldsymbol{q}}\bigg|_{\boldsymbol{q}=\boldsymbol{q}_t} \tag{5.20}$$

$$\dot{\gamma}_t \;=\; i\,\mathrm{Tr}\,\boldsymbol{A}_t - \frac{1}{2}\boldsymbol{\xi}\cdot\boldsymbol{\xi} - V(\boldsymbol{q}_t) + \boldsymbol{\xi}_t\cdot\dot{\boldsymbol{q}}_t \tag{5.21}$$

In this derivation, for the sake of diversity, we will solve these equations of motion without direct appeal to stability matrices, though all the expressions we find can be reexpressed in terms of them.

Let $\boldsymbol{A}_t = \frac{1}{2}\boldsymbol{P}_{\boldsymbol{Z}t}\cdot\boldsymbol{Z}_t^{-1}$.

Substituting this into Eq. 5.19

$$\implies \dot{\boldsymbol{P}}_{\boldsymbol{Z}t} \;=\; -\frac{\partial^2 V(\boldsymbol{q})}{\partial \boldsymbol{q}^2}\bigg|_{\boldsymbol{q}=\boldsymbol{q}_t}\cdot\boldsymbol{Z}_t \tag{5.22}$$

$$\implies \dot{\boldsymbol{Z}}_t \;=\; \boldsymbol{P}_{\boldsymbol{Z}t}. \tag{5.23}$$

Let $\boldsymbol{\xi}_t = \boldsymbol{p}_t + \boldsymbol{\zeta}_t$.

Substituting this into Eq. 5.20 produces

$$\dot{\boldsymbol{\zeta}}_t = -2\boldsymbol{A}_t\cdot\boldsymbol{\zeta}_t \tag{5.24}$$

and it also simplifies Eq. 5.21,

$$\dot{\gamma}_t = L + i\,\mathrm{Tr}\,\boldsymbol{A}_t - \frac{1}{2}\boldsymbol{\zeta}_t\cdot\boldsymbol{\zeta}_t. \tag{5.25}$$

To find the solution γ_t from Eq. 5.25, the integral with time of the last two terms must be found.

The integral of $\mathrm{Tr}\, \boldsymbol{A}_t$ is fairly easy to do:

$$
\begin{aligned}
\int_0^t \mathrm{Tr}\, \boldsymbol{A}_{t'}\, dt' &= \frac{1}{2} \int_0^t dt'\, \mathrm{Tr}\left(\dot{\boldsymbol{Z}}_{t'} \cdot \boldsymbol{Z}_{t'}^{-1} \right) \\
&= \frac{1}{2} \log\left(\det \boldsymbol{Z}_t \right) \tag{5.26}
\end{aligned}
$$

It is dealing with the next term where things get a little hairy. Before we integrate $\boldsymbol{\zeta}_t \cdot \boldsymbol{\zeta}_t$, we must figure out what $\boldsymbol{\zeta}_t$ is. Diagonalizing $\boldsymbol{A}_t$ in Eq. 5.24 simplifies the process:

$$
\begin{aligned}
\boldsymbol{U}_t^{-1} \cdot \dot{\boldsymbol{\zeta}}_t &= -2\boldsymbol{U}_t^{-1} \cdot \boldsymbol{A}_t \cdot \boldsymbol{U}_t \cdot \boldsymbol{U}_t^{-1} \cdot \boldsymbol{\zeta}_t \tag{5.27} \\
\boldsymbol{U}_t^{-1} \cdot \dot{\boldsymbol{\zeta}}_t &= -2\left(\boldsymbol{U}_t^{-1} \cdot \boldsymbol{A}_t \cdot \boldsymbol{U}_t \right) \cdot \left(\boldsymbol{U}_t^{-1} \cdot \boldsymbol{\zeta}_t \right) \tag{5.28} \\
\dot{\boldsymbol{\zeta}}_t^* &= -2\boldsymbol{A}_t^* \cdot \boldsymbol{\zeta}_t^* \tag{5.29}
\end{aligned}
$$

where $\boldsymbol{A}_t^*$ is the diagonal matrix $\boldsymbol{U}_t^{-1} \cdot \boldsymbol{A}_t \cdot \boldsymbol{U}_t$ and ζ_t^* is $\boldsymbol{U}_t^{-1} \cdot \boldsymbol{\zeta}_t$.

Solving Eq. 5.29 leads to the solution of Eq. 5.24:

$$
\boldsymbol{\zeta}_t = c_1 \exp\left[\int_0^t \lambda_1(t')dt' \right] \boldsymbol{u}_1 + c_2 \exp\left[\int_0^t \lambda_2(t')dt' \right] \boldsymbol{u}_2 + \ldots + c_N \exp\left[\int_0^t \lambda_N(t')dt' \right] \boldsymbol{u}_N \tag{5.30}
$$

where $\{\lambda_i(t)\}_{i=1..N}$ are the (time-dependent) eigenvalues of $\boldsymbol{A}_t$ with eigenvectors $\{\boldsymbol{u}_i\}_{i=1..N}$ at $t = 0$, and $\{c_i\}_{i=1..N}$ are coefficients such that

$$
\boldsymbol{\zeta}_0 = c_1 \boldsymbol{u}_1 + c_2 \boldsymbol{u}_2 + \ldots + c_N \boldsymbol{u}_N. \tag{5.31}
$$

What we've really done here is rederive matrix exponentiation. The solution can be more concisely written as:

$$
\boldsymbol{\zeta}_t = \exp\left(-2 \int_0^t dt' \boldsymbol{A}_{t'} \right) \boldsymbol{\zeta}_0. \tag{5.32}
$$

We are now in a position to write the solution of Eq. 5.25:

$$\gamma_t = S + \frac{i}{2} \log\left(\det \boldsymbol{Z}_t\right) - \frac{1}{2} \int_0^t dt' \boldsymbol{\zeta}_{t'} \cdot \boldsymbol{\zeta}_{t'} \tag{5.33}$$

where $\boldsymbol{\zeta}_t$ is given in Eq. 5.32.

In the original center-led thawed Gaussian approximation (TGA), $\boldsymbol{\xi}_t = \boldsymbol{p}_t \implies \boldsymbol{\zeta}_t = \boldsymbol{\zeta}_0 = 0$ and so this last term is not present.

Note that $\boldsymbol{\xi}_t$ is also dependent on Eq. 5.32 since $\boldsymbol{\xi}_t = \boldsymbol{p}_t + \boldsymbol{\zeta}_t$.

At $t = 0$, let's set our initial Gaussian to be centred at $(\boldsymbol{p}_\beta, \boldsymbol{q}_\beta)$ with a dispersion of $\boldsymbol{\sigma}_\beta$:

$$\Psi_\beta(q,0) = \left(\pi^N \det \boldsymbol{\sigma}_\beta^2\right)^{-1/4} \exp\left[i\boldsymbol{p}_\beta \cdot (\boldsymbol{q} - \boldsymbol{q}_\beta) - \frac{1}{2}(\boldsymbol{q} - \boldsymbol{q}_\beta) \cdot \boldsymbol{\sigma}_\beta^{-2} \cdot (\boldsymbol{q} - \boldsymbol{q}_\beta) \right]. \tag{5.34}$$

Equating this to the initial state written in terms of the $\boldsymbol{\xi}_0$, $\boldsymbol{A}_0$, and γ_0 variables in Eq. 6.2 sets

$$\boldsymbol{A}_0 = \frac{i}{2}\boldsymbol{\sigma}_\beta^{-2} \tag{5.35}$$

$$\boldsymbol{\xi}_0 = \boldsymbol{p}_\beta + 2\boldsymbol{A}_0 \cdot (\boldsymbol{q}_0 - \boldsymbol{q}_\beta) \tag{5.36}$$

$$\boldsymbol{\gamma}_0 = (\boldsymbol{q}_0 - \boldsymbol{q}_\beta) \cdot \left[\boldsymbol{A}_0 \cdot (\boldsymbol{q}_0 - \boldsymbol{q}_\beta) + \boldsymbol{p}_\beta\right] \tag{5.37}$$

$$A = \left(\pi^N \det \boldsymbol{\sigma}_\beta^2\right)^{-1/4} \tag{5.38}$$

where $\boldsymbol{I}$ is an $N \times N$ identity matrix.

This means that

$$\boldsymbol{\zeta}_0 = \boldsymbol{\xi}_0 - \boldsymbol{p}_0 = \boldsymbol{p}_\beta + 2\boldsymbol{A}_0 \cdot (\boldsymbol{q}_0 - \boldsymbol{q}_\beta) - \boldsymbol{p}_0. \tag{5.39}$$

Taking the inner product of the initial Gaussian wavepacket $\Psi_\beta(\boldsymbol{q}, 0)$ and the propagated wavepacket $\Psi_\beta(\boldsymbol{q}, t)$, both given by Eq. 6.2, we find that an individual term of the autocorrelation is

$$\langle \boldsymbol{\beta} | \boldsymbol{\beta}(t) \rangle_j = 2^{n/2} \sqrt{\frac{\det \boldsymbol{A}_0}{\det(\boldsymbol{A}_0 + \boldsymbol{A}_t)}} \exp\left[i(\gamma_t - \gamma_0^*) + i(\boldsymbol{\xi}_0^* \cdot \boldsymbol{q}_0 - \boldsymbol{\xi}_t \cdot \boldsymbol{q}_t) + i(\boldsymbol{q}_0 \cdot \boldsymbol{A}_0 \cdot \boldsymbol{q}_0 + \boldsymbol{q}_t \cdot \boldsymbol{A}_t \cdot \boldsymbol{q}_t)\right] \tag{5.40}$$

$$\times \exp\left[-\frac{i}{4}(\boldsymbol{\xi}_0^* - \boldsymbol{\xi}_t + 2\boldsymbol{A}_0 \cdot \boldsymbol{q}_0 + 2\boldsymbol{A}_t \cdot \boldsymbol{q}_t) \cdot (\boldsymbol{A}_0 + \boldsymbol{A}_t)^{-1} \cdot (\boldsymbol{\xi}_0^* - \boldsymbol{\xi}_t + 2\boldsymbol{A}_0 \cdot \boldsymbol{q}_0 + 2\boldsymbol{A}_t \cdot \boldsymbol{q}_t)\right].$$

29

In one dimension, Eq. 5.41 reduces to

$$\langle \boldsymbol{\beta} | \boldsymbol{\beta}(t) \rangle_j = \left\{ \sqrt{\frac{2A_0}{A_t + A_0}} \exp\left[i(\gamma_t - \gamma_0^*) - \frac{i}{4} \frac{(\xi_0 - \xi_t)^2}{A_t + A_0} + i \frac{(A_t \xi_0^* + A_0 \xi_t)(q_0 - q_t) + i A_t A_0 (q_0 - q_t)^2}{A_t + A_0} \right] \right\}_j$$

(5.41)

The subscript j denotes a contribution from a particular trajectory. In one dimension, Eq. 5.41 reduces to Eq. 20 in Ref. [15].
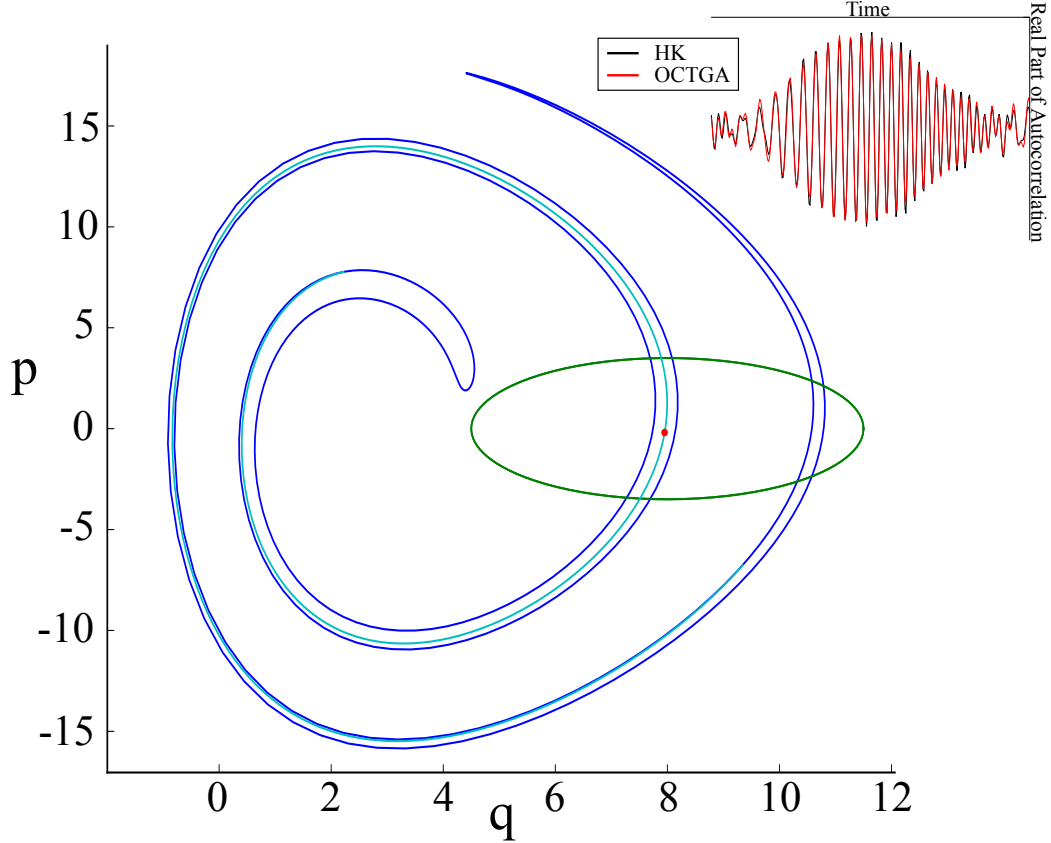

Figure 5.1: (Color onlline) The phase space $3.5\,\sigma$-confidence intervals of the initial (green) and final (blue) distributions with a one-dimensional manifold of trajectories (cyan) lying along the optimal off-center guiding points at the 3700th timestep. The (red) dot designates the off-center point chosen at that timestep. Inset: Real part of the twelfth recurrence of a Morse oscillator exhibiting multiple contributions from separate overlaps in phase space that differ in phase.

5.3 Sensitivity to "Off-Center" Guiding Trajectory

We consider the potential

$$V(\boldsymbol{q}) = D\left[1 - \exp(-\alpha(q - q_e))\right]^2 \tag{5.42}$$

where $D = 500$ is the Morse oscillator potential depth, $\alpha = 0.1$ is the bond rigidity, and q_e is the equilibrium bond length set to 3.0.
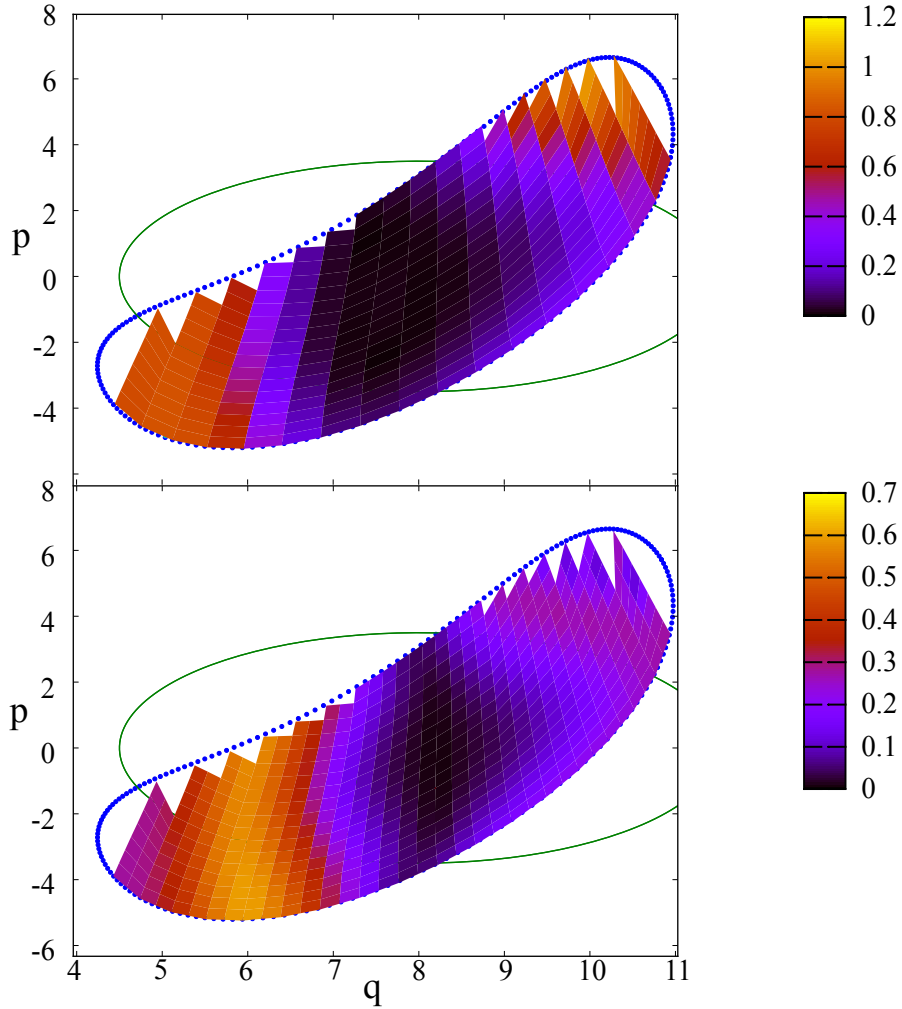

Figure 5.2: (Color online) Magnitude of the (a) real and (b) imaginary parts of the difference between the OCTGA-calculated autocorrelation and the analytical value at a particular timestep for different off-center guiding trajectories selected from within the classical distribution's 3.5 σ-interval.[16]

Finding the optimal off-center guiding trajectory for each overlap at a particular timestep can be considered to be a "soft" root search. By this it is meant that a rather wide region of points in phase space, generally grouped around the center of the overlap, can be used to produce an accurate second order potential. This is apparent in Figure 5.2 for the case of one Morse oscillator and makes the calculation much less sensitive to errors in selecting optimal guiding trajectories.

In this invesigation, this process was simplified as in Ref. [12] by only following a smaller one-dimensional manifold of trajectories in time (see Figure 5.1). These well-selected trajectories were monitored for intersection with the $3.5\,\sigma$-interval of the initial state. For all dimensions, this optimal manifold was found by examining each recurrence of the Gaussian with its initial state and searching for the phase space point at the center of its overlap during a series of timesteps through Monte Carlo sampling of trajectories. These phase space points were strung together in a list that was filled in through linear interpolation to form a manifold of trajectories.

5.4 Real-Trajectory Equivalence to vV.M.G

The cross- or auto-correlation from OCTGA can be described as the real-trajectory equivalent to the time-dependent W.K.B. approximation in coherent state representation, also known as generalized Gaussian wavepacket methods. This is discussed in more detail in [17]. Briefly, applying the method of steepest descents to the two integrals in:

$$\langle \Psi_\beta(q) \, | \Psi_\beta(q,t) \rangle_{\text{W.K.B.}} = \int_{-\infty}^{\infty} \mathrm{d}q'' \int_{-\infty}^{\infty} \mathrm{d}q' \Psi_\alpha(q'') G^{\text{vVMG}}(q'',q',t) \Psi_\beta(q'), \qquad (5.43)$$

results in

$$\Psi_\beta(q,t) = \frac{1}{\sqrt{\pi i \hbar \sigma}} \sum_{\text{saddle points}} \exp\left(\frac{i}{\hbar} S(q, q_0, t)\right) \tag{5.44}$$

$$\times \left\{ \left[\frac{1}{\sigma^2} - \frac{i}{2\hbar} \left(\frac{\partial^2 S}{\partial q^2}\right)_{q'} \right] \left[\frac{1}{\sigma^2} - \frac{i}{2\hbar} \left(\frac{\partial^2 S}{\partial q'^2}\right)_q \right] + \frac{1}{4\hbar^2} \left[\frac{\partial^2 S}{\partial q' \partial q}\right]^2 \right\}^{-\frac{1}{2}}$$

$$\times \exp\left[\frac{i}{2\hbar^2\sigma^2} \Re p_0 \Im p_0 - \frac{1}{4\hbar^2\sigma^2} (\Im p_0)^2 - \sigma^2 (\Im q_0)^2 - \frac{1}{\hbar} \Re p_0 \Im q_0 \right]$$

$$\times \exp\left[\frac{i}{2\hbar^2\sigma^2} \Re p_t \Im p_t - \frac{1}{4\hbar^2\sigma^2} (\Im p_t)^2 - \sigma^2 (\Im q_t)^2 + \frac{1}{\hbar} \Re p_t \Im q_t \right],$$

where now the sum is over all saddle points that satisfy

$$0 = \frac{2}{\sigma^2}(q_0 - q_\beta) + \frac{i}{\hbar}(p_0 - p_\beta), \tag{5.45}$$

and

$$0 = \frac{2}{\sigma^2}(q_t - q_\beta) - \frac{i}{\hbar}(p_t - p_\beta). \tag{5.46}$$

These saddle points are generally complex and can be considered to be the "best" guiding trajectories within such a quadratic (semiclassical) approximation.

Similarly, the position representation of OCTGA can be described as the real-trajectory equivalent to the time-dependent W.K.B. approximation in position state representation where the saddle points satisfy

$$0 = \frac{2}{\sigma^2}(q_0 - q_\beta) + \frac{i}{\hbar}(p_0 - p_\beta), \tag{5.47}$$

and

$$0 = q_t - q_\beta, \tag{5.48}$$

for p_0, and $q_0 \in \mathbb{C}$ and

$$
\Psi_\beta(q, t)
$$
$$
= \sqrt[4]{\frac{2}{\pi\sigma^2}} \sum_{\text{saddle points}} \frac{1}{\sqrt{\left(\frac{\partial^2 S}{\partial q_0^2}\right)_{q_t} + \frac{2i\hbar}{\sigma^2}}} \exp\left(\frac{i}{\hbar} S(q, q_0, t)\right) \tag{5.49}
$$
$$
\times \exp\left[\frac{i}{2\hbar^2\sigma^2}\Re p_0 \Im p_0 - \frac{1}{4\hbar^2\sigma^2}(\Im p_0)^2 - \sigma^2(\Im q_0)^2 - \frac{1}{\hbar}\Re p_0 \Im q_0\right].
$$

Again, the guiding trajectories we discussed in OCTGA can be formally considered to be the "best" or closest "real" ones to the generally complex classical saddle point trajectories in proper time-dependent W.K.B. Though no longer lying on the real axis, the latter are still often "nearly real" as a consequence.

5.5 Conclusion

In conclusion, we find that OCTGA can be a very fast, viable semiclassical propagation method for many-dimensional systems, at least as long as phase space areas of interest to approximation do not involve strongly curved regions. (We note that, as $\hbar \to 0$, the curvature problems vanish so OCTGA is already in the class of full semiclassical approximation.) This includes non-trivial many-body systems such as the coupled Morse oscillator chain model explored, and greatly opens up the field of feasible higher-dimensional systems, especially those that are integrable or mixed and are not amenable to Filinov filtering. In the approach taken in this chapter, the OCTGA relied on a well-chosen one-dimensional manifold of trajectories for selecting optimal "off-center" guiding trajectories and for its superior scaling with dimension. The development of methods for finding such manifolds, be they reliant on stability analysis or earlier recurrence analysis as in this Letter, is an important component necessary for the success of this semiclassical method in other systems of interest.

6 A Third Order Thawed Gaussian Approximation

The Feynman path integral provides a clear prescription for finding the quantum dynamics of states[18, 19]. Unfortunately, it is exactly solvable in only a few simple cases and so its semiclassical treatment is often considered instead. A variational expansion up to second order in $\hbar$ produces the time-dependent Wentzel-Kramers-Brillouin (W.K.B.) - the van Vleck-Morette-Gutzwiller (vV.M.G.) propagator[20, 21, 22] - which reduces the number of trajectories that are considered to the set of only the (real or complex) *classical* trajectories between two manifolds, along with their action S and stability $\partial^2 S/\partial q'\partial q$:

$$G^{\text{vVMG}}(q, q', t) = \frac{1}{\sqrt{2\pi i\hbar}} \sum_{\text{paths}} \left(\frac{\partial^2 S(q, q', t)}{\partial q\partial q'} \right)^{1/2} \exp\left[\frac{i}{\hbar}S(q, q', t) \right], \qquad (6.1)$$

where q' and q are the initial and final positions respectively for time t.

When considering the propagation of states in time whose representative classical densities are localized in phase space, such as coherent states (Gaussian wavepackets in position and momentum space), it is often useful to expand their semiclassical propagator around guiding time-dependent trajectories[4] that approximate the local parts of the state well that are of interest. When this expansion is done to quadratic order the dynamics near the guiding trajectory are linearized and the neighboring part of the wavepacket remains well approximated for all time for sufficiently small $\hbar$, or equivalently, for all $\hbar$ for a sufficiently short time. Even when the dynamics of the classical

density are globally highly non-linear in phase space, local pieces on the order of $\hbar$ can often still be linear and well captured, as has been shown for the Coulombic potential[23] and the stadium billiard[24].

However, for larger $\hbar$, non-linearities become important even at the local scale, and an expansion to higher than second order around the guiding trajectories becomes necessary. This was found in both prior studies where hairpins - highly curved manifolds - in phase space had to be avoided[23, 24] and is a general feature of almost any physically relevant system away from the classical regime. Therefore, there is a great need for a treatment that handles such pervasive non-linearity. Related efforts have relied on complex root-finding[25] or Monte Carlo uniformization[26] to address this issue.

Unfortunately, many expansions of this nature behave badly when taken to higher than second order and fewer still have closed-form simple solutions. Will including the dynamics up to third order be a non-asymptotic expansion and therefore actually produce less accurate results? Is it still possible, as in earlier work, to calculate correlations of wavepackets by summing periodic or heteroclinic orbit contributions based on their phase space intersections?

6.1 Derivation of the Cubic Approximation

To examine these questions we will work in one dimension and examine the time propagation of initial Gaussian wavepackets

$$\Psi_\beta(q,0) = \sqrt[4]{\frac{2}{\pi\sigma^2}} \exp\left\{\frac{i}{\hbar}\left[\xi\left(q-q_\beta\right) + \frac{i\hbar}{\sigma^2}\left(q-q_\beta\right)^2 + \gamma\right]\right\}. \tag{6.2}$$

$\sigma \in \mathbb{R}$ and is proportional to the spread of the Gaussian, $\Re\xi$ is equal to the central momentum while $\Im\xi$ describes p-q correlation, and $\gamma \in \mathbb{I}$ is an initial phase of the state.

Instead of the full semiclassical propagator, we apply the cubically approximated semiclassical (c.s.c.) propagator, $G^{\text{csc}}(q, q', t) = \sum_{\text{paths}} \exp\left[iS^{\text{cub}}(q, q', t)\right]$, to the initial state Ψ_β, giving

$$\Psi_\beta^{\text{csc}}(q, t) = \int dq' G^{\text{csc}}(q, q', t) \Psi_\beta(q', 0).$$ (6.3)

Here we have expanded the action $S(q, q')$ up to third order around an initial position q_0 and its time evolute q_t:

$$
\begin{aligned}
S^{\text{cub}}(q, q', t) &= S(q_t, q_0) + \left(\frac{\partial S}{\partial q_t}\right)_{q_0} Q + \left(\frac{\partial S}{\partial q_0}\right)_{q_t} Q' \\
&+ \frac{1}{2}\left(\frac{\partial^2 S}{\partial q_t^2}\right)_{q_0} Q^2 + \frac{1}{2}\left(\frac{\partial^2 S}{\partial q_0^2}\right)_{q_t} Q'^2 \\
&+ \left(\frac{\partial^2 S}{\partial q_0 \partial q_t}\right) Q'Q + \frac{1}{6}\left(\frac{\partial^3 S}{\partial q_0^3}\right)_{q_t} Q'^3 \\
&+ \frac{1}{6}\left(\frac{\partial^3 S}{\partial q_t^3}\right)_{q_0} Q^3 + \frac{1}{2}\left(\frac{\partial^3 S}{\partial q_0^2 \partial q_t}\right) Q'^2 Q \\
&+ \frac{1}{2}\left(\frac{\partial^3 S}{\partial q_0 \partial q_t^2}\right) Q'Q^2,
\end{aligned}
$$ (6.4)

where $Q = q - q_t$ and $Q' = q' - q_0$. This is the main extension over the harmonically approximated semiclassical (h.s.c.) propagator, and as we shall see in the following, the resulting formalism builds upon it.

Substituting the expanded action into Eq. 6.3 yields,

$$
\begin{aligned}
\Psi_\beta^{\text{csc}}(q, t) = \sqrt[4]{\frac{2}{\pi\sigma^2}} \frac{1}{\sqrt{2\pi i\hbar}} \sum_{\text{paths}} \int_{-\infty}^{\infty} dQ' &\left[\left(\sqrt{\frac{\partial^2 S}{\partial Q' \partial Q}}\right)_{Q'=Q=0}\right. \\
&+ \left(\frac{\frac{\partial^3 S}{\partial Q'^2 \partial Q}}{\sqrt{\frac{\partial^2 S}{\partial Q' \partial Q}}}\right)_{Q'=Q=0} Q' + \left.\left(\frac{\frac{\partial^3 S}{\partial Q' \partial Q^2}}{\sqrt{\frac{\partial^2 S}{\partial Q' \partial Q}}}\right)_{Q'=Q=0} Q\right] \\
&\times \exp\left\{\frac{i}{\hbar}\left[\Xi Q'^3 + \Upsilon Q'^2 + \Omega Q' + \Lambda\right]\right\}
\end{aligned}
$$ (6.5)

where

$$\Xi = \frac{1}{6}\left(\frac{\partial^3 S}{\partial q_0^3}\right)_{q_t}, \tag{6.6}$$

$$\Upsilon = \frac{1}{2}\left[\left(\frac{\partial^2 S}{\partial q_0^2}\right)_{q_t} + \left(\frac{\partial^3 S}{\partial q_0^2 \partial q_t}\right)Q\right] + \frac{i\hbar}{\sigma^2}, \tag{6.7}$$

$$\Omega = \left(\frac{\partial S}{\partial q_0}\right)_{q_t} + \left(\frac{\partial^2 S}{\partial q_0 \partial q_t}\right)Q + \left(\frac{\partial^3 S}{\partial q_0 \partial q_t^2}\right)Q^2$$
$$+ \frac{2i\hbar}{\sigma^2}(q_0 - q_\beta) + \xi, \tag{6.8}$$

and

$$\Lambda = S(q_t, q_0) + \left(\frac{\partial S}{\partial q_t}\right)_{q_0}Q + \frac{1}{2}\left(\frac{\partial^2 S}{\partial q_t^2}\right)_{q_0}Q^2 \tag{6.9}$$
$$+ \frac{1}{6}\left(\frac{\partial^3 S}{\partial q_t^3}\right)_{q_0}Q^3 + \frac{i\hbar}{\sigma^2}(q_0 - q_\beta)^2 + \xi(q_0 - q_\beta) + \gamma.$$

Above we have also expanded the prefactor to the next higher order around $q' = q_0$ and $q = q_t$ compared to the h.s.c. propagator; the h.s.c. propagator only contains the first term in this prefactor.

We let the phase in Eq. 6.5 be $f(Q', t)$ and the prefactor $g(Q', t)$ and then rewrite the former to fit the Airy function's cubic integral identity such that

$$\Psi_\beta^{\text{csc}}(q, t) = \sum_{\text{paths}} \int dQ' g(Q', t) \exp\left\{\frac{1}{\hbar}f(Q', t)\right\}, \tag{6.10}$$

where

$$f(Q', t) \tag{6.11}$$

$$= \Xi Q'^3 + \Upsilon Q'^2 + \Omega Q' + \Lambda \tag{6.12}$$

$$= \Xi \left(Q'^3 + \frac{\Upsilon}{\Xi} Q'^2 + \frac{\Omega}{\Xi} Q' + \frac{\Lambda}{\Xi} \right) \tag{6.13}$$

$$= \Xi \left[\left(Q' + \frac{1}{3} \frac{\Upsilon}{\Xi} \right)^3 - \frac{1}{3} \left(\frac{\Upsilon}{\Xi} \right)^2 Q' - \frac{1}{27} \left(\frac{\Upsilon}{\Xi} \right)^3 + \frac{\Omega}{\Xi} Q' + \frac{\Lambda}{\Xi} \right] \tag{6.14}$$

$$= \Xi \left[\left(Q' + \frac{1}{3} \frac{\Upsilon}{\Xi} \right)^3 - \frac{1}{27} \left(\frac{\Upsilon}{\Xi} \right)^3 + \frac{\Lambda}{\Xi} \right.$$
$$\left. + \left(\frac{\Omega}{\Xi} - \frac{1}{3} \left(\frac{\Upsilon}{\Xi} \right)^2 \right) \left(Q' + \frac{1}{3} \frac{\Upsilon}{\Xi} \right) - \frac{1}{3} \frac{\Upsilon}{\Xi} \left(\frac{\Omega}{\Xi} - \frac{1}{3} \left(\frac{\Upsilon}{\Xi} \right)^2 \right) \right], \tag{6.15}$$

and

$$g(Q', t) = \sqrt[4]{\frac{2}{\pi \sigma^2}} \frac{1}{\sqrt{2\pi i \hbar}} \left[\left(\sqrt{\frac{\partial^2 S}{\partial Q' \partial Q}} \right)_{Q'=Q=0} \right.$$
$$\left. + \left(\frac{\frac{\partial^3 S}{\partial Q'^2 \partial Q}}{\sqrt{\frac{\partial^2 S}{\partial Q' \partial Q}}} \right)_{Q'=Q=0} Q' + \left(\frac{\frac{\partial^3 S}{\partial Q' \partial Q^2}}{\sqrt{\frac{\partial^2 S}{\partial Q' \partial Q}}} \right)_{Q'=Q=0} Q \right]. \tag{6.16}$$

Thus, setting $z = -i \sqrt[3]{\frac{3}{\Xi^2}} \left(\Xi Q' + \frac{1}{3} \Upsilon \right)$ simplifies the phase such that

$$f = \frac{z^3}{3} - \zeta z + A, \tag{6.17}$$

where

$$\zeta = \sqrt[3]{\frac{\Xi^2}{3}} \left[\frac{\Omega}{\Xi} - \frac{1}{3} \left(\frac{\Upsilon}{\Xi} \right)^2 \right], \tag{6.18}$$

and

$$A = i \left\{ -\frac{1}{3} \Upsilon \left[\frac{\Omega}{\Xi} - \frac{1}{3} \left(\frac{\Upsilon}{\Xi} \right)^2 \right] - \frac{1}{27} \frac{\Upsilon^3}{\Xi^2} + \Lambda \right\}. \tag{6.19}$$

Substituting in z changes the contour integral:

$$\Psi_\beta^{\mathrm{csc}}(q,t) = \sum_{\mathrm{paths}} \int_{-i\sqrt[3]{\frac{3}{\Xi^2}}\left(-\Xi\infty+\frac{1}{3}\Upsilon\right)}^{-i\sqrt[3]{\frac{3}{\Xi^2}}\left(\Xi\infty+\frac{1}{3}\Upsilon\right)} dz \tag{6.20}$$

$$\times g\left(Q'(z),t\right)\frac{dQ'}{dz}\exp\left[\frac{1}{\hbar}\left(\frac{z^3}{3}-\zeta z+A\right)\right].$$

This is a convergent integral when $\frac{\pi}{6} < \arg(z) < \frac{\pi}{2}$, $\frac{5\pi}{6} < \arg(z) < \frac{7\pi}{6}$, or $\frac{3\pi}{2} < \arg(z) < \frac{11\pi}{6}$ as $|z| \to \pm\infty$. These conditions are satisfied since $\Xi \in \mathbb{R}$ and $\Im\Upsilon = \frac{1}{\sigma^2} > 0$. Depending on the root of $\Xi^{-\frac{2}{3}}$, the possible contours of integration are equivalent to C_1 from $\infty e^{-\frac{1}{3}\pi i}$ to $\infty e^{\frac{1}{3}\pi i}$, C_2 from $\infty e^{\frac{1}{3}\pi i}$ to $\infty e^{\pi i}$, and C_3 from $\infty e^{\pi i}$ to $\infty e^{-\frac{1}{3}\pi i}$.

It remains to evaluate the integrals

$$F(\zeta,\hbar,C_j) = \frac{1}{2\pi i}\int_{C_j} dz\,\exp\left[\frac{1}{\hbar}\left(\frac{z^3}{3}-\zeta z\right)\right], \tag{6.21}$$

$$G(\zeta,\hbar,C_j) = \frac{1}{2\pi i}\int_{C_j} dz\,z\,\exp\left[\frac{1}{\hbar}\left(\frac{z^3}{3}-\zeta z\right)\right]. \tag{6.22}$$

The contours of integration ensure that each $F(C_j)$ and $G(C_j)$ is linearly dependent on the other two[2] such that

$$F(\zeta,\hbar,C_1) + F(\zeta,\hbar,C_2) + F(\zeta,\hbar,C_3) = 0, \tag{6.23}$$

and the same with G.

Furthermore,

$$F(\zeta,\hbar,C_2) = \exp\left(\frac{2}{3}\pi i\right)F(\zeta e^{\frac{2}{3}\pi i},\hbar,C_1), \tag{6.24}$$

$$G(\zeta,\hbar,C_2) = \exp\left(\frac{4}{3}\pi i\right)G(\zeta e^{\frac{2}{3}\pi i},\hbar,C_1), \tag{6.25}$$

and

$$F(\zeta, \hbar, C_3) = \exp\left(\frac{2}{3}\pi i\right) F(\zeta e^{\frac{2}{3}\pi i}, \hbar, C_2), \tag{6.26}$$

$$G(\zeta, \hbar, C_3) = \exp\left(\frac{4}{3}\pi i\right) G(\zeta e^{\frac{2}{3}\pi i}, \hbar, C_2). \tag{6.27}$$

With these identities, the contour integrals in Eqs 6.21 and 6.22 can be evaluated, and their results are shown in Table 6.1.

j	$F(\zeta, \hbar, C_j)$	$G(\zeta, \hbar, C_j)$
1	$\hbar^{\frac{1}{3}}\, \mathscr{Ai}\left(\frac{\zeta}{\hbar^{\frac{2}{3}}}\right)$	$-\hbar^{\frac{2}{3}}\, \mathscr{Ai}'\left(\frac{\zeta}{\hbar^{\frac{2}{3}}}\right)$
2	$e^{\frac{4\pi i}{3}}\hbar^{\frac{1}{3}}\, \mathscr{Bi}\left(\frac{e^{\frac{2\pi i}{3}}\zeta}{\hbar^{\frac{2}{3}}}\right)$	$-e^{\frac{4\pi i}{3}}\hbar^{\frac{2}{3}}\, \mathscr{Bi}'\left(\frac{e^{\frac{2\pi i}{3}}\zeta}{\hbar^{\frac{2}{3}}}\right)$
3	$-\hbar^{\frac{1}{3}}\left[\mathscr{Ai}\left(\frac{\zeta}{\hbar^{\frac{2}{3}}}\right) + e^{\frac{4\pi i}{3}}\, \mathscr{Bi}\left(\frac{e^{\frac{2\pi i}{3}}\zeta}{\hbar^{\frac{2}{3}}}\right) \right]$	$\hbar^{\frac{2}{3}}\left[\mathscr{Ai}'\left(\frac{\zeta}{\hbar^{\frac{2}{3}}}\right) + e^{\frac{4\pi i}{3}}\, \mathscr{Bi}'\left(\frac{e^{\frac{2\pi i}{3}}\zeta}{\hbar^{\frac{2}{3}}}\right) \right]$

Table 6.1:

In summary,

$$\Psi_\beta^{\text{csc}}(q,t) \tag{6.28}$$

$$= \sum_{\text{paths}} \int_C \mathrm{d}z \, g(Q'(z),t) \frac{\mathrm{d}Q'}{\mathrm{d}z} \exp\left[\frac{1}{\hbar}\left(\frac{z^3}{3} - \zeta z + A\right)\right] \tag{6.29}$$

$$= \sum_{\text{paths}} \int_C \mathrm{d}z \, \sqrt[4]{\frac{2}{\pi\sigma^2}} \frac{1}{\sqrt{2\pi i \hbar}} \frac{-i}{\sqrt[3]{3\Xi}} \left[\left(\sqrt{\frac{\partial^2 S}{\partial Q' \partial Q}}\right)_{Q'=Q=0}\right. \tag{6.30}$$

$$+ \left(\frac{\frac{\partial^3 S}{\partial Q' \partial Q^2}}{\sqrt{\frac{\partial^2 S}{\partial Q' \partial Q}}}\right)_{Q'=Q=0} Q + \left(\frac{\frac{\partial^3 S}{\partial Q'^2 \partial Q}}{\sqrt{\frac{\partial^2 S}{\partial Q' \partial Q}}}\right)_{Q'=Q=0} \left(\frac{i}{\sqrt[3]{3\Xi}} z - \frac{\Upsilon}{3\Xi}\right)\right]$$

$$\times \exp\left[\frac{1}{\hbar}\left(\frac{z^3}{3} - \zeta z + A\right)\right]$$

$$= (2\pi i) \sum_{\text{paths}} \sqrt[4]{\frac{2}{\pi\sigma^2}} \frac{1}{\sqrt{2\pi i \hbar}} \frac{-i}{\sqrt[3]{3\Xi}} \left\{\left[\left(\sqrt{\frac{\partial^2 S}{\partial Q' \partial Q}}\right)_{Q'=Q=0}\right.\right. \tag{6.31}$$

$$+ \left(\frac{\frac{\partial^3 S}{\partial Q' \partial Q^2}}{\sqrt{\frac{\partial^2 S}{\partial Q' \partial Q}}}\right)_{Q'=Q=0} Q - \frac{\Upsilon}{3\Xi}\left(\frac{\frac{\partial^3 S}{\partial Q'^2 \partial Q}}{\sqrt{\frac{\partial^2 S}{\partial Q' \partial Q}}}\right)_{Q'=Q=0}\right] F(\zeta,\hbar,C_j)$$

$$\left. + \frac{i}{\sqrt[3]{3\Xi}}\left(\frac{\frac{\partial^3 S}{\partial Q'^2 \partial Q}}{\sqrt{\frac{\partial^2 S}{\partial Q' \partial Q}}}\right)_{Q'=Q=0} G(\zeta,\hbar,C_j)\right\} \exp\left(\frac{A}{\hbar}\right)$$

where C_j runs from $-i\sqrt[3]{\frac{3}{\Xi^2}}\left(\Xi\infty + \frac{1}{3}\Upsilon\right)$ to $-i\sqrt[3]{\frac{3}{\Xi^2}}\left(-\Xi\infty + \frac{1}{3}\Upsilon\right)$.

$F(\zeta,\hbar,C_1)\exp\left(\frac{A}{\hbar}\right)$ can be written in a form that makes its Q-dependence explicit:

$$\mathscr{A}(\alpha Q^2 + \beta Q + \gamma) \exp\left[i\left(\delta Q^3 + \epsilon Q^2 + \zeta Q + \eta\right)\right], \tag{6.32}$$

where $\beta, \gamma, \epsilon, \zeta, \eta \in \mathbb{C}$ and $\alpha, \delta \in \mathbb{I}$ (see the Appendix for their explicit form.)

In this way, it can be seen that the final solution in Eq. 6.31 is linear combination of an Airy function and its derivative, with complex quadratic arguments in Q, multiplied by a Gaussian with a cubic imaginary term.

In this paper, all examples are found to maintain normalization except when the wavepacket is at turning points. At these instances, the prefactor diverges due to the branch cut of the prefactor's square root function (which is not an entire function) overlapping with the center of the initial wavepacket around which its expansion in Q' is made. The quadratic approximation does not suffer from this effect; it only expands the prefactor to its zeroth order, and so is not dependent on which side of the branch cut the expansion is made. Remedying this inconvenience, while still relying on only real trajectories, is clearly of future interest to this study.

Due to the variable transformation necessary to produce the Airy function form, it is numerically necessary that $\Xi^2 \not\ll (\Omega - \Xi\Upsilon^2)$ or, more loosely, that the triple derivatives of the trajectories' action cannot be much smaller than the second order derivatives with respect to the Gaussian's dispersion σ, in order for the Airy functions' arguments not to be very large. This is never the case early in a wavepacket's propagation when its dynamics are exactly linearizable. As a consequence, in practice, early on in the dynamics the argument for the Airy function is a very large number and only later in the dynamics does this form become usable, as numerical evaluation readily shows.

As a final point on practical implementation, in numerics it is important to watch the sign of the argument $\partial^2 S/\partial q_0 \partial q_t$ in the square roots of the prefactor so that the roots propagate continuously on their Riemannian surface across branch cuts. This is equivalent to adding the correct Maslov or Morse index into the formulation.

6.2 Stability Matrices and Their Derivatives

The double action derivatives are often most easily found in terms of the elements of the stability matrix,

$$
M(t) = \begin{pmatrix} M(t)_{11} & M(t)_{12} \\ M(t)_{21} & M(t)_{22} \end{pmatrix} = \begin{pmatrix} \left(\frac{\partial p_t}{\partial p_0}\right)_{q_0} & \left(\frac{\partial p_t}{\partial q_0}\right)_{p_0} \\ \left(\frac{\partial q_t}{\partial p_0}\right)_{q_0} & \left(\frac{\partial q_t}{\partial q_0}\right)_{p_0} \end{pmatrix}.
\tag{6.33}
$$

These are more convenient since they are dependent on the initial position and momentum instead of the initial and final positions. In terms of M, the double action derivative are:

$$
\left(\frac{\partial^2 S}{\partial q_0^2}\right)_{q_t} = \frac{M_{22}}{M_{21}}, \quad \frac{\partial^2 S}{\partial q_0 \partial q_t} = -\frac{1}{M_{21}}, \quad \text{and} \quad \left(\frac{\partial^2 S}{\partial q_t^2}\right)_{q_0} = \frac{M_{11}}{M_{21}},
\tag{6.34}
$$

where we dropped the stability matrix's t argument for brevity's sake and $M(t=0) = \mathbb{I}_{2\times 2}$.

The stability matrix of the guiding trajectory $(q_0, q_t) = (p_t, q_t)$ obeys the symplectic equation of motion

$$
\dot{M}(t) = K(t) \cdot M(t),
\tag{6.35}
$$

where

$$
K(t) = \begin{pmatrix} -\frac{\partial^2 H}{\partial q \partial p} & -\frac{\partial^2 H}{\partial q^2} \\ \frac{\partial^2 H}{\partial p^2} & \frac{\partial^2 H}{\partial p \partial q} \end{pmatrix}.
\tag{6.36}
$$

Similarly, the triple derivatives of the action can often most easily be found in terms of the elements of the stability matrix and its first derivative $\Gamma(t) \equiv \frac{\partial M}{\partial (p_0, q_0)}$, a $2 \times 2 \times 2$ tensor. The equation of motion for $\Gamma(t)$ can be shown to be:

$$
\dot{\Gamma}(t)_{ilm} = \sum_{j,k} \frac{\partial K(t)}{\partial (p,q)_{ijk}} M(t)_{kl} M(t)_{jm} + \sum_j K(t)_{ij} \Gamma(t)_{jlm},
\tag{6.37}
$$

where

$$
\frac{\partial K(t)}{\partial p} = \begin{pmatrix} -\frac{\partial^3 H}{\partial q \partial p^2} & -\frac{\partial^3 H}{\partial q^2 \partial p} \\ \frac{\partial^3 H}{\partial p^3} & \frac{\partial^3 H}{\partial q \partial p^2} \end{pmatrix} \quad \text{and} \quad \frac{\partial K(t)}{\partial q} = \begin{pmatrix} -\frac{\partial^3 H}{\partial q^2 \partial p} & -\frac{\partial^3 H}{\partial q^3} \\ \frac{\partial^3 H}{\partial p^2 \partial q} & \frac{\partial^3 H}{\partial q^2 \partial p} \end{pmatrix}.
\tag{6.38}
$$

In terms of the Γ tensor, the triple action derivatives are:

$$\frac{\partial^3 S}{\partial q_0^3} = \frac{1}{M_{21}}\Gamma_{222} - 2\frac{M_{22}}{(M_{21})^2}\Gamma_{221} + \frac{(M_{22})^2}{(M_{21})^3}\Gamma_{211}, \tag{6.39}$$

$$\frac{\partial^3 S}{\partial q_0^2 \partial q_t} = \frac{1}{(M_{21})^2}\left(\Gamma_{212} - \frac{M_{22}}{M_{21}}\Gamma_{211}\right), \tag{6.40}$$

$$\frac{\partial^3 S}{\partial q_t^3} = \frac{1}{(M_{21})^2}\left(\Gamma_{111} - \frac{M_{11}}{M_{21}}\Gamma_{211}\right), \tag{6.41}$$

$$\frac{\partial^3 S}{\partial q_0 \partial q_t^2} = \frac{\Gamma_{211}}{(M_{21})^3}, \tag{6.42}$$

and $\Gamma(0) = 0 \times \mathbb{I}_{2\times2\times2}$.

In many applications there is often no need to maintain strict symplecticity or conservation of the area of phase space when calculating $\Gamma(t)$. Instead, it can be found by numerical approximation to an acceptable accuracy, such as perhaps by a finite difference evaluation from two stability matrices for two trajectories, with initial conditions slightly displaced from each other. This is especially important for applications in "on-the-fly" calculations, where the stability matrix is computed by *ab-initio* methods and generally relies on an expensive calculation of the system's Hessian matrix to find $K(t)$. Thus, for instance, using a finite difference computational approach would be expected to double the amount of Hessians that must be computed. This is still a far cry from the many more that are necessary, one for each trajectory's stability matrix, in contemporary "initial-value methods" such as the Herman-Kluk propagator.

6.3 Performance of the Cubic Approximation

To begin evaluating the performance of the cubic approximation just derived, we examine the first return of an initially displaced and kicked coherent state with $\sigma = 0.5$, $q_\beta = 1$ and $p_\beta = -300$, under the Hamiltonian $H = \frac{p^2}{2m} + \omega|q^3|$ with $m = 1$, $\omega = 10000$. Notice that although trajectories under this system's evolution have higher than triple action derivatives, the triple derivatives dominate in a regime of $\hbar$ and σ. For the results shown, the guiding trajectory (p_t, q_t) was chosen to be the center of mass of the initial state at $t = 0$ since, in the early timescale examined, the states

do not appreciably stretch so as to necessarily warrant "off-centered" trajectories to approximate them adequately. Furthermore, the initial spread σ was set such that the state's manifold exhibited significant cubic curvature after its first orbit. Decreasing σ allows the quadratic approximation to perform better in the time period shown as less of the density in phase space develops curvature, whereas increasing σ leads both the quadratic and cubic approximations to perform badly as higher than cubic curvature dominates the state's dynamics.

As it completes an orbit, the wavepacket nearly reforms to a Gaussian state as it collides off the near wall and, as Figure 6.1 shows, it then develops highly oscillatory anharmonic features as it travels again to the far wall. While the quadratic approximation captures its center of mass motion well, it is clearly unable to reproduce the non-linear oscillations. The cubic approximation is able to capture these features far more successfully.

The real part of the numerically evaluated autocorrelation during this time period is shown in Figure 6.2a and similarly shows that the quadratic expansion is able to capture the overall general envelope well, but unlike the cubic approximation, is unable to reproduce the chirp in the frequency during the recurrence, as well as the variations in its envelope.

Immediately before the first recurrence shown in Figure 6.2a, the cubic approximation diverges as the wavepacket hits the near wall. This is apparent in its divergent normalization around $t = 330$ shown in the second lowest panel of Figure 6.2a as well as in the divergent peak at the same time point in its autocorrelation one panel above. This occurs for the reasons already described, namely that at turning points the cubic approximation's prefactor diverges.

As indicated in the earlier derivation, the second and third order calculations both rely on a guiding trajectory at each time step. Figure 6.2b shows the 3.5-σ confidence interval of the initial classical Gaussian distribution and its final time evolute at the time $t = 375$ in the middle of the recurrence. Also shown are the equivalent confidence intervals generated from quadratically and cubically expanding the potential around the guiding trajectory (indicated by 'x') at every timestep at the center of mass of the wavepacket. The deviation of the cubically approximated density from the exact density is due to the triple derivative discontinuity of the potential around $q = 0$.

The tails of the Gaussian off the central guiding trajectory increasingly deviate from their exact evolution with time because the third order expansion around the guiding trajectory gets the sign of the potential wrong on the other side of q=0 at every timestep.

The cubic approximation is expected to be superior to the quadratic one only for intermediate value of $\hbar$ when the cubic curvature of the state's manifold in phase space becomes significant. For larger values of $\hbar$ when higher orders for curvature become important, it is expected to only be nominally better. On the other hand, as $\hbar \to 0$, the quadratic expansion should become exact. This can be seen in the inset of Fig 6.2b where the error of the two methods using the same guiding trajectory is plotted. Notice also that as $\hbar \to 0$ the error in the cubic approximation eventually diverges as the magnitude of the double action derivatives in the Airy function's argument become comparatively too large for the function to be properly numerically evaluated.

6.4   Method of Steepest Descents

An alternative quadratic approximation to

$$\Psi_\beta(q,t) = \int \mathrm{d}q' G^{\mathrm{vVMG}}(q,q',t)\Psi_\beta(q',0),\tag{6.43}$$

is by the method of steepest descents[27, 28, 29, 30]. This is equivalent to the quadratic expansion already presented, except that the guiding centers are the saddle points of the integrand - where the first derivative of the phase is equal to zero - and is thus on a far more formally solid footing. In other words, the expansion of the action in Eq. 6.5 is made around the saddle phase space points of the integrand, which are generally complex trajectories (p_t, q_t), obeying double-ended boundary conditions. Generally, these must be found by root finding. The result, the mixed coherent state/position representation of the time-dependent W.K.B. approximation, also the position representation of what is called generalized Gaussian wavepacket dynamics

(G.G.W.P.D.)[31, 32], is

$$
\Psi_\beta(q, t)
$$

$$
= \sqrt[4]{\frac{2}{\pi \sigma^2}} \sum_{\text{saddle points}} \frac{1}{\sqrt{\left(\frac{\partial^2 S}{\partial q_0^2}\right)_{q_t} + \frac{2i\hbar}{\sigma^2}}} \exp\left(\frac{i}{\hbar} S(q, q_0, t)\right) \tag{6.44}
$$

$$
\times \exp\left[\frac{i}{2\hbar^2\sigma^2} \Re p_0 \Im p_0 - \frac{1}{4\hbar^2\sigma^2} (\Im p_0)^2 - \sigma^2 (\Im q_0)^2 - \frac{1}{\hbar} \Re p_0 \Im q_0\right]
$$

where the sum is over all saddle points that satisfy

$$
0 = \frac{2}{\sigma^2}(q_0 - q_\beta) + \frac{i}{\hbar}(p_0 - p_\beta), \tag{6.45}
$$

and

$$
0 = q_t - q_\beta, \tag{6.46}
$$

for p_0, and $q_0 \in \mathbb{C}$.

The result of the steepest descents integration applied to the prior absolute cubic potential is shown in the third column of Figure 6.1. There it is clear that the G.G.W.P.D. wavepacket hews closely to the exact evolution but exhibits a spurious peak to the right at the caustic. We included the two expected saddle point contributions in this calculation. It is possible that the spurious peak is due to one of the saddle points crossing a Stokes line and becoming divergent, but we find that unlikely. We believe that these saddle points become too close together (with respect to $\hbar$) at the right of the wavefunction, such that G.G.W.P.D. needs to be "uniformized" to capture the interference effect they add without behaving badly. The cubic approximation, on the other hand, is able to capture both of the contributions caused by the curvature automatically with one trajectory.

The quadratic approximation has been recently argued to be an approximation to W.K.B., where the latter's complex trajectories are approximated by the closest real trajectory[17]. In other words, the guiding trajectories can be considered to be real-trajectory approximations to the original integrand's saddle point trajectories that are used to obtain G.G.W.P.D.

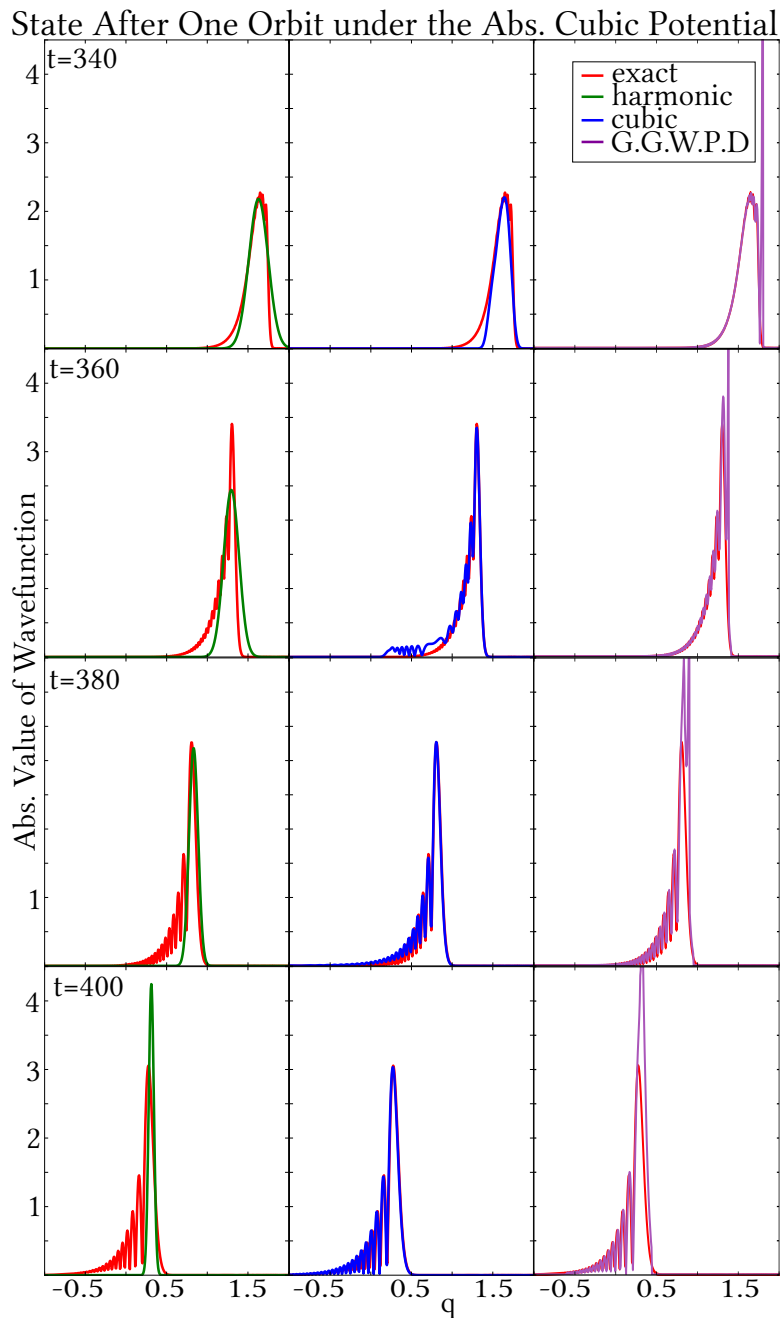**State After One Orbit under the Abs. Cubic Potential**

Figure 6.1: The first recurrence of the wavepacket with its initial coherent state in the absolute value cubic potential described inline. At $t = 340$ the wavepacket has just reflected off of the right wall and is fairly Gaussian in appearance. As it proceeds back across the potential at $t = 360$ to $t = 400$, the absolute value of its wavefunction becomes far more assymetric and oscillatory. The cubic approximation to this evolution, expanded around the classical guiding trajectory at the center of the wavepacket, appears to be able to capture this latter behavior far better than the quadratic approximation and G.G.W.P.D.
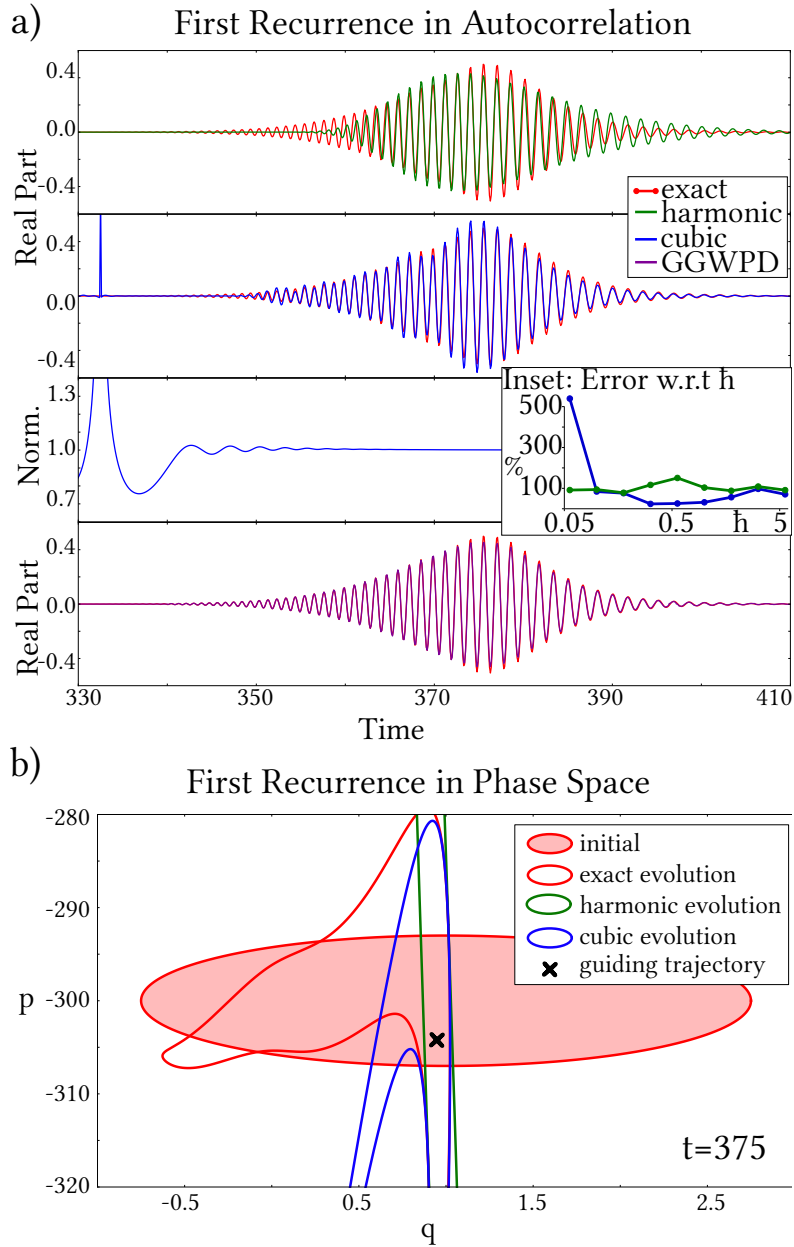
Figure 6.2: For the cubic potential described in text with timestep $\Delta t = 8 \times 10^{-5}$. a) The first recurrence in the autocorrelation of this state is compared between the full quantum result and the semiclassical quadratic (first panel) and cubic (second panel) approximations. The cubic autocorrelation diverges from unit normalization immediately before the recurrence when the wavepacket bounces against the near wall, as can be seen in the third panel. In the last panel, the G.G.W.P.D. simulation of this recurrence is shown and exhibits excellent agreement with the exact autocorrelation except for a slight underestimation of the amplitude. b) The 3.5-σ confidence intervals of the initial and final states in classical phase space are shown around the time of the middle of the recurrence. Along with the full time evolution, also shown is the quadratically and cubically approximated evolution of the state around the guiding trajectory marked by 'x'. (Inset: The error $|C_\beta^{\text{c.s.c./h.s.c}}(t) - C_\beta(t)|/|C_\beta(t)|$ averaged over the $t = 350$ to $t = 400$ for different values of $\hbar$ plotted on a logarithmic scale with $\sigma/\hbar$ kept fixed.)

As an aside, it is likely possible to formulate a superior steepest descents equivalent to the cubic approximation presented herein, in the same way that G.G.W.P.D. is the superior steepest descents equivalent of the quadratic approximation (also known as the off-center "thawed Gaussian approximation"). Such a formulation would be a uniformization, in that it would properly handle two (or more) coalescing saddle phase space points, which are the marker of phase space curvature, in a uniform manner. Again, the cubic approximation presented herein could be interpreted as a real-trajectory approximation to such a uniform steepest descents treatment, the latter of which would instead generally involve complex trajectory root finding of what would now be two stationary phase points.

We choose to examine G.G.W.P.D.'s approximation of the autocorrelation during the first recurrence by taking advantage of the analytically known steepest descents integral of Eq. 6.45 with a coherent state. This is because the numerical evaluation of the integral, which is what we examined for the quadratic and cubic approximations to the autocorrelation examined so far, is comparably difficult to perform due of the necessity of finding the correct roots for each q-point at every timestep. In any case, such a steepest descents evaluation produces the coherent state representation of time-dependent W.K.B. or G.G.W.P.D. and is:

$$\Psi_\beta(q,t) = \frac{1}{\sqrt{\pi i \hbar \sigma}} \sum_{\text{saddle points}} \exp\left(\frac{i}{\hbar} S(q, q_0, t)\right) \tag{6.47}$$

$$\times \left\{ \left[\frac{1}{\sigma^2} - \frac{i}{2\hbar}\left(\frac{\partial^2 S}{\partial q^2}\right)_{q'}\right] \left[\frac{1}{\sigma^2} - \frac{i}{2\hbar}\left(\frac{\partial^2 S}{\partial q'^2}\right)_q\right] + \frac{1}{4\hbar^2}\left[\frac{\partial^2 S}{\partial q' \partial q}\right]^2 \right\}^{-\frac{1}{2}}$$

$$\times \exp\left[\frac{i}{2\hbar^2\sigma^2}\Re p_0 \Im p_0 - \frac{1}{4\hbar^2\sigma^2}(\Im p_0)^2 - \sigma^2(\Im q_0)^2 - \frac{1}{\hbar}\Re p_0 \Im q_0\right]$$

$$\times \exp\left[\frac{i}{2\hbar^2\sigma^2}\Re p_t \Im p_t - \frac{1}{4\hbar^2\sigma^2}(\Im p_t)^2 - \sigma^2(\Im q_t)^2 + \frac{1}{\hbar}\Re p_t \Im q_t\right],$$

where now the sum is over all saddle points that satisfy

$$0 = \frac{2}{\sigma^2}(q_0 - q_\beta) + \frac{i}{\hbar}(p_0 - p_\beta), \tag{6.48}$$

and

$$0 = \frac{2}{\sigma^2}(q_t - q_\beta) - \frac{i}{\hbar}(p_t - p_\beta). \tag{6.49}$$

The last panel of Figure 6.2a shows that G.G.W.P.D. is able to capture the third recurrence very well. Its only apparent deviation from the exact autocorrelation can be found in its amplitude, which is slightly too low. We attribute this underestimation of the amplitude the fact that we only included one saddle point in the sum of Eq. 6.47 at every timestep in Figure 6.2a, unlike before when we examined G.G.W.P.D. in its position representation. Investigation of nearby complex trajectory space reveals the other expected saddle point but it was found contribute badly to the middle of the recurrence in the autocorrelation. For this reason, it was not included. Again, we believe its bad behavior is due to its coalescence together with the saddle point we use between $t = 370$ and $t = 380$, leading to a badly behaved contribution in the steepest descents integration that produces G.G.W.P.D.

6.5   Guiding Trajectories

The quadratic approximation's accuracy has often been found to be rather insensitive to the selection of an appropriate real guiding trajectory. In fact, many results[33, 34] have been obtained only using the central trajectory of the initial coherent state as the guiding trajectory, as we also did for the results shown in Figs. 6.1 and 6.2. However, when the dynamics of the state become more anharmonic, the selection of an "off-center" guiding trajectory becomes more important.
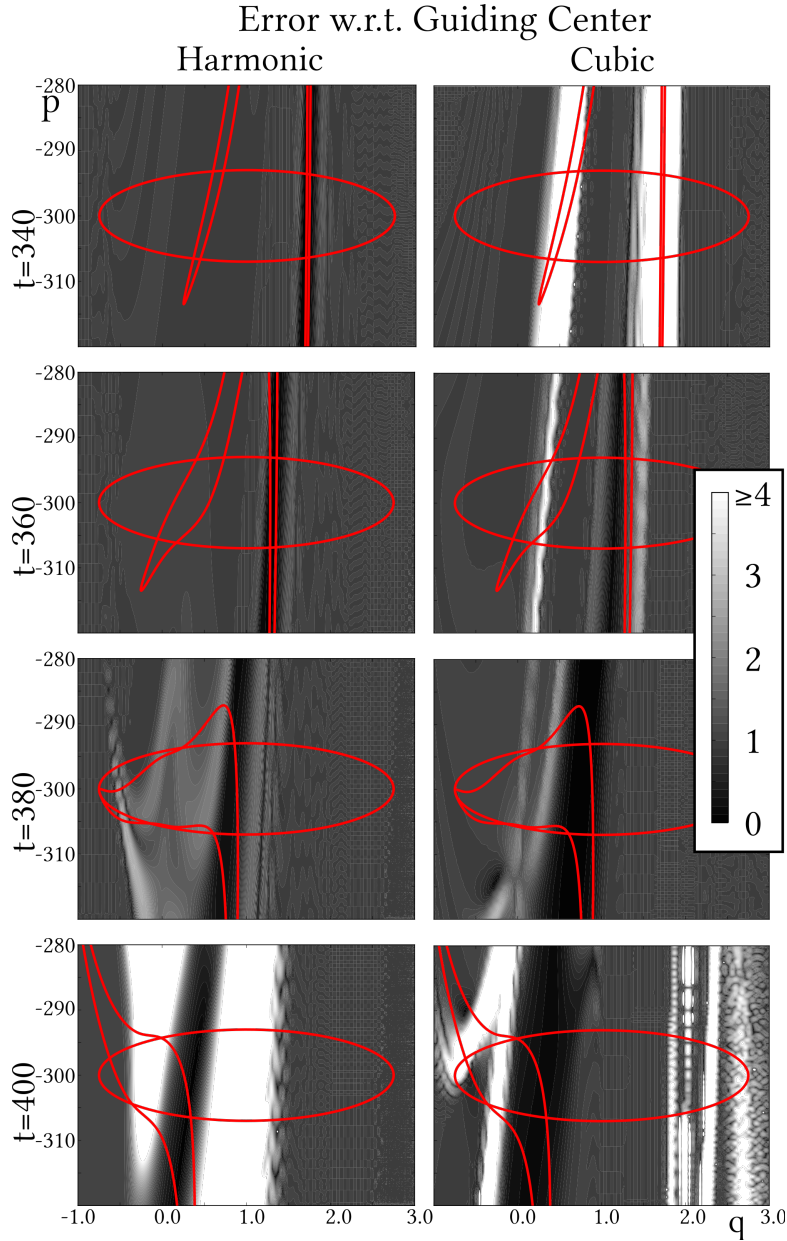
Figure 6.3: Error, $\frac{|C_\beta^{hsc/csc}(t) - C_\beta(t)|}{|C_\beta(t)|}$, for guiding trajectories (p_t, q_t) ending at the phase space point indicated for the timestep shown in Figure 6.2. Darker regions correspond to guiding trajectories that lead to the most accurate approximation of the overlap while lighter regions correspond to poorer trajectories. As can be seen in this side-by-side comparison between the quadratic and cubic approximations, while the area in phase space acceptable from which the quadratic approximation's guiding center can be placed is quite consistent and appears almost Gaussian-shaped itself, it is significantly more variable for the cubic case. In particular, the cubic approximation's valid guiding center area is smallest when it is least applicable immediately after a turning point and is largest when the third order action derivatives dominate over all others.

The overlap in phase space of the classical density corresponding to the wavepacket with its initial self during the four times indicated in Figure 6.1 are shown in Figure 6.3. Their 3.5-σ confidence intervals are draw in red in both columns over underlying contour plots of the error in approximating the first recurrence from using different guiding trajectories. They show that at $t = 340$ only the far-flung tails of the classical density has passed through its initial self, while at $t = 380$ the wavepacket has rotated and its central highest density is now sweeping through. Finally, at $t = 400$, the central density is seen exiting the initial 3.5-σ confidence interval.

The shading of Figure 6.3's contour plots corresponds to the error in the first recurrence of the wavepacket propagated by a guiding trajectory that ends at the phase space point (p_t, q_t) indicated by the abscissas and ordinates. The lighter the shading, the greater the error, or equivalently, the poorer the corresponding guiding trajectory (p_t, q_t) fares at capturing the overlap at the timestep shown. The left column shows the error from the quadratic expansion at the guiding trajectories while the right column shows the cubic expansion's error.

As expected, the region of good candidate guiding trajectories (p_t, q_t) is quite consistently broad for the quadratic approximation and seems to itself be fairly Gaussian in shape. Selecting a better guiding trajectory than the center of the wavepacket from these darker phase space regions does greatly improve the quadratic approximation's autocorrelation for the first half of the recurrence shown in Figure 6.2, a procedure that is unecessary for the cubic approximation, which fares just fine with the central guiding trajectory.

On the other hand, the cubic approximation's region of good candidate trajectories (p_t, q_t) indicated by the growing black area appears to be highly variable in shape and size. At $t = 340$ the cubic approximation is still suffering the late effects of its divergence at the preceding caustic and has only a very thin black region around $q = 1.3$. This region grows dramatically with time, dwarfing the corresponding quadratic approximation's area during the time period when the cubic approximation is seen to most closely approach the exact propagation in Figure 6.1. This suggests that when the cubic approximation is performing best, it is more insensitive to "incorrect" guiding trajectories compared to the quadratic approximation, and vice-versa.

6.6 Sum Over Individual Contributions

As time increases, growing numbers of periodic or heteroclinic orbits usually intersect with an area in phase space. Adding all of them with appropriate phases, from a manifold of guiding trajectories, is necessary to approximate the full wavepacket. This sum is the real-trajectory equivalent to the saddle point sum formally present in G.G.W.P.D. in Eq. 6.45 and Eq. 6.47. The quadratically expanded propagator has been shown to handle this properly, as mentioned before in the cases of the Coulombic potential and the stadium billiard. However, as stated, when these individual contribution are highly curved themselves (appearing as hairpins in phase space), the quadratic approximation struggles. This is clear in Figure 6.4, which shows the autocorrelation at some time interval for an initial coherent state evolving under a Morse potential - often used to realistically model the anharmonicity in molecular vibrational bonds. Figure 6.4a shows the absolute value of the autocorrelation while Figure 6.4b shows the real part. The inset shows the confidence intervals of the classical density of the initial wavepacket and its time evolute during the autocorrelation examined. Apparent in this inset are the trajectories contributing to the autocorrelation at that timestep, of which representative ones are indicated by the black 'x's. Using these as the guiding trajectories for the quadratic approximation produces a rather poor fit to the exact curves. On the other hand, the cubic approximation is able to reproduce the autocorrelation far better as is clear in this Figure. Each contribution is added with the correct relative phase with respect to the others along with its amplitude.
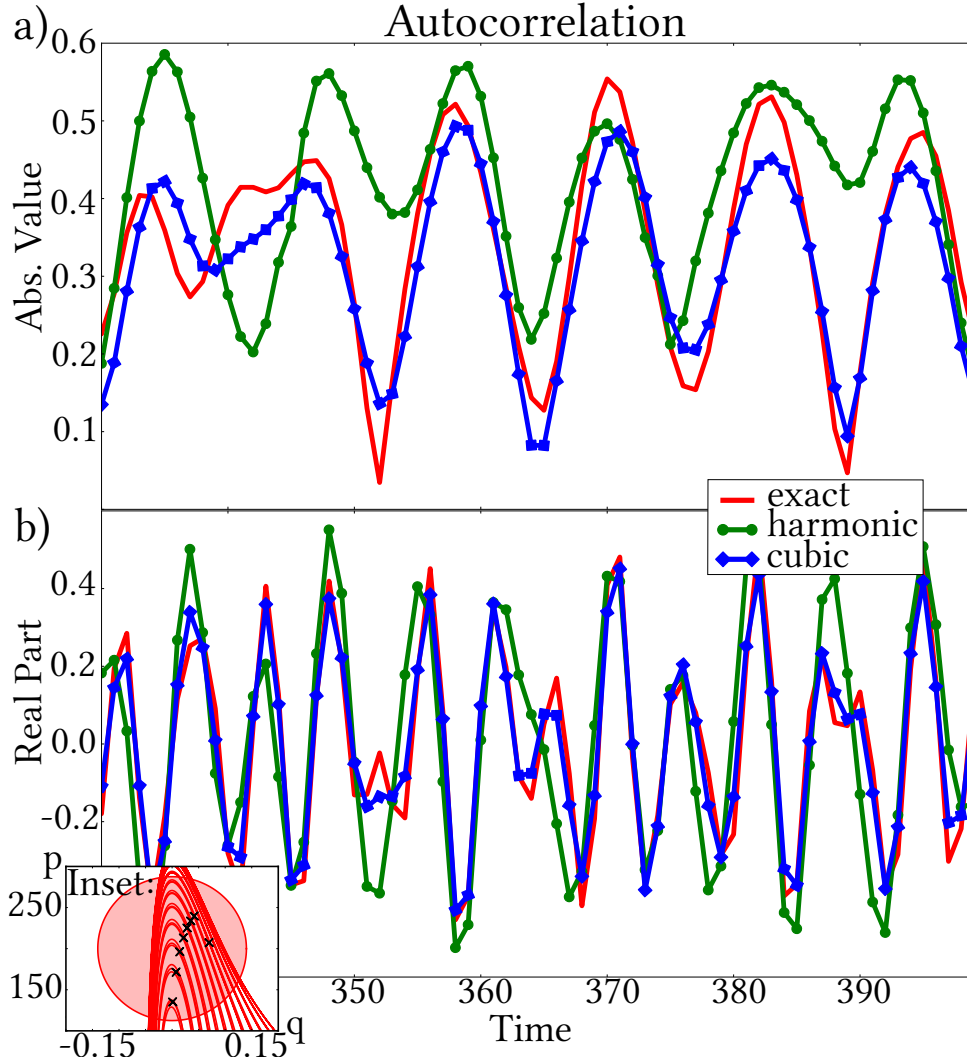
Figure 6.4: The a) absolute value and b) real part of the autocorrelation of an initial coherent state with $\sigma = 0.04$, $q_\beta = 0$, $p_\beta = 200$ in the Morse potential $H = \frac{p^2}{2m} + D[1 - \exp(-\alpha q)]^2$ with $m = 1$, $D = 50000$, and $\alpha = 8$ plotted for time step $\Delta t = 0.00005$. The cubic expansion is able to capture the local non-linearity in the autocorrelation. (Inset: The collection of periodic orbits shown in phase space which additively contribute to the semiclassical wavepacket (the sums over paths in Eqs. 6.31 and 6.32) at $t = 750$).

6.7 Conclusion

In conclusion, in this paper we presented and examined a closed-form extension to the quadratically expanded real-trajectory time-dependent W.K.B. formalism. We accomplished this by expanding the action $S(q, q', t)$ to third order so as to treat curvature in the underlying semiclassical dynamics in phase space. The resultant expression was found to perform better than the quadratic approximation when $\hbar$ is finite but not so large so as to necessitate higher powers of the action to characterize the curvature in areas of its magnitude. In practice, very short time dynamics were found to be numerically difficult to evaluate because then the triple action derivatives are too small compared to the double derivatives, rendering the argument to the Airy function to be numerically too large to handle. The expression was also found to diverge at caustics, unlike the the lower order treatment, and also to be comparatively more sensitive to the selection of an appropriate guiding trajectory (p_t, q_t) at these times when the quadratic approximation captures the dynamics well. However, when the quadratic treatment begins to fail to be sufficient at capturing the dynamics well, the cubic approximation is found to be less sensitive to the correct (p_t, q_t).

Thus, overall, unlike the lower order approximation, the cubic approximation proves to effectively handle non-linearities in phase space and it is able to accomplish this without appealing to complex classical trajectory root-finding or initial-value sampling of trajectories as prior methods have done. The derivation presented can be easily extended to higher dimensions, and we hope that it can be used as easily as the "thawed Gaussian" approximation in many-dimensional systems. Finally, the cubic treatment we presented further solidifies the concept that underlying classical trajectories make up localized quantum wavepackets, even in the non-linear regime, which is ubiquitous in physical systems far from the classical regime.

6.8 Appendix

In Eq. 6.32, the coefficients are:

$$\alpha = -\left(2\frac{\partial^3 S}{\partial q_0^3}\right)^{-\frac{2}{3}}\left[\left(\frac{\partial^3 S}{\partial q_0^2 \partial q_t}\right)^2 - \frac{\partial^3 S}{\partial q_0^3}\frac{\partial^3 S}{\partial q_0 \partial q_t^2}\right], \tag{6.50}$$

$$\beta = 2\left(2\frac{\partial^3 S}{\partial q_0^3}\right)^{-\frac{2}{3}}\left[\frac{\partial^2 S}{\partial q_0 \partial q_t}\frac{\partial^3 S}{\partial q_0^3} + \left(\frac{\partial^2 S}{\partial q_0^2} - 2A\right)\frac{\partial^3 S}{\partial q_0^2 \partial q_t}\right], \tag{6.51}$$

$$\gamma = \left(2\frac{\partial^3 S}{\partial q_0^3}\right)^{-\frac{2}{3}}\left[-4A^2 - \left(\frac{\partial^2 S}{\partial q_0^2}\right)^2 + 2\frac{\partial^3 S}{\partial q_0^3}\left(\frac{\partial S}{\partial q_0} + \xi + 2A(q_0 - q_\beta)\right)\right.$$
$$\left. -4A\frac{\partial^2 S}{\partial q_0^2}\right], \tag{6.52}$$

$$\delta = \frac{1}{6}\left(\frac{\partial^3 S}{\partial q_0^3}\right)^{-2}\left[2\left(\frac{\partial^3 S}{\partial q_0^2 \partial q_t}\right)^3 - 6\frac{\partial^3 S}{\partial q_0^2 \partial q_t}\frac{\partial^3 S}{\partial q_0^3}\frac{\partial^3 S}{\partial q_0 \partial q_t^2} + \left(\frac{\partial^3 S}{\partial q_0^3}\right)^2\frac{\partial^3 S}{\partial q_t^3}\right], \tag{6.53}$$

$$\epsilon = \frac{1}{2}\left(\frac{\partial^3 S}{\partial q_0^3}\right)^{-2}\left[4A\left(\frac{\partial^3 S}{\partial q_0^2 \partial q_t}\right)^2 + 2\frac{\partial^2 S}{\partial q_0^2}\left(\frac{\partial^3 S}{\partial q_0^2 \partial q_t}\right)^2\right. \tag{6.54}$$

$$-2\frac{\partial^2 S}{\partial q_0 \partial q_t}\frac{\partial^3 S}{\partial q_0^2 \partial q_t}\frac{\partial^3 S}{\partial q_0^3} + \frac{\partial^2 S}{\partial q_t^2}\left(\frac{\partial^3 S}{\partial q_0^3}\right)^2 \tag{6.55}$$

$$\left. -2\left(2A + \frac{\partial^2 S}{\partial q_0^2}\right)\frac{\partial^3 S}{\partial q_0^3}\frac{\partial^3 S}{\partial q_0 \partial q_t^2}\right],$$

$$\zeta = \left(\frac{\partial^3 S}{\partial q_0^3}\right)^{-2}\left[4A^2\frac{\partial^3 S}{\partial q_0^2 \partial q_t} + \left(\frac{\partial^2 S}{\partial q_0^2}\right)^2\frac{\partial^3 S}{\partial q_0^2 \partial q_t} - \frac{\partial^2 S}{\partial q_0^2}\frac{\partial^2 S}{\partial q_0 \partial q_t}\frac{\partial^3 S}{\partial q_0^3}\right.$$

$$+\frac{\partial^3 S}{\partial q_0^3}\left(\frac{\partial^3 S}{\partial q_0^3}\frac{\partial S}{\partial q_t} - \frac{\partial^3 S}{\partial q_0^2 \partial q_t}\left(\frac{\partial S}{\partial q_0} + \xi\right)\right) \tag{6.56}$$

$$\left.+2A\left(2\frac{\partial^2 S}{\partial q_0^2}\frac{\partial^3 S}{\partial q_0^2 \partial q_t} - \frac{\partial^3 S}{\partial q_0^3}\left(\frac{\partial^2 S}{\partial q_0 \partial q_t} + \frac{\partial^3 S}{\partial q_0^2 \partial q_t}(q_0 - q_\beta)\right)\right)\right],$$

$$\eta = \frac{1}{3}\left(\frac{\partial^3 S}{\partial q_0^3}\right)^{-2}\left[8A^3 + \left(\frac{\partial^2 S}{\partial q_0^2}\right)^3 + 12A^2\left(\frac{\partial^2 S}{\partial q_0^2} - \frac{\partial^3 S}{\partial q_0^3}(q_0 - q_\beta)\right)\right.$$

$$+3A\left(\left(\frac{\partial^2 S}{\partial q_0^2}\right)^2 - 2\frac{\partial^2 S}{\partial q_0^2}\frac{\partial^3 S}{\partial q_0^3}(q_0 - q_\beta) + \right. \tag{6.57}$$

$$\left.\frac{\partial^3 S}{\partial q_0^3}\left(-2\frac{\partial S}{\partial q_0} + \frac{\partial^3 S}{\partial q_0^3}(q_0 - q_\beta)^2 - 2\xi\right)\right)$$

$$\left.-3\frac{\partial^2 S}{\partial q_0^2}\frac{\partial^3 S}{\partial q_0^3}\left(\frac{\partial S}{\partial q_0} + \xi\right) + 3\left(\frac{\partial^3 S}{\partial q_0^3}\right)^2(S(q_t, q_0) + \gamma + \xi(q_0 - q_\beta))\right].$$

6.8.1 Crosscorrelation

A simple closed-form solution for the crosscorrelation treated to third-order does not seem possible. The integrals involved are in the family of those familiar to the field of "catastrophe theory". They do not appear to be well-described by numerical libraries like the Airy function is. Therefore, though an analytic solution may be possible to derive, it's practical implementation would be difficult on a computer today.

7
Directed Herman Kluk

A simplification of the Heller-Herman-Kluk-Kay (HK) propagator is presented that does not suffer from the need for an increasing number of trajectories with dimensions of the system under study. This is accomplished by replacing HK's uniformizing integral over all of phase space by a one-dimensional curve that is appropriately selected to lie along the fastest growing manifold of a defining trajectory. It is shown that this modification leads to eigenspectra of quantum states in weakly anharmonic systems that can outperform the comparatively computationally cheap thawed Gaussian approximation method and frequently approach the accuracy of spectra obtained with the full HK propagator.

7.0.1 Introduction

Semiclassical quantum wave packet evolution is a powerful method to evolve quantum states using classical trajectories. Many efficient methods exist.

Perhaps the most widely used semiclassical method of quantum propagation is the Heller-Herman-Kluk-Kay (HK) propagator[35, 26, 7, 36, 37]. In brief, this method is a stationary phase approximation of the quantum coherent state propagator evaluated in an uniformized initial value representation. When applied to finding autocorrelations and from the perspective of phase space, every timestep requires the calculation of the overlap of a swarm of "frozen" Gaussians, often selected by Monte Carlo-based sampling dependent on the initial state. The propagation of every such Gaussian is governed by its central classical trajectory and each Gaussian's contribution to the propagator's value at a timestep is dependent on the classical action of its central trajectory

as well as elements of its stability matrix. In practice, computation of these elements, first order differentials of final position and momenta with respect to initial position and momenta, is the most intensive part of the procedure.

Unfortunately, HK suffers from the necessity of calculating an increasing number of trajectories as the number of degrees of freedom increases. The calculation of every trajectory's associated stability matrix elements is doubly confounded; Not only do the number of matrix elements scale unfavorably with degrees of freedom ($4d^2$ for d degrees of freedom), the number of times these elements must be calculated also proliferates (frequently exponentially) with the number of trajectories. Efforts have been made to address this issue, the most notable of which is cellular dephasing[11] or Filinov filtering[38]. However, these methods have proven ineffective in many systems and only reduce the growth of trajectories necessary to a point[39].

One way around this unfavorable growth in the number of trajectories is to take a more targeted approach in selecting only the most important trajectories. In the first half of this chapter, a simplification to the HK formulation is heuristically presented referred to as "directed" HK (DHK) and is numerically compared to the full HK method. In the second half, DHK is examined in a more formal perspective.

DHK is simpler than HK in that it performs the uniformizing integration of the latter along a one-dimensional manifold instead of all of phase space, regardless of the dimension of the system under study. This curve is chosen to lie along the eigenvector with the largest eigenvalue of the stability matrix associated with a defining trajectory. In a test set of chemically relevant anharmonic systems, it is shown that this approach eliminates the scaling in the number of trajectories with dimension and produces results that are frequently more accurate than the computationally cheaper method of the thawed Gaussian approximation (TGA)[3].

7.0.2 Method

The uniformization present in the HK propagator involves an integration over all the degrees of phase space where the quantum state of interest resides (see Figure 7.1a). In the case that

61

a dominant eigenvector of the stability matrix governing the dynamics of the state exists, such isotropic sampling is redundant from the perspective that all the trajectories tend towards this one-dimensional manifold. Sampling solely along this manifold reduces the integration over initial states dramatically while still accomplishing a good sampling of the time-evolved state (Figure 7.1c).
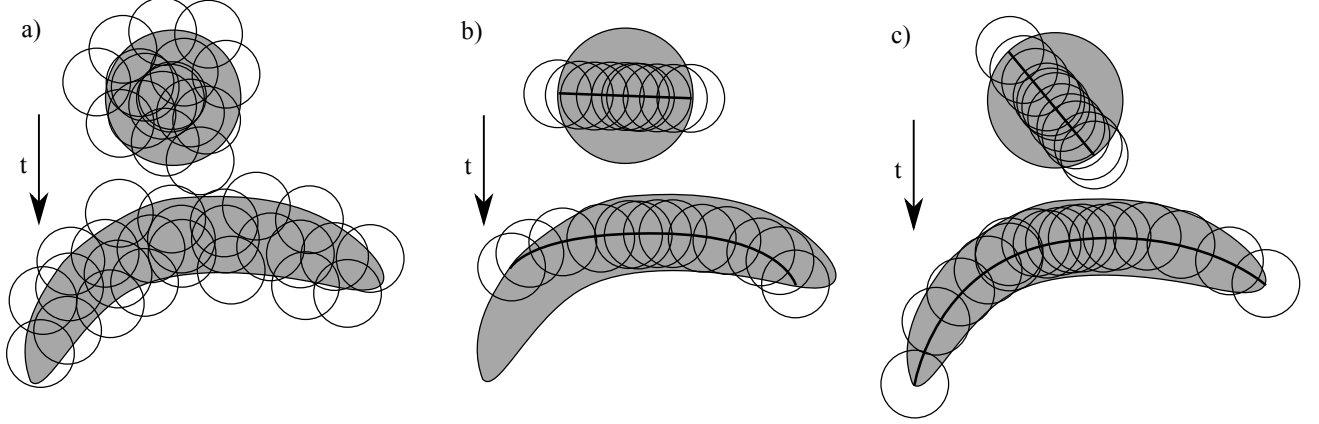

Figure 7.1: Cartoon of the effect of the uniformization integral in HK as it appears in phase space. a) Sampling the initial state based on its absolute density in all dimensions, as frequently performed with the Metropolis-Hastings algorithm for integration. Though initially isotropic, such a distribution of "frozen" Gaussians propagates to become a distribution that stretches out along a dominant stability matrix eigenvector. b) Replacing this isotropic distribution which is slow to converge with one along an ill-chosen one-dimensional manifold will lead to a poor representation of later distributions. c) However, if the proper axis is used, a similar distribution to the one obtained with the full HK propagater can be formed (especially at later times) without initially sampling the full dimensional space since all trajectories tend to that dominant manifold.

As an exposition of the accuracy and efficiency of such one-dimensional sampling, we calculate the autocorrelation of a coherent state Ψ_β centered at $(\boldsymbol{p}_\beta, \boldsymbol{q}_\beta)$ with width γ_β in position space. The DHK method is based on the full HK propagator and is presented below:

$$\langle \Psi_\beta(0) \mid \Psi_\beta(t) \rangle_{\text{DHK}}$$
$$= \mathcal{N}^{-1} \int_{\mathcal{L}} dl \mathcal{A}(l,t) g(l,0) g^*(l,t) e^{\frac{i}{\hbar} S(\boldsymbol{p}_0(l), \boldsymbol{q}_0(l), t)} \tag{7.1}$$

where

$$g(l,0) = \exp\left[-\frac{1}{2} \frac{\gamma\gamma_\beta}{\gamma+\gamma_\beta} (\boldsymbol{q}_\beta - \boldsymbol{q}_0(l))^2 - \frac{1}{2\hbar^2(\gamma+\gamma_\beta)} (\boldsymbol{p}_\beta - \boldsymbol{p}_0(l))^2 + \frac{i}{\hbar(\gamma+\gamma_\beta)} (\boldsymbol{q}_0(l) - \boldsymbol{q}_\beta)(\gamma \boldsymbol{p}_\beta + \gamma_\beta \boldsymbol{p}_0(l)) \right], \tag{7.2}$$

$$g(l,t) = \exp\left[-\frac{1}{2}\frac{\gamma\gamma_\beta}{\gamma+\gamma_\beta}(\boldsymbol{q}_\beta - \boldsymbol{q}_t(l))^2 - \frac{1}{2\hbar^2(\gamma+\gamma_\beta)}(\boldsymbol{p}_\beta - \boldsymbol{p}_t(l))^2 + \frac{i}{\hbar(\gamma+\gamma_\beta)}(\boldsymbol{q}_t(l) - \boldsymbol{q}_\beta)(\gamma\boldsymbol{p}_\beta + \gamma_\beta\boldsymbol{p}_t(l))\right], \quad (7.3)$$

$$\mathcal{A}(l,t) = \sqrt{\det\left[\frac{1}{2}\left(\frac{\partial\boldsymbol{p}_t(l)}{\partial\boldsymbol{p}_0(l)} + \frac{\partial\boldsymbol{q}_t(l)}{\partial\boldsymbol{q}_0(l)} - i\gamma\hbar\frac{\partial\boldsymbol{q}_t(l)}{\partial\boldsymbol{p}_0(l)} + \frac{i}{\hbar\gamma}\frac{\partial\boldsymbol{p}_t(l)}{\partial\boldsymbol{q}_0(l)}\right)\right]}, \quad (7.4)$$

and

$$\mathcal{N} = \int dl\, g(l,0)g^*(l,0). \quad (7.5)$$

The differences between this simpler relation and the full HK propagator are the contour integral over the curve $\mathcal{L}$ and the addition of the global normalization $\mathcal{N}$ so that the expression is 1 at $t = 0$.

No effort is made to formally justify these simplifications aside from pointing out the following observations. Grossman *et al.* have shown that the uniformization integral in HK can be formulated as the result of inserting a coherent state identity operator into a primitive semiclassical propagator to be evaluated fully[40] (as opposed to by stationary phase). Herein this identity operator is the one-dimensional manifold of coherent states which is not a complete basis set (in any dimension except with proper modification in one dimension) and so, at the very least, requires an overall normalization with $\mathcal{N}$. The amplitudes and phases from the coherent states that are neglected by this one-dimensional manifold seem to be proportionally accounted for by the central manifold's values.

It is important to notice that when applied to dimensions greater than one, the fluctuations in the magnitude of the $\mathcal{A}(l,t)$ can cause the magnitude of DHK's autocorrelation to exceed 1, especially for ill-chosen manifolds $\mathcal{L}$. In practice this was found to be uncommon in the systems studied here though a ceiling of 1 was forced in all numerical simulations.

7.0.3 Numerical Examples

A series of test runs were conducted on progressively larger molecular systems obeying the coupled Morse vibrational Hamiltonian:

$$H = \sum_{i=1}^{N} \left\{ \frac{1}{2\mu} p_i^2 + D[1 - \exp(-\alpha q_i)]^2 \right\} \qquad (7.6)$$
$$+ g_{qq'} \sum_{i<j}^{N} p_i p_j + f_{qq'} \sum_{i<j}^{N} q_i q_j$$

Numerical tests were performed for a parametrization of HCl ($N = 1$)[41, 42], SO_2 ($N = 2$)[43], GeH_4 ($N = 4$)[44] and $^{184}WF_6$ ($N = 6$)[45]. Initial states were chosen to be displaced coherent states in one vibrational degree of freedom and ground states in all the others. DHK's one-dimensional manifold $\mathcal{L}$ was chosen to lie along the dominant stability matrix eigenvector for the coherent state's central trajectory during either its first or second quasi-periodic return to the region near its initial state. For a list of parameters used see the Appendix.
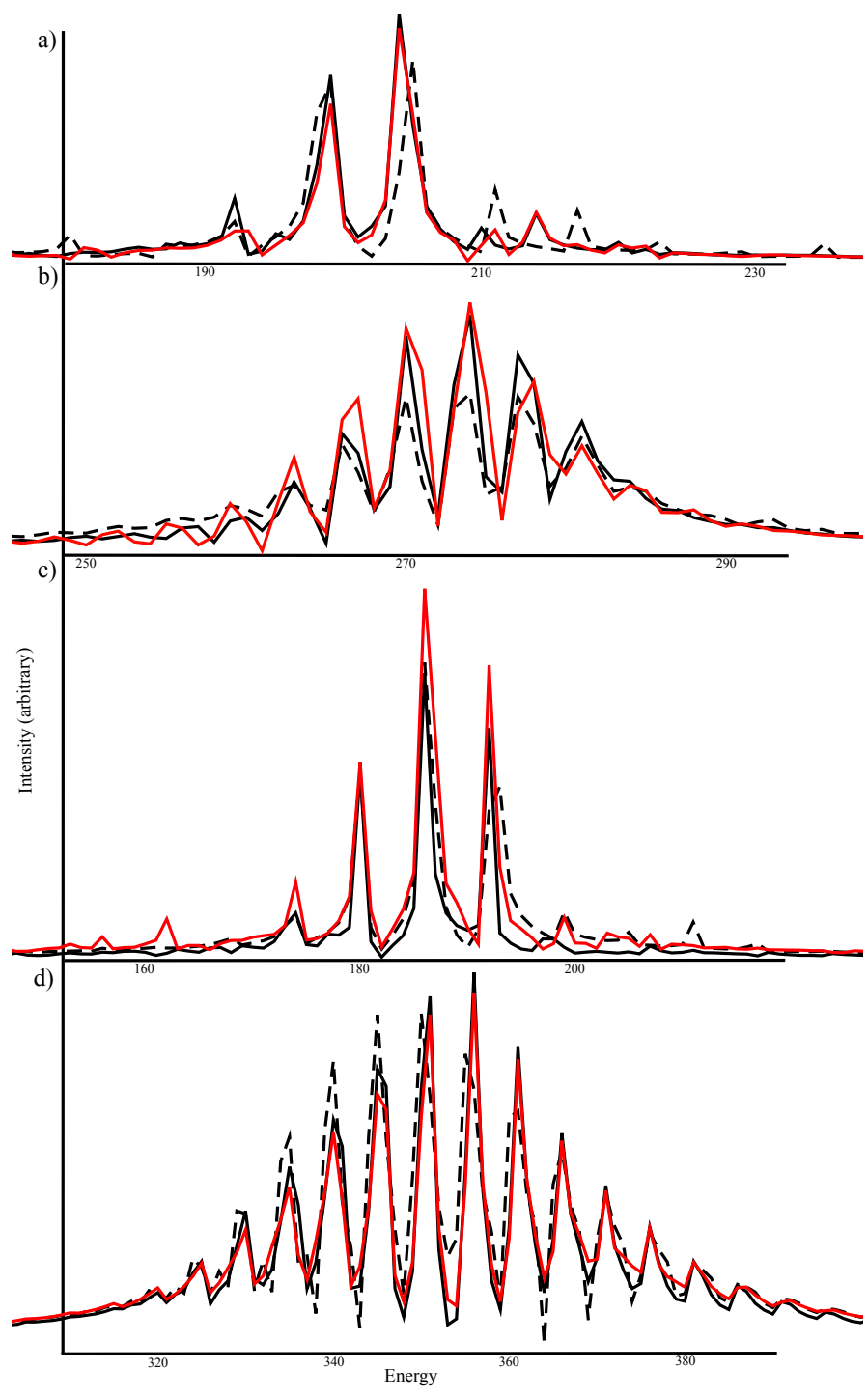
Figure 7.2: HK (black), TGA (dashed black) and DHK (red) results are presented for a) HCl, b) SO_2, c) GeH_4 and d) $^{184}WF_6$. Energy units are 5 THz.

Figure 7.2 shows the eigenspectra of these states - the Fourier transforms of their autocorrelations. Comparison with TGA confirms that they quickly explore anharmonic regions of phase space and limit its accuracy. In contrast, the DHK method along the one dimensional manifold is able to maintain very good accuracy with the eigenspectra of the full HK method. Furthermore, it is able to accomplish this without the full HK method's unfortunate scaling with dimension (see figure 7.3). Tests with initial states involving more than a single excited degree of freedom produced similar agreement. If the excited states were brought down lower on the Morse potential, agreement with TGA improved, as expected for such a method that is exact for harmonic potentials.
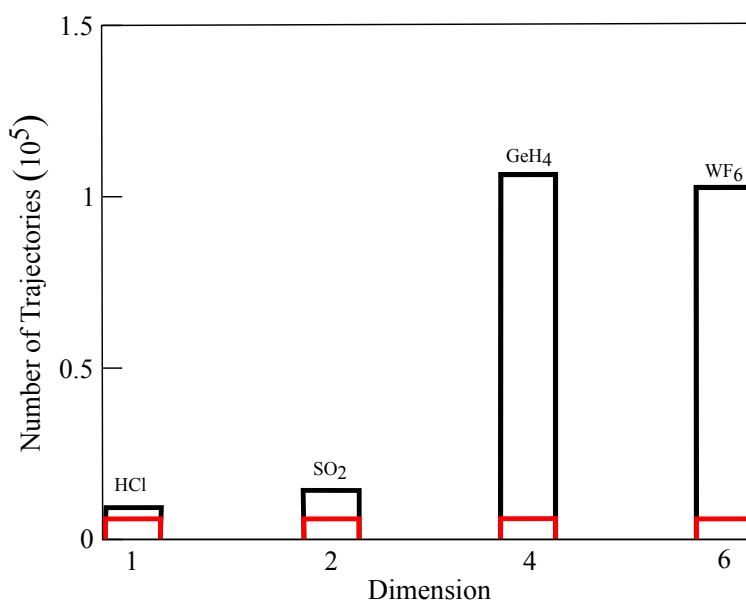

Figure 7.3: Number of trajectories necessary for convergence of HK (black) and DHK (red) spectra in Figure 7.2 with respect to the dimension of the system.

It should be noted that all the trial runs reported here involved strong recurrences in the autocorrelations of the respective systems. In some cases where recurrences were observed to be far smaller, the sensitivity to the selection of the initial manifold seemed to increase (not shown). Indeed, it was found that separate recurrences often required different one-dimensional manifolds to be well brought out in this simplification to HK. This is expected considering that their separate dynamical origins are made more apparent when they only produce "glancing" blows with the initial state, leading to weak recurrences.

7.0.4 Conclusion

It is perhaps fulfilling to discover that when the underlying classical dynamics of a state in an anharmonic system exhibit a dominant stability matrix eigenvector, the proliferation of trajectories necessary to compute a semiclassical autocorrelation can be severely reduced. It remains to be seen whether this method can be formalized or if it can be generalized to any submanifold of smaller dimension. The latter is especially important in systems which exhibit more than one dominant eigenvector.

Finally, it is also necessary to examine the robustness of this simplification with regards to weaker autocorrelations and in cases of more anharmonic, mixed or chaotic dynamics. Future directions also include examining the marriage of this method with Filinov filtering and its usefulness in on-the-fly calculation.

Though many possibilities for speeding up semiclassical evaluation have been examined over the years, few have focused on using the actual dynamics of underlying trajectories to simplify computation with "frozen" Gaussian basis sets. Our findings offer encouraging evidence about the promise of this direction.

7.1 A More Formal Analysis

We now proceed through a more formal justification for the successes of the DHK time propagator by examining its performance in one-dimensional bound systems which exhibit at least quasi-periodic motion. DHK is distinguished by its single one-dimensional integral - a vast simplification over the usual $2N$-dimensional integral in full HK (for an N-dimensional system). We find that DHK accurately captures particular coherent state autocorrelations when its single integral is chosen to lie along these states' fastest growing manifold, as long as it is not perpendicular to their action gradient. Moreover, the larger the action gradient, the better DHK will perform. We numerically examine DHK's accuracy in a one-dimensional quartic oscillator and illustrate that these conditions are frequently satisfied such that the method performs well. This lends some explanation for why DHK frequently seems to work so well, and suggests that it may be applicable to systems exhibiting quite strong anharmonicity.

7.1.1 Motivation

In hyperbolic systems there exist stable and unstable manifolds which characterize all trajectories. Those on the unstable manifold will exponentially depart from a fixed point while trajectories on the stable manifold will exponentially approach a fixed point. Though most bound systems cannot be characterized in this way, they frequently still exhibit at least quasi-periodic points around which growing and compressing manifolds can be found (as long as the potential has some anharmonicity). An example is shown in the inset of Figure 7.4 where the phase space of a quartic oscillator is shown and the trajectories making up the density of an initial coherent state stretch out along the manifold delineated by the green curve after it has undergone one period.

Again, we consider the dynamics of quantum states that are initially coherent states. The diagonal term for the HK propagator in a coherent state representation (equivalently the
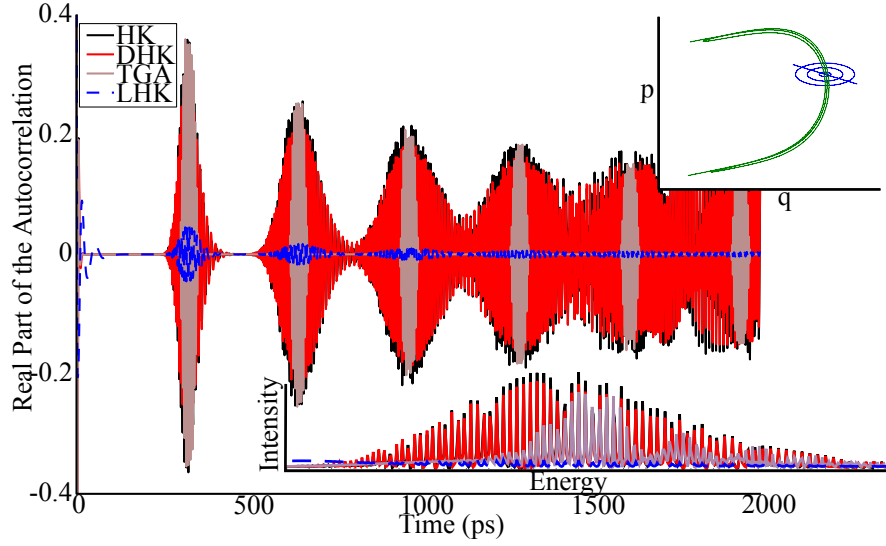
Figure 7.4: The real part of the autocorrelation compared between HK, DHK, TGA and LHK. TGA is the thawed Gaussian approximation[3]. Inset, top-right: The phase space overlap between the initial (blue) and time evolved (green) coherent state. The blue line corresponds to the manifold over which DHK's integral was evaluated. Inset, bottom-right: The Fourier transform of the autocorrelation.

autocorrelation of a coherent state) is:

$$
\begin{aligned}
&\langle \Psi_\beta(0) | \Psi_\beta(t) \rangle_{\mathrm{HK}} \\
&= \left(\frac{\sqrt{\gamma \gamma_\beta}}{\pi \hbar (\gamma + \gamma_\beta)} \right)^N \int \mathrm{d}\boldsymbol{p}_0 \int \mathrm{d}\boldsymbol{q}_0 \, C_t(\boldsymbol{p}_0, \boldsymbol{q}_0) \exp\left[\frac{i}{\hbar} S_t(\boldsymbol{p}_0, \boldsymbol{q}_0) \right] g_\beta(\boldsymbol{p}_0, \boldsymbol{q}_0) g_\beta^*(\boldsymbol{p}_t, \boldsymbol{q}_t),
\end{aligned}
\tag{7.7}
$$

where

$$
g_\beta(\boldsymbol{p}, \boldsymbol{q}) = \exp\left[-\frac{\gamma_\beta \gamma}{2(\gamma + \gamma_\beta)} (\boldsymbol{q} - \boldsymbol{q}_\beta)^2 - \frac{1}{2\hbar^2(\gamma + \gamma_\beta)} (\boldsymbol{p} - \boldsymbol{p}_\beta)^2 + \frac{i}{\hbar(\gamma + \gamma_\beta)} (\boldsymbol{q} - \boldsymbol{q}_\beta) \cdot (\gamma \boldsymbol{p}_\beta + \gamma_\beta \boldsymbol{p}) \right],
\tag{7.8}
$$

and the preexponential is

$$
C_t(\boldsymbol{p}_0, \boldsymbol{q}_0) = \sqrt{\det\left[\frac{1}{2} \left(\frac{\partial \boldsymbol{p}_t}{\partial \boldsymbol{p}_0} + \frac{\partial \boldsymbol{q}_t}{\partial \boldsymbol{q}_0} - i\hbar\gamma \frac{\partial \boldsymbol{q}_t}{\partial \boldsymbol{p}_0} + \frac{i}{\hbar\gamma} \frac{\partial \boldsymbol{p}_t}{\partial \boldsymbol{q}_0} \right) \right]}.
\tag{7.9}
$$

This term contains elements of the stability matrix

$$
\boldsymbol{M}(t) = \begin{pmatrix} \boldsymbol{M}(t)_{11} & \boldsymbol{M}(t)_{12} \\ \boldsymbol{M}(t)_{21} & \boldsymbol{M}(t)_{22} \end{pmatrix} = \begin{pmatrix} \left(\frac{\partial \boldsymbol{p}_t}{\partial \boldsymbol{p}_0} \right)_{\boldsymbol{q}_0} & \left(\frac{\partial \boldsymbol{p}_t}{\partial \boldsymbol{q}_0} \right)_{\boldsymbol{p}_0} \\ \left(\frac{\partial \boldsymbol{q}_t}{\partial \boldsymbol{p}_0} \right)_{\boldsymbol{q}_0} & \left(\frac{\partial \boldsymbol{q}_t}{\partial \boldsymbol{q}_0} \right)_{\boldsymbol{p}_0} \end{pmatrix}.
\tag{7.10}
$$

Vectors are denoted by lowercase bold letters while matrices are denoted by uppercase bold letters (e.g. $\boldsymbol{a}$ and $\boldsymbol{A}$ respectively). The coherent state Ψ_β has dispersion γ_β whereas γ are those of the "frozen" coherent states centered at $(\boldsymbol{p}_0, \boldsymbol{q}_0)$ whose overlaps with $\Psi_\beta(0)$ and $\Psi_\beta(t)$, $g_\beta(\boldsymbol{p}_0, \boldsymbol{q}_0) g_\beta^*(\boldsymbol{p}_t, \boldsymbol{q}_t)$, are integrated over. Each frozen state is governed by its central classical trajectory with associated actions S_t and stability matrices $\boldsymbol{M}(t)$ that are both accounted for through the phase and preexponential terms respectively.

As can be seen in Eqs. 8.8 to 7.9, HK has several ingredients: a) the actual overlap between the initial and propagated coherent states as sampled by "frozen" coherent states, b) the phase due to their action, and the c) phase and d) magnitude of their preexponential involving stability matrix elements. Figure 7.5 shows how all of these vary along the green manifold in a quartic oscillator system for states labeled A, B, C and D. Forecasting the effectiveness of DHK, it can be seen that this manifold cuts through and samples a good average of all the ingredients in the area of highest overlap for every state except C. Furthermore, the phase space densities of the states asymptotically approach the manifold with time. In this way, it can be seen that integrating along it may proportionally represent all adjacent phase space points appropriately and so render their explicit inclusion through a larger dimensional integral such as HK's unnecessary. DHK exploits this idea, and as the right column of Figure 7.5 (as well as Figure 7.4) shows, its autocorrelations can be in very good agreement with HK's.

7.1.2   Formulation of DHK

As shown previously, DHK replaces HK's full $2N$-dimensional integral with one along a selected one-dimensional manifold $\mathcal{L}$, which can differ from any of the $2N$ integral domains of the full HK expression:

$$\langle \Psi_\beta(0) | \Psi_\beta(t) \rangle_{\text{HK}} = \int_{-\infty}^{\infty} \mathrm{d}^{2N} \boldsymbol{x}_0 \xi(\boldsymbol{x}_0, t) \approx \mathcal{N}^{-1} \int_{\mathcal{L}} \mathrm{d}l \xi(\boldsymbol{x}_0(l), t) \equiv \langle \Psi_\beta(0) | \Psi_\beta(t) \rangle_{\text{DHK}} \quad (7.11)$$

where ξ is the integrand in the full HK formula. Naturally, we desire such a method to still be normalized such that it is 1 at $t = 0$. This means that

$$\mathcal{N} = \int_{\mathcal{L}} \mathrm{d}l \xi(\boldsymbol{x}_0(l), 0). \tag{7.12}$$

It is therefore necessary in any application of Eq. 7.11 to show that there exists such a manifold $\mathcal{L}$, which is a good representation of the full HK integral's domain. To accomplish this it is important to examine the "ingredients" of HK's integrand ξ where it is most significant, namely, for the autocorrelation examined here, in the phase space region of the initial coherent state.
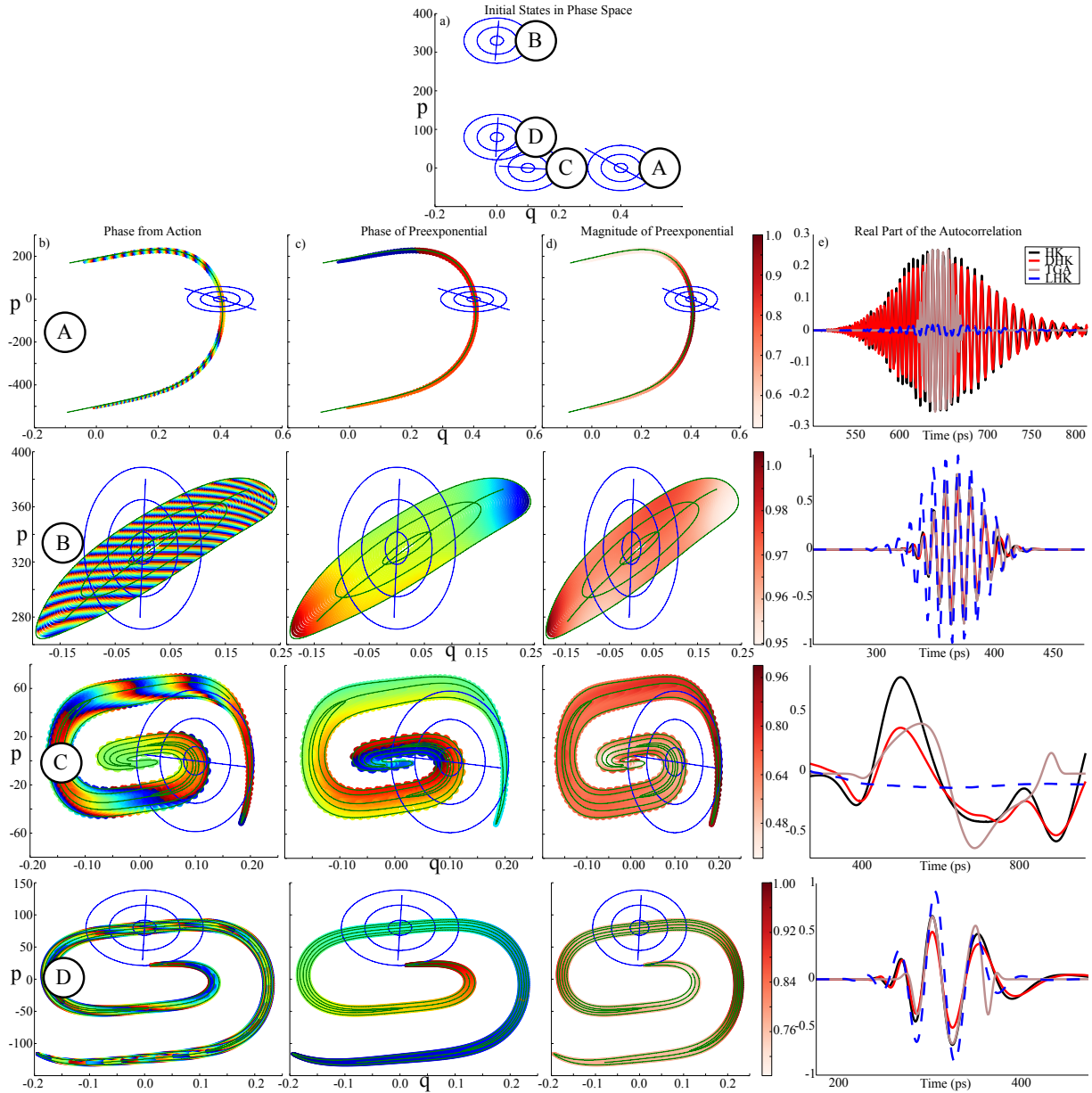
Figure 7.5: a) The initial phase space distributions of the four coherent states A-D in the quartic oscillator system investigated are shown. Organized column-wise are plots of each state's b) phase due to its action, and c) phase and d) magnitude of its HK preexponential immediately after one orbit. Also shown are the corresponding e) first recurrences of their autocorrelations. The blue line corresponds to the manifold over which DHK's integral was evaluated which evolves into the green line after one orbit. Integrating along this manifold is intended to proportionally represent the rest of the overlap phase space. Shown superimposed on the plots in a)-d) are corresponding concentric initial (blue) and final (green) confidence intervals of the underlying wavefunction density.

72

A cursory examination of recurrences in phase space (such as in Figure 7.5) reveals that the phase due to the evolved state's action is often the most significantly varying component of ξ on the scale of the area of overlap with the initial state when compared with the magnitude and phase of the associated preexponential. This is reasonable since the preexponential is a function of the stability matrices of the underlying trajectories and is responsible for preserving HK's norm; it will only vary between areas in phase space that are experiencing different environments of compression and stretching and this generally occurs at scales that are larger than that of the area of the initial coherent state. The phase change from the action along a manifold with endpoints l_1 and l_2,

$$S(\boldsymbol{p}_0(l_2), \boldsymbol{q}_0(l_2), t) - S(\boldsymbol{p}_0(l_1), \boldsymbol{q}_0(l_1), t) = \int_{q_t(l_1)}^{q_t(l_2)} \boldsymbol{p} \cdot \mathrm{d}\boldsymbol{q}, \tag{7.13}$$

can vary far more quickly.

Therefore, when examining the largest contributions to the characteristics of ξ, it is often sufficient to only consider the density of the overlap and the phase from the action at the point of largest overlap. In particular, we proceed to approximate the overlap of the time propagated coherent state $\Psi_\beta(t)$ with its initial self $\Psi_\beta(0)$, by representing both by Gaussians $\Psi_\beta(q,t) \approx \left(\frac{\Re \gamma_t}{\pi}\right)^{\frac{1}{4}} \exp\left[-\frac{\gamma_t}{2}(q - q_\beta^2) + \frac{i}{\hbar}p_\beta(q - q_\beta)\right]$ (though the propagated state will no longer be a Gaussian in anharmonic systems) and consider their respective Wigner functions:

$$\rho_W(p,q,\theta,\gamma) = \frac{1}{\pi\hbar} \exp\left\{ [(p - p_\beta, q - q_\beta) \cdot R(\theta)] \begin{pmatrix} -\frac{1}{\gamma\hbar^2} & 0 \\ 0 & -\gamma \end{pmatrix} [(p - p_\beta, q - q_\beta) \cdot R(\theta)]^T \right\}, \tag{7.14}$$

where θ denotes their rotation with respect to the origin, γ are their dispersions along their major and minor axes ($\gamma = \frac{\sin\theta + i\gamma_t\hbar\cos\theta}{\gamma_t\hbar^2\sin\theta + i\hbar\cos\theta} \in \mathbb{R}$, not to be confused with the γ of HK's frozen sampling Gaussians, g_β, discussed in the Motivation) and $R(\theta)$ is the standard 2×2 rotation matrix. See the Appendix for a derivation. These Gaussian fits of $\Psi_\beta(t)$ are equivalent to its propagation under a harmonic expansion of the potential at its center in phase space (such as in the thawed Gaussian approximation[3]). We further approximate the contribution of the phase from the action via a plane wave

$$\exp\left[ik(\cos(\phi)\hat{p} - \sin(\phi)\hat{q}) \cdot (p, q)^T/\hbar\right], \tag{7.15}$$

which is rotated by ϕ with respect to the $\hat{p}$ axis and has momentum k. The top-right of Figure 7.6 illustrates how these approximate the overlap and phase of a particular recurrence.

Under these approximations, the full HK autocorrelation at a point in time during a recurrence corresponds to taking the full integral of the two ρ_Ws, with one rotated by θ compared to the other, all modulated by the plane wave:

$$O_{\text{HK}}(t) \approx \int_{-\infty}^{\infty} \mathrm{d}p \int_{-\infty}^{\infty} \mathrm{d}q \rho_W(p, q; 0, \gamma_0) \rho_W(p, q; \theta, \gamma) \exp\left[ik(\cos(\phi)\hat{p} - \sin(\phi)\hat{q}) \cdot (p, q)^T/\hbar\right].$$
(7.16)

We let the fastest growing manifold lie along the p-coordinate cutting through the center of the coherent state so that its stretching in this direction is proportional to γ. It follows that $\theta \approx 0$ in the limit that the dynamics are wholly linearizable. Therefore, if we set DHK's $\mathcal{L}$ manifold to lie along the state's fastest growing manifold - which seems sensible since such an $\mathcal{L}$ will contribute non-zero overlaps for the appropriate times as the state passes through a recurrence - DHK will correspond to a simplified version of Eq. 7.16:

$$O_{\text{DHK}}(t) \approx \frac{\int_{-\infty}^{\infty} \mathrm{d}l \rho_W(l, 0; 0, \gamma_0) \rho_W(l, 0; 0, \gamma) \exp\left[ik(\cos(\phi)\hat{p} - \sin(\phi)\hat{q}) \cdot (p, q)^T/\hbar\right]}{\int_{-\infty}^{\infty} \mathrm{d}l \rho_W(l, 0; 0, \gamma_0) \rho_W(l, 0; 0, \gamma_0)}.$$
(7.17)

We are interested in the absolute value of the difference of $O_{\text{DHK}}(t)$ and O_{HK}, a measure of the expected error in DHK, where $\theta \approx 0$:

$$|O_{\text{DHK}}(t) - O_{\text{HK}}(t)| = \left| \sqrt{\frac{2\gamma}{\gamma + \gamma_0}} e^{-\frac{\gamma\gamma_0 k^2 \cos^2(\phi)}{4(\gamma + \gamma_0)}} - \frac{2\sqrt{\gamma\gamma_0}}{\gamma + \gamma_0} e^{-\frac{k^2((\gamma\gamma_0 - 1)\cos(2\phi) + \gamma\gamma_0 + 1)}{8(\gamma + \gamma_0)}} \right|.$$
(7.18)

An examination of this error shown in Figure 7.6 reveals that, under the aforementioned approximations of the modeled overlap, DHK always approaches HK's value for all k and ϕ when $\frac{\gamma}{\gamma_0} \ll 1$ where γ_0 is the dispersion of the initial coherent state and γ is its dispersion during the recurrence along the (fastest growing) manifold sampled. The greater the manifold's growth, the larger γ is. This may seem troubling, since it means that accuracy of DHK is only ensured when its one-dimensional integral is performed along the direction that has shrunk, not grown, and such

a manifold would only capture the middle of recurrences well when the center of the state has returned near its initial point. However, all is saved by non-zero phase variation from action; in particular, Figure 7.6 shows that when DHK's integral lies along the fastest growing manifold ($\gamma > \gamma_0$), its agreement with HK improves the larger the wavevector k of the plane wave is and as long as ϕ, its angle, isn't perpendicular to this manifold. This last requirement is likely due to the fact that sampling along $\mathcal{L}$ when it lies perpendicular to the gradient of action would only include one value of this variation and thus hardly serve as its representative average.
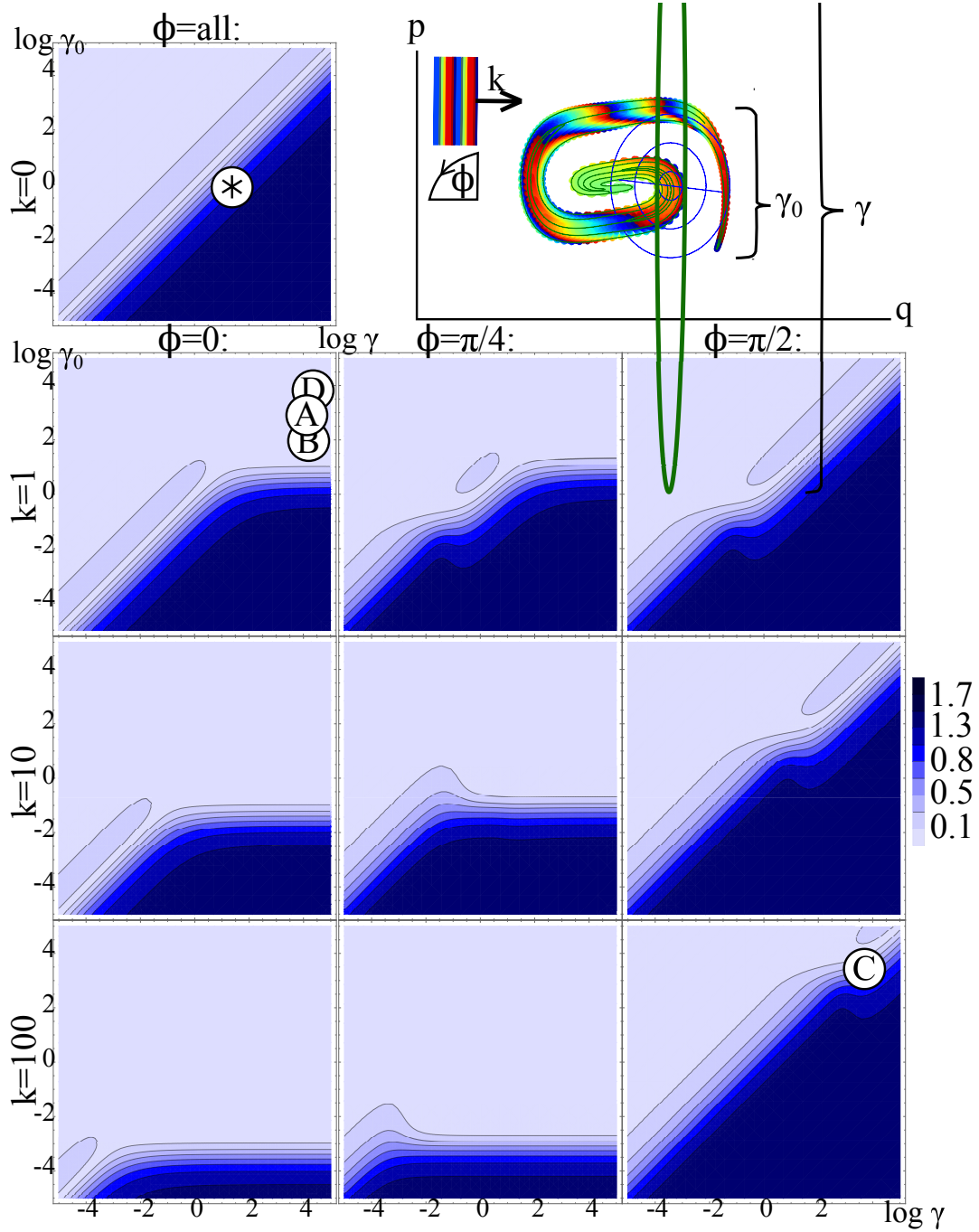
Figure 7.6: The contour plots for various values of k and ϕ of $|O_{\mathrm{DHK}}(t) - O_{\mathrm{HK}}(t)|$ defined by Eqs. 7.16 and 7.17. These indicate that when $\mathcal{L}$ lies along the fastest growing manifold, DHK fares best at reproducing autocorrelations when $\frac{\gamma}{\gamma_0} \ll 1$ but also will agree with HK better the larger k is as long as $\phi \neq \pi/2$. In other words, DHK will be more accurate the greater the gradient of the action as long as it does not face perpendicularly to $\mathcal{L}$. This means that the first recurrence of system A, B and D (shown in white markers) should be well treated by DHK. C's first recurrence should be less accurately captured. This qualitatively agrees with the results shown in Figure 7.5e. Note that representing A's phase of action by a plane wave is a rather poor approximation as can be seen in Figure 7.5, however its wavevector in the vicinity of the overlap is $k > 0$ and $\phi \approx 0$.

Substituting in the appropriate angles ϕ of the momentum k found at the moment of the first recurrence of states $A - D$ into Eqs. 7.16 and 7.17 reveals that they all satisfy this last requirement of $\phi \neq \pi/2$ and so lie in areas where DHK is close to HK's value, except for C, as indicated by the markers in Figure 7.6. For state C, the gradient of action varies perpendicular to the major axis of its initial and final states. C's initial dispersion γ_0 is too small for DHK to handle this perpendicular angle of action variation $\phi = \pi/2$. This agrees well with the relatively poorer autocorrelation calculated from DHK for system C seen in Figure 7.5e.

We have so far illustrated that it is often quite reasonable to assume, in bound anharmonic systems exhibiting at least quasi-periodicity, that recurrences which can be well described by our simple Gaussian-plane wave model, can frequently be well approximated by only the single integral in Eq. 7.11 when $\mathcal{L}$ is chosen to lie along the fastest growing manifold of the coherent state.

Linearizing around such a chosen manifold $\mathcal{L}$ (by Taylor expanding) is an approach that may appear to be closely related, at least at first glance. Its derivation is presented in the Appendix. The autocorrelations of the resultant method, which we refer to herein as "linearized HK" (LHK), are compared to DHK in Figure 7.5e and are shown to often be inferior to DHK in the quartic system examined. This can be explained by noting that DHK's manifold $\mathcal{L}$ is explicitly chosen to be representative of *all* of the features of the integrand. Linearization around the same $\mathcal{L}$ further takes into account the behavior of the integrand perpendicular and close by to this manifold, which can be quite different from the representative whole, and frequently this can lead to a worse approximation.

For completeness, we substitute in ξ and expand Eq. 7.11, revealing the full DHK formula as:

$$\langle \Psi_\beta(0) \mid \Psi_\beta(t) \rangle_{\text{DHK}}$$
$$= \mathcal{N}^{-1} \int_{\mathcal{L}} \mathrm{d}l \mathcal{A}(l,t) g_\beta(l,0) g_\beta^*(l,t) e^{\frac{i}{\hbar} S(\boldsymbol{p}_0(l), \boldsymbol{q}_0(l), t)} \tag{7.19}$$

where

$$g_\beta(l,0) = \exp\left[-\frac{1}{2}\frac{\gamma\gamma_\beta}{\gamma+\gamma_\beta}(\boldsymbol{q}_\beta - \boldsymbol{q}_0(l))^2 - \frac{1}{2\hbar^2(\gamma+\gamma_\beta)}(\boldsymbol{p}_\beta - \boldsymbol{p}_0(l))^2 + \frac{i}{\hbar(\gamma+\gamma_\beta)}(\boldsymbol{q}_0(l) - \boldsymbol{q}_\beta)(\gamma\boldsymbol{p}_\beta + \gamma_\beta\boldsymbol{p}_0(l))\right], \tag{7.20}$$

$$g_\beta(l, t) = \exp\left[-\frac{1}{2}\frac{\gamma\gamma_\beta}{\gamma + \gamma_\beta}(\boldsymbol{q}_\beta - \boldsymbol{q}_t(l))^2 - \frac{1}{2\hbar^2(\gamma + \gamma_\beta)}(\boldsymbol{p}_\beta - \boldsymbol{p}_t(l))^2 + \frac{i}{\hbar(\gamma + \gamma_\beta)}(\boldsymbol{q}_t(l) - \boldsymbol{q}_\beta)(\gamma\boldsymbol{p}_\beta + \gamma_\beta\boldsymbol{p}_t(l))\right], \quad (7.21)$$

$$\mathcal{A}(l, t) = \sqrt{\det\left[\frac{1}{2}\left(\frac{\partial\boldsymbol{p}_t(l)}{\partial\boldsymbol{p}_0(l)} + \frac{\partial\boldsymbol{q}_t(l)}{\partial\boldsymbol{q}_0(l)} - i\gamma\hbar\frac{\partial\boldsymbol{q}_t(l)}{\partial\boldsymbol{p}_0(l)} + \frac{i}{\hbar\gamma}\frac{\partial\boldsymbol{p}_t(l)}{\partial\boldsymbol{q}_0(l)}\right)\right]}, \quad (7.22)$$

and

$$\mathcal{N} = \int_\mathcal{L} \mathrm{d}l\, g(l, 0)g^*(l, 0). \quad (7.23)$$

γ_β is the dispersion of the initial Gaussian wavepacket and γ are those of the "frozen" sampling Gaussians over which the integration is performed.

7.1.3 Further Discussion

It is possible to gain further appreciation of the conditions necessary for DHK to achieve good accuracy by examining how DHK handles autocorrelations in a simpler hyperbolic system. As Figure 7.7 shows, if a coherent state is placed on the saddle point of this system, DHK actually fails miserably (LHK becomes nearly exact, as expected in a system that can be exactly linearized). On the other hand, if the coherent state is started displaced off of the saddle point, DHK fares far better (see Figure 7.7). This can be explained by noting that the former produces no appreciable action gradient in the overlap region between the initial and final state, and thus falls in the region of poor performance marked by ⊛ in Figure 7.6, whereas the latter's gradient is angled almost perpendicular to its major axis (as seen in the insets of Figure 7.7).

Unlike a "linearized" propagator, DHK relies on a one-dimensional integral that can best capture all the information of a higher dimensional phase space. When there is no modulating phase from the action, DHK's single integral will likely only perform well when the dynamics of the state are all captured by one parameter. A state in a hyperbolic system perched on top of the saddle-point sits there indefinitely while exhibiting *both* compression and stretching dynamics. On the other hand, a state displaced from the saddle point is instead mostly seen as translating away from the perspective of its initial state. The former dynamics would likely require at least two integrals to accurately capture if one of them is selected along the unstable manifold; the other would have to
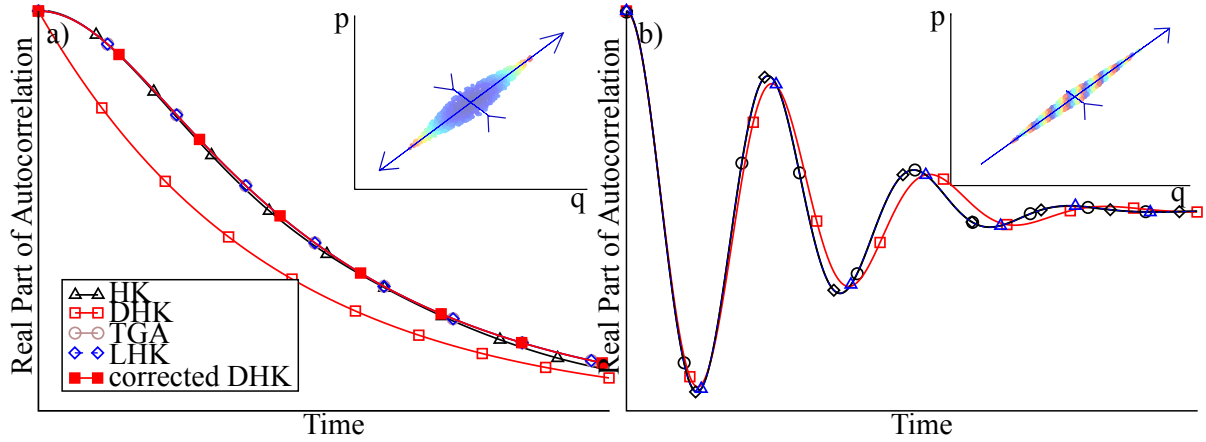
Figure 7.7: The real part of the autocorrelation for a coherent state obeying hyperbolic dynamics initially situated a) on the saddle point and b) off the saddle point. When $\mathcal{L}$ is selected to be along the unstable manifold, DHK performs better in the latter case. If $\mathcal{L}$ is angled to lie equally along stable and unstable manifolds, DHK's performance improves in the former case (producing the "corrected DHK" curve).

be chosen to take into account the compression dynamics. If we wish to have only one integral as in Eq. 7.11, both the compression and stretching dynamics need to be captured by the single manifold we choose. Therefore, we can perhaps imagine fixing DHK's inferior autocorrelation in this case by choosing $\mathcal{L}$ such that it lies equally along the stable and unstable manifold, thereby equally capturing the dynamics of both stretching and compressing. Such a change produces the "corrected DHK" curve in Figure 7.7. Though most systems would be difficult to treat in this way, this suggests that DHK's results may be improved for some states if a manifold not corresponding to the fastest growing one is chosen as its integral's domain.

7.1.4 Conclusions

Through a simple model of the dominant contributions to HK's integral during recurrences in one-dimensional systems, we showed what conditions are necessary for DHK's single integral to perform comparably when it is chosen to lie along the state's fastest growing manifold. In particular, we found that it generally works well as long as the action gradient during recurrences is not perpendicular to this manifold.

These conditions may also hold in more dimensions and may suggest why DHK often seems applicable in systems with greater than one dimension, though it remains to be verified that the trends discussed here remain true. It would be interesting to see if DHK's performance in many-dimensions, when $\mathcal{L}$ is chosen to be the fastest growing manifold of a state, are still contingent on the gradient of its action not lying perpendicular to $\mathcal{L}$. As we showed in our earlier Communication, DHK frequently works well in many-dimensional systems, so perhaps this is a limitation that is often sufficiently satisfied. For attempts at implementing DHK for coherent state autocorrelations in general systems that are at least quasi-periodic, we recommend the same method as the one used herein to find the best manifold $\mathcal{L}$ for DHK's integral domain; all the one-dimensional manifolds in Figure 7.5 (over which the integration was performed in DHK) were chosen by examining the stability matrix of the state's central classical trajectory, determining when its eigenvalues became real and their magnitudes maximal near either the trajectory's first or second quasi-return to its initial point, and choosing the associated eigenvector. This is the approach we found most success with and corresponds to approximately choosing the state's "fastest growing" manifold.

The formalism for DHK presented herein also suggests that the method can work quite well for anharmonic systems. In fact, the quartic potential examined in Figure 7.4 illustrates how well DHK performs for a system with a potential containing no global quadratic terms at all. However, in general the fastest growing manifold of such systems will not be linear and will exhibit some curvature since dynamics in higher than second order potentials are not completely described by linearizing their dynamics. This suggests that DHK may see improvement from selecting $\mathcal{L}$ to be a curved manifold. It would also be interesting to see how well DHK performs in chaotic or unbounded systems, where previous efforts in this direction have seen most improvement over HK (such as Filinov filtering).

7.2 Appendix

7.2.1 Parameters #1

HCl: $D = 37032$ cm^{-1}, $\alpha = 1.63219$ Å^{-1}, $\gamma_\beta = 75.7$ Å^{-2}, and $q_\beta = 1.87$ Å in excited degree of freedom. SO$_2$: $D = 57116$ cm^{-1}, $\alpha = 2.120$ Å^{-1}, $\gamma_\beta = 403.3$ Å^{-2}, $g_{qq'} = -0.01041$ a.m.u.$^{-1}$, $f_{qq'} = 0.0$ and $q_\beta = 1.01$ Å in excited degree of freedom. GeH$_4$: $D = 34716$ cm^{-1}, $\alpha = 1.41920$ Å^{-1}, $\gamma_\beta = 64.2$ Å^{-2}, $g_{qq'} = -0.00463465$ a.m.u.$^{-1}$, $f_{qq'} = 581.793$ cm^{-1}Å^{-2}, and $q_\beta = 1.51$ Å in excited degree of freedom. ^{184}WF$_6$: $D = 61270$ cm^{-1}, $\alpha = 1.465$ Å^{-1}, $\gamma_\beta = 366.6$ Å^{-2}, $g_{qq'} = -0.0014$ a.m.u.$^{-1}$, $f_{qq'} = 12890$ cm^{-1} for adjacent bonds, $f_{qq'} = 10810$ cm^{-1} for opposite bonds, and $q_\beta = 2.27$ Å in excited degree of freedom.

$q_\beta = p_\beta = 0.0$ in all other degrees of freedom. One-dimensional manifolds were chosen to be straight lines centered on $(\boldsymbol{p}_\beta, \boldsymbol{q}_\beta)$ with vector $(-1.0, -1.25 \times 10^{-4})$, $(7.02 \times 10^{-1}, 7.12 \times 10^{-1}, 1.61 \times 10^{-5}, 6.53 \times 10^{-6})$, $(0.1, -1.06 \times 10^{-2}, -1.05 \times 10^{-2}, -1.05 \times 10^{-2}, 1.19 \times 10^{-4}, 9.75 \times 10^{-7}, 9.75 \times 10^{-7}, 9.75 \times 10^{-7})$, and $(-9.97 \times 10^{-1}, 3.67 \times 10^{-2}, 3.67 \times 10^{-2}, 3.30 \times 10^{-2}, 3.67 \times 10^{-2}, 3.70 \times 10^{-2}, -2.03 \times 10^{-3}, 7.42 \times 10^{-5}, 7.42 \times 10^{-5}, 6.67 \times 10^{-5}, 7.42 \times 10^{-5}, 7.39 \times 10^{-5})$ for HCl, SO$_2$, GeH$_4$ and ^{184}WF$_6$ respectively (arbitrary units).

$\gamma = \gamma_\beta$ for all runs. To obtain spectra, Fourier transforms were performed on 1000 timesteps of 0.2 fs.

7.2.2 Derivation of LHK

We change the integration over phase space variables in HK to a new set $(l_0(\boldsymbol{q}_0, \boldsymbol{p}_0), \boldsymbol{n}_0(\boldsymbol{q}_0, \boldsymbol{p}_0))$, where l_0 lies along our chosen manifold and $\boldsymbol{n}_0$ are the remaining perpendicular degrees of freedom. The Jacobian of this transformation is equal to 1 since it is equivalent to just a rotation and translation of the $(\boldsymbol{p}_0, \boldsymbol{q}_0)$ variables.

We make an approximation by linearizing our action around $\boldsymbol{n}_0 = \boldsymbol{n}_\beta$ where $(l_\beta, \boldsymbol{n}_\beta) \equiv (\boldsymbol{p}_\beta, \boldsymbol{q}_\beta)$, and we define ζ to be the argument of the exponentials in Eq. 8.8 such that $g_\beta = \exp(\zeta)$,

$$\boldsymbol{u}(t) = \left[\left(\frac{\partial \zeta(\boldsymbol{p}_t(l_t, \boldsymbol{n}_t), \boldsymbol{q}_t(l_t, \boldsymbol{n}_t))}{\partial \boldsymbol{n}_0} \right)_{l_0} \right]_{\boldsymbol{n}_0 = \boldsymbol{n}_\beta}, \tag{7.24}$$

and

$$\boldsymbol{U}(t) = \left[\left(\frac{\partial^2 \zeta(\boldsymbol{p}_t(l_t, \boldsymbol{n}_t), \boldsymbol{q}_t(l_t, \boldsymbol{n}_t))}{\partial \boldsymbol{n}_0^2} \right)_{l_0} \right]_{\boldsymbol{n}_0 = \boldsymbol{n}_\beta}, \tag{7.25}$$

so that we can express $g_\beta(\boldsymbol{p}(l_t, \boldsymbol{n}_t), \boldsymbol{q}(l_t, \boldsymbol{n}_t))$ more easily in terms of the new coordinates:

$$g_\beta(l_0, \boldsymbol{n}_0) = \exp\left\{ \frac{1}{2}(\boldsymbol{n}_0 - \boldsymbol{n}_\beta) \cdot \boldsymbol{U}(0) \cdot (\boldsymbol{n}_0 - \boldsymbol{n}_\beta)^T + \boldsymbol{u}(0) \cdot (\boldsymbol{n}_0 - \boldsymbol{n}_\beta)^T + \zeta\left(\boldsymbol{p}(l_0, \boldsymbol{n}_\beta), \boldsymbol{q}(l_0, \boldsymbol{n}_\beta)\right) \right\} \tag{7.26}$$

and

$$g_\beta^*(l_t, \boldsymbol{n}_0) = \exp\left\{ \frac{1}{2}(\boldsymbol{n}_0 - \boldsymbol{n}_\beta) \cdot \boldsymbol{U}^*(t) \cdot (\boldsymbol{n}_0 - \boldsymbol{n}_\beta)^T + \boldsymbol{u}^*(t) \cdot (\boldsymbol{n}_0 - \boldsymbol{n}_\beta)^T + \zeta^*\left(\boldsymbol{p}(l_t, \boldsymbol{n}_t), \boldsymbol{q}(l_t, \boldsymbol{n}_t)\right) |_{\boldsymbol{n}_0 = \boldsymbol{n}_\beta} \right\}. \tag{7.27}$$

We also linearize the action:

$$S_t^{\text{lin}}(\boldsymbol{p}_0, \boldsymbol{q}_0) = S_t^{\text{lin}}(l_0, \boldsymbol{n}_0) \equiv S_t(l_0, \boldsymbol{n}_0 = \boldsymbol{n}_\beta) + \left(\frac{\partial S_t}{\partial \boldsymbol{n}_0} \right)_{l_0} \Big|_{\boldsymbol{n}_0 = \boldsymbol{n}_\beta} \cdot (\boldsymbol{n}_0 - \boldsymbol{n}_\beta)^T \tag{7.28}$$

$$+ \frac{1}{2}(\boldsymbol{n}_0 - \boldsymbol{n}_\beta) \cdot \left(\frac{\partial^2 S_t}{\partial \boldsymbol{n}_0^2} \right)_{l_0} \Big|_{\boldsymbol{n}_0 = \boldsymbol{n}_\beta} \cdot (\boldsymbol{n}_0 - \boldsymbol{n}_\beta)^T. \tag{7.29}$$

We neglect all derivatives that are higher order than the stability matrix elements.

Hence the integral becomes,

$$\langle \Psi_\beta(0) | \Psi_\beta(t) \rangle_{\text{HK}} \approx \left(\frac{\sqrt{\gamma \gamma_\beta}}{\pi \hbar (\gamma + \gamma_\beta)} \right)^N \int \mathrm{d}l_0 \int \mathrm{d}\boldsymbol{n}_0 C_t(l_0, \boldsymbol{n}_0) g_\beta(l_0, \boldsymbol{n}_0) g_\beta^*(l_t, \boldsymbol{n}_0) \exp\left[i S_t^{\text{lin}}(l_0, \boldsymbol{n}_0)/\hbar \right]. \tag{7.30}$$

We perform the Gaussian integral over $\boldsymbol{n}_0$ linearized around $\boldsymbol{n}_\beta$ to obtain the LHK:

$$\langle \Psi_\beta(0) | \Psi_\beta(t) \rangle_{\text{LHK}} = \int_{-\infty}^{\infty} \mathrm{d}l_0 \int_{-\infty}^{\infty} \mathrm{d}\boldsymbol{n}_0 \mathcal{N}(l_0) \exp\left[-\frac{1}{2}(\boldsymbol{n}_0 - \boldsymbol{n}_\beta) \cdot \boldsymbol{A}(l_0, t) \cdot (\boldsymbol{n}_0 - \boldsymbol{n}_\beta)^T + \boldsymbol{b}(l_0) \cdot (\boldsymbol{n}_0 - \boldsymbol{n}_\beta)^T \right] \tag{7.31}$$

$$= \int_{-\infty}^{\infty} \mathrm{d}l_0 \mathcal{N}(l_0) \left(\frac{(2\pi)^{2N-1}}{\det \boldsymbol{A}(l_0, t)} \right)^{1/2} \exp\left(\frac{1}{2} \boldsymbol{b}(l_0, t) \cdot \boldsymbol{A}(l_0, t)^{-1} \cdot \boldsymbol{b}(l_0, t)^T \right), \tag{7.32}$$

where

$$\boldsymbol{A}(l_0, t) = -\left[\boldsymbol{U}(0) + \boldsymbol{U}^*(t) + \frac{i}{\hbar} \left(\frac{\partial^2 S_t}{\partial \boldsymbol{n}_0^2} \right)_{l_0} \Big|_{\boldsymbol{n}_0 = \boldsymbol{n}_\beta} \right], \tag{7.33}$$

$$\boldsymbol{b}(l_0, t) = \left[\boldsymbol{u}(0) + \boldsymbol{u}^*(t) + \frac{i}{\hbar} \left(\frac{\partial S_t}{\partial \boldsymbol{n}_0} \right)_{l_0} \bigg|_{\boldsymbol{n}_0 = \boldsymbol{n}_\beta} \right], \tag{7.34}$$

and

$$\mathcal{N}(l_0, \boldsymbol{n}_0) = \left(\frac{\sqrt{\gamma \gamma_\beta}}{\pi \hbar (\gamma + \gamma_\beta)} \right)^N C_t(\boldsymbol{p}_0(l_0), \boldsymbol{q}_0(l_0)) e^{iS_t(l_0, \boldsymbol{n}_0 = \boldsymbol{n}_\beta)/\hbar} \tag{7.35}$$
$$\times \exp \left\{ \zeta(\boldsymbol{p}(l_0, \boldsymbol{n}_\beta), \boldsymbol{q}(l_0, \boldsymbol{n}_\beta)) + \zeta^*(\boldsymbol{p}(l_t, \boldsymbol{n}_t), \boldsymbol{q}(l_t, \boldsymbol{n}_t)) |_{\boldsymbol{n}_0 = \boldsymbol{n}_\beta} \right\}.$$

Combining all of this together in one expression we find:

$$\langle \Psi_\beta(0) | \Psi_\beta(t) \rangle_{\text{LHK}} = \int_{-\infty}^{\infty} dl_0 \left(\frac{\sqrt{\gamma \gamma_\beta}}{\pi \hbar (\gamma + \gamma_\beta)} \right)^N C_t(\boldsymbol{p}_0(l_0, \boldsymbol{n}_0 = \boldsymbol{n}_\beta), \boldsymbol{q}_0(l_0, \boldsymbol{n}_0 = \boldsymbol{n}_\beta)) \left(\frac{(2\pi)^{2N-1}}{\det \boldsymbol{A}(l_0, t)} \right)^{1/2} e^{iS_t(l_0, \boldsymbol{n}_0 = \boldsymbol{n}_\beta)/\hbar}$$
$$\times \exp \left\{ \zeta(\boldsymbol{p}(l_0, \boldsymbol{n}_\beta), \boldsymbol{q}(l_0, \boldsymbol{n}_\beta)) + \zeta^*(\boldsymbol{p}(l_t, \boldsymbol{n}_t), \boldsymbol{q}(l_t, \boldsymbol{n}_t)) |_{\boldsymbol{n}_0 = \boldsymbol{n}_\beta} \right\} \tag{7.36}$$
$$\times \exp \left(\frac{1}{2} \boldsymbol{b}(l_0, t) \cdot \boldsymbol{A}(l_0, t)^{-1} \cdot \boldsymbol{b}(l_0, t)^T \right).$$

7.2.3   Derivation of Eq. 7.14

Suppose we start with a Gaussian $\Psi_\beta(q, 0) = \left(\frac{\Re \gamma_0}{\pi} \right)^{\frac{1}{4}} \exp \left[-\frac{\gamma_0}{2}(q - q_\beta^2) + \frac{i}{\hbar} p_\beta(q - q_\beta) \right]$ where $\gamma_0 \in \mathbb{R}$ (a coherent state) and we are interested in its return to overlap itself at (p_β, q_β) at some time t. We consider the case that the state has remained a Gaussian but has acquired a new dispersion $\gamma_t \in \mathbb{C}$ (i.e. the state may now be rotated and squeezed with respect to its initial state). If this Gaussian's major axis is rotated with respect to the p- or q-axis then $\Delta q \Delta p = \frac{\hbar}{2} \sqrt{1 + \frac{\Re \gamma_t^2}{\Im \gamma_t^2}} > \frac{\hbar}{2}$. This corresponds to a Gaussian aligned with some major and minor axes rotated by θ to the p, q-axes in whose frame $\Im \gamma = 0$. It can be shown[3] that

$$\Re \gamma_t = \frac{\gamma}{d(\theta)}, \tag{7.37}$$

$$\Im \gamma_t = \frac{(1 - \gamma^2 \hbar^2) \sin \theta \cos \theta}{\hbar d(\theta)}, \tag{7.38}$$

where

$$d(\theta) = \cos^2 \theta + \gamma^2 \hbar^2 \sin^2 \theta. \tag{7.39}$$

If $\gamma = \frac{1}{\hbar}$ then the Gaussian appears to be a circle in phase space. For $\gamma > \frac{1}{\hbar}$ ($\gamma < \frac{1}{\hbar}$) its major axis corresponds to the p-axis (q-axis) in the rotated frame.

The Wigner transform of these Gaussians is

$$
\begin{aligned}
\rho_W(p,q) &= \frac{1}{2} \int_{-\infty}^{\infty} ds \Psi_\beta \left(q - \frac{s}{2}, t \right) \Psi_\beta^* \left(q + \frac{s}{2}, t \right) \exp \left(\frac{i}{\hbar} sp \right) \tag{7.40} \\
&= \exp \left[-\gamma_t \left(2 - \frac{\gamma_t}{\Re\gamma_t} \right) (q - q_\beta)^2 - \frac{(p - p_\beta)^2}{\hbar^2 \Re\gamma_t} + \frac{2i}{\hbar} \left(\frac{\gamma_t}{\Re\gamma_t} - 1 \right) (q - q_\beta)(p - p_\beta) \right]. \tag{7.41}
\end{aligned}
$$

Using Eqs. 7.37 and 7.38, this can be reexpressed in a more intuitive form as Eq. 7.14.

7.2.4 Parameters #2

All results were obtained with $\hbar = 1$. We express all quantities below as defined in Eqs. 7.19-7.23.

For the quartic oscillator results, the mass was $m = 0.979573$, the potential was $V = \omega q^4$ with $\omega = 2012640.0$. The states A-D all had dispersions $\gamma_\beta = \gamma = \frac{1.0}{0.0425615^2}$. In particular, for A, $(p_\beta, q_\beta) = (0.0, 0.4)$, $\mathcal{L} = (-0.999997388, 0.00228581084)$ and the timestep $\delta t = 0.00002$; for B, $(p_\beta, q_\beta) = (240.0, 0.0)$, $\mathcal{L} = (0.999999993, 0.000114148579)$, and $\delta t = 0.00002$; for C, $(p_\beta, q_\beta) = (0.0, 0.1)$, $\mathcal{L} = (0.999832662, -0.0182933862)$, and $\delta t = 0.00004$; and for D, $(p_\beta, q_\beta) = (80.0, 0.0)$, $\mathcal{L} = (0.999999997, 0.0000743170501)$, and $\delta t = 0.00004$.

For the inverted oscillator results, the mass was $m = 1$, and the potential was $V = -m\omega^2 q^2$ with $\omega = 1.0$. The dispersion was $\gamma_\beta = \gamma = 1.0$. The timestep was $\delta t = 0.0005$. The state displaced off the saddle point began at $(p_\beta, q_\beta) = (0.0, 10.0)$.

8

Generalized Dephasing Relation for Fidelity and Application as an Efficient Propagator

In this chapter we introduce the dephasing relation (DR), a linearization of semiclassical fidelity, and then generalize it to include the overlap of "off-diagonal" elements. The accuracy of the formulation is tested in integrable and chaotic systems and its scaling with dimensionality is studied in a Caldeira-Leggett model with many degrees of freedom. It is shown that the DR is often in very good agreement with numerically analytic quantum results and frequently outperforms an alternative semiclassical treatment. Most importantly, since there is no computationally expensive prefactor, and facilitated by Monte Carlo Metropolis sampling, calculation of the DR is found to scale remarkably well with increasing dimension. We further demonstrate that a propagator based on the DR can include more quantum coherence and outperform other popular linearized semiclassical methods, such as FBSD and LSC-IVR.

8.1   Introduction

We define a general notion of fidelity as,

$$F(t) = |O(t)|^2 = |\langle \Psi_B | e^{iH^{\epsilon}t/\hbar} e^{-iH^0 t/\hbar} | \Psi_A \rangle|^2 \tag{8.1}$$

where $H^\epsilon = H^0 + \epsilon V$. This can be described from the Loschmidt echo perspective as an initial state Ψ_A that is propagated forward for some time t obeying the Hamiltonian H^0 and then propagated back for the same time obeying the perturbed Hamiltonian H^ϵ. After this forward-backward propagation, the inner product with a state Ψ_B is considered. An equivalent description is as the overlap between states Ψ_A and Ψ_B both of which have been forward-propagated for time t but obeying different Hamiltonians, H^0 and H^ϵ, respectively. In either case, fidelity will range from being equal to 1 when the time-propagated Ψ_A and Ψ_B wavefunctions are the same, to 0 when they are fully orthogonal.

Over the years, a linearized Wigner transform of this expression has been defined in one form or another[46, 47, 48, 49, 50, 51, 52, 53, 54, 55]. Most recently, Vanicek and coworkers derived a prefactorless form that they have called the "dephasing" relation (DR)[56, 57]. They have shown that the DR possesses many promising features, the most notable that the expression scales independently of dimension when sampled appropriately[58]. Furthermore, they report that in general, the more complex H^0 and H^ϵ are, the better the DR works[59].

Many efforts have been made to develop an accurate semiclassical propagator that does not contain a prefactor dependant on the computationally costly propagation of stability (monodromy) matrices. Much of this work has been focused on the linearization of existing semiclassical methods. Perhaps the most successful are those pioneered by Makri and coworkers[60, 61] and Miller and coworkers[62, 63]. In their work, an additional stationary phase approximation (SPA) is made to combine the forward and backward propagators that are present in many correlation functions. This produces the prefactorless simplified expressions called the FBSD and the LSC-IVR respectively. Unfortunately, the SPA takes away quantum dynamical effects (quantum correlations) which leaves these methods with short applicable timescales in many systems[60]. There have been many suggestions made to improve these expressions[64, 65] but this is often found to be difficult without the inclusion of stability matrix elements.

Here, we propose a very different approach for linearization based around fidelity and its efficient calculation by the DR. The main result we present is a semiclassical propagator that

contains quantum dynamical effects, unlike its predecessors, and is computationally cheap because it remains free of any dependance on stability matrices.

This chapter is organized as follows: The expression that results from extending the DR to include "off-diagonal" elements (where $\Psi_A \neq \Psi_B$) is presented in Section 8.2 along with an alternate semiclassical result to be used as a comparison. Section 8.3.1 compares the performance of these two expressions when applied to two-dimensional test systems that are integrable and chaotic. Section 8.3.2 further compares their performance with a Caldeira-Leggett model involving many more degrees of freedom. Section 8.4 shows how the DR can be used as a semiclassical propagator and demonstrates its promising ability to include quantum coherence for longer times. Section 8.5 concludes the discussion and offers some potential applications for the DR-based propagator.

8.2 Generalized dephasing relation

Fidelity has traditionally been defined and explored in Eq. 8.1 with $\Psi_A = \Psi_B \equiv \Psi$. This "diagonal" version has been found to be well approximated by a clever first-order perturbative expansion of its semiclassical Wigner transform[66, 59]. Neglecting a prefactor, the resultant simplified expression consists of an integral over the Wigner function of $\Psi(t = 0)$ multiplied by a time-dependent phase term. The form of this compact expression led Vanicek and coworkers to call it the "dephasing relation".

Extending the DR to handle cases where $\Psi_A \neq \Psi_B$ produces a generalized form of fidelity capable of handling the "off-diagonal" elements that are necessary in any applications as a meaningful propagator. A thorough derivation for "diagonal" elements has been presented in the literature[66, 59] and can be extended to "off-diagonal" elements simply by setting $\Psi_A \neq \Psi_B$. The main results are reprinted here.

Consider the Hamiltonians H^0 and $H^\epsilon \equiv H^0 + \epsilon V$. Taking the primitive semiclassical expression for Eq. 8.1 up to zeroth order in ϵ for the prefactor (ie. neglecting it) and up to first

order in ϵ for the phase, where the perturbation is taken around the trajectory obeying the mean Hamiltonian $((H^\epsilon + H^0)/2)$,

$$
\begin{aligned}
O(t) &= O_{\text{DR}}^{AB}(t) \\
&\equiv h^{-d} \int d\boldsymbol{q}^0 d\boldsymbol{p}^0 \rho_W^{AB}(\boldsymbol{q}^0, \boldsymbol{p}^0) e^{iS_{\text{DR}}(\boldsymbol{q}^0, \boldsymbol{p}^0; t)/\hbar}
\end{aligned}
\tag{8.2}
$$

in a d dimensional system where

$$
\rho_W^{AB}(\boldsymbol{q}^0, \boldsymbol{p}^0) \equiv \int d\boldsymbol{s} \left\langle \boldsymbol{q}^0 - \boldsymbol{s}/2 \, | \Psi_A \right\rangle \left\langle \Psi_B \, | \boldsymbol{q}^0 + \boldsymbol{s}/2 \right\rangle e^{i\boldsymbol{s}\cdot\boldsymbol{p}^0/\hbar}
\tag{8.3}
$$

is the Wigner transform of $|\Psi_A\rangle \langle \Psi_B|$ and

$$
S_{\text{DR}}(\boldsymbol{q}^0, \boldsymbol{p}^0; t) \equiv -\epsilon \int_0^t d\tau V(\boldsymbol{q}_\tau, \boldsymbol{p}_\tau, \tau),
\tag{8.4}
$$

with $(\boldsymbol{q}_\tau, \boldsymbol{p}_\tau)$ following the classical trajectory of the average Hamiltonian $(H^0 + H^\epsilon)/2$.

The Wigner transform differs from that presented in the traditional DR solely in that ρ_W consists of the operator $|\Psi_A\rangle \langle \Psi_B|$ instead of $|\Psi\rangle \langle \Psi|$.

Position States

If we consider position states in Eq. 8.1 such that $\Psi_A(\boldsymbol{q}) = \delta(\boldsymbol{q} - \boldsymbol{q}_A)$ and $\Psi_B(\boldsymbol{q}) = \delta(\boldsymbol{q} - \boldsymbol{q}_B)$ then the expression in Eq. 8.2 simpilifies to:

$$
\begin{aligned}
O_{\text{DR}}^{AB}(t) &= \frac{1}{(2\pi\hbar)^d} \\
&\times \int d\boldsymbol{p} \, \exp\left[\frac{i}{\hbar}(\boldsymbol{q}_A - \boldsymbol{q}_B) \cdot \boldsymbol{p} + \frac{i}{\hbar} S_{\text{DR}}\left(\frac{\boldsymbol{q}_A + \boldsymbol{q}_B}{2}, \boldsymbol{p}; t\right)\right].
\end{aligned}
\tag{8.5}
$$

Momentum States

Similarly, for $\Psi_A(\boldsymbol{p}) = \delta(\boldsymbol{p} - \boldsymbol{p}_A)$ and $\Psi_B(\boldsymbol{p}) = \delta(\boldsymbol{p} - \boldsymbol{p}_B)$,

$$O_{\text{DR}}^{AB}(t) = \frac{1}{(2\pi\hbar)^d}$$
$$\times \int d\boldsymbol{q} \, \exp\left[\frac{i}{\hbar}(\boldsymbol{p}_A - \boldsymbol{p}_B) \cdot \boldsymbol{q} + \frac{i}{\hbar}S_{\text{DR}}\left(\boldsymbol{q}, \frac{\boldsymbol{p}_A + \boldsymbol{p}_B}{2}; t\right)\right]. \tag{8.6}$$

Gaussian States

For $\Psi_A(\boldsymbol{q}) = (\pi\sigma^2)^{-\frac{d}{4}} \exp\left[-\frac{(\boldsymbol{q}-\boldsymbol{q}_A)^2}{2\sigma^2} + \frac{i\boldsymbol{p}_A \cdot (\boldsymbol{q}-\boldsymbol{q}_A)}{\hbar}\right]$ and $\Psi_B(\boldsymbol{q}) = (\pi\sigma^2)^{-\frac{d}{4}} \exp\left[-\frac{(\boldsymbol{q}-\boldsymbol{q}_B)^2}{2\sigma^2} + \frac{i\boldsymbol{p}_B \cdot (\boldsymbol{q}-\boldsymbol{q}_B)}{\hbar}\right]$,

$$O_{\text{DR}}^{AB}(t) = \frac{1}{(\pi\hbar)^d} \int d\boldsymbol{q} \int d\boldsymbol{p}$$
$$\times \exp\left\{ -\left[\frac{(\boldsymbol{q}_A + \boldsymbol{q}_B - 2q)^2}{4\sigma^2} + \frac{(\boldsymbol{p}_A + \boldsymbol{p}_B - 2\boldsymbol{p})^2\sigma^2}{4\hbar^2} \right.\right.$$
$$-i(\frac{(\boldsymbol{p}_A - \boldsymbol{p}_B) \cdot (\boldsymbol{q}_A + \boldsymbol{q}_B - 2\boldsymbol{q})}{2\hbar}$$
$$\left.\left. + \frac{\boldsymbol{p} \cdot (\boldsymbol{q}_A - \boldsymbol{q}_B)}{\hbar})\right] + \frac{i}{\hbar}S_{\text{DR}}\left(\boldsymbol{q}, \boldsymbol{p}; t\right) \right\}. \tag{8.7}$$

These three examples illustrate how calculating "off-diagonal" elements of the DR introduces an additional phase into the traditional formula for "diagonal" elements as well as a slightly different phase integral in Eqs. 8.5 and 8.6 but does not make evaluation any more difficult.

Forward-Backward Semiclassical Expression

Substituting the Heller-Herman-Kluk-Kay coherent state version of the semiclassical propagator for the quantum propagators in Eq. 8.1 yields,

$$O(t)_{\text{HK}} = \frac{1}{(2\pi\hbar)^{2d}} \int d\boldsymbol{q}_0^0 \int d\boldsymbol{p}_0^0 \int d\boldsymbol{q}_0^\epsilon \int d\boldsymbol{p}_0^\epsilon$$
$$\times C_t(\boldsymbol{q}_0^0, \boldsymbol{p}_0^0) C_t(\boldsymbol{q}_0^\epsilon, \boldsymbol{p}_0^\epsilon)^* \langle \boldsymbol{q}_0^0, \boldsymbol{p}_0^0 | \Psi_A \rangle \tag{8.8}$$
$$\times \langle \Psi_B | \boldsymbol{q}_0^\epsilon, \boldsymbol{p}_0^\epsilon \rangle e^{i(S_t^0 - S_t^\epsilon)\hbar} \langle \boldsymbol{q}_t^\epsilon, \boldsymbol{p}_t^\epsilon | \boldsymbol{q}_t^0, \boldsymbol{p}_t^0 \rangle,$$

where $C_t(\boldsymbol{q}_0, \boldsymbol{p}_0) = \sqrt{\det\left[\frac{1}{2}\left(\frac{\partial \boldsymbol{q}_t}{\partial \boldsymbol{q_0}} + \frac{\partial \boldsymbol{p}_t}{\partial \boldsymbol{p}_0} - i\gamma\hbar\frac{\partial \boldsymbol{q}_t}{\partial \boldsymbol{p}_0} + \frac{i}{\gamma\hbar}\frac{\partial \boldsymbol{p}_t}{\partial \boldsymbol{q}_0}\right)\right]}$.

This integral is difficult to evaluate numerically due to the oscillating double phase. Taking a SPA of the final term in Eq. 8.8 simplifies matters. The details are presented in Appendix 8.6.1 wherein taking the SPA is shown to be equivalent to assuming $\langle \boldsymbol{q}_t^\epsilon, \boldsymbol{p}_t^\epsilon | \boldsymbol{q}_t^0, \boldsymbol{p}_t^0 \rangle = \delta\left(\boldsymbol{q}_t^\epsilon - \boldsymbol{q}_t^0\right)\delta\left(\boldsymbol{p}_t^\epsilon - \boldsymbol{p}_t^0\right)$. This allows the double-phase space integral to be replaced by a single one over a new set of coordinates $(\boldsymbol{q}, \boldsymbol{p})$ that are defined to start out at $(\boldsymbol{q}_0^0, \boldsymbol{p}_0^0)$, forward-propagate under H^0 to $(\boldsymbol{q}_t^0, \boldsymbol{p}_t^0) = (\boldsymbol{q}_t^\epsilon, \boldsymbol{p}_t^\epsilon)$, and finally return via back-propagation under H^ϵ to $(\boldsymbol{q}_0^\epsilon, \boldsymbol{p}_0^\epsilon)$. The final result is,

$$O(t)_{\text{FB-HKR}} = \frac{1}{(2\pi\hbar)^{2d}}\int d\boldsymbol{q}_0 \int d\boldsymbol{p}_0 \tag{8.9}$$
$$\times C_t(\boldsymbol{q}_0, \boldsymbol{p}_0)\,\langle \boldsymbol{q}_0,\,\boldsymbol{p}_0\,|\Psi_A\rangle\,\langle\Psi_B\,|\boldsymbol{q}_0^\epsilon,\,\boldsymbol{p}_0^\epsilon\rangle\,e^{i(S_t^0 - S_t^\epsilon)\hbar}.$$

This expression will be referred to as the "Forward-Backward Heller-Herman-Kluk-Kay relation" (FB-HKR). It is quite different from the DR; FB-HKR is accurate up to the assumption $\langle \boldsymbol{q}_t^\epsilon,\,\boldsymbol{p}_t^\epsilon | \boldsymbol{q}_t^0,\,\boldsymbol{p}_t^0 \rangle = \delta\left(\boldsymbol{q}_t^\epsilon - \boldsymbol{q}_t^0\right)\delta\left(\boldsymbol{p}_t^\epsilon - \boldsymbol{p}_t^0\right)$ while the DR is accurate up to first order in ϵ in phase and zeroth order in the prefactor. Also, due to the prefactor containing monodromy matrix elements, the FB-HKR is more computationally expensive than the generalized DR. Nevertheless, the FB-HKR is introduced to serve, at the very least, as a qualitative semiclassical benchmark against which the accuracy of the DR can be compared, especially in higher dimensional systems where a full numerically analytic solution proves too costly.

8.3   Numerical Tests

Perhaps the most attractive feature of the DR is its excellent scaling with dimension while the most important limitation is its dependence on small perturbations ϵ for accurate performance. This suggests that it has a natural application in the time-propagation of many-dimensional systems that are weakly coupled to each other. To study the DR's performance in such applications, a
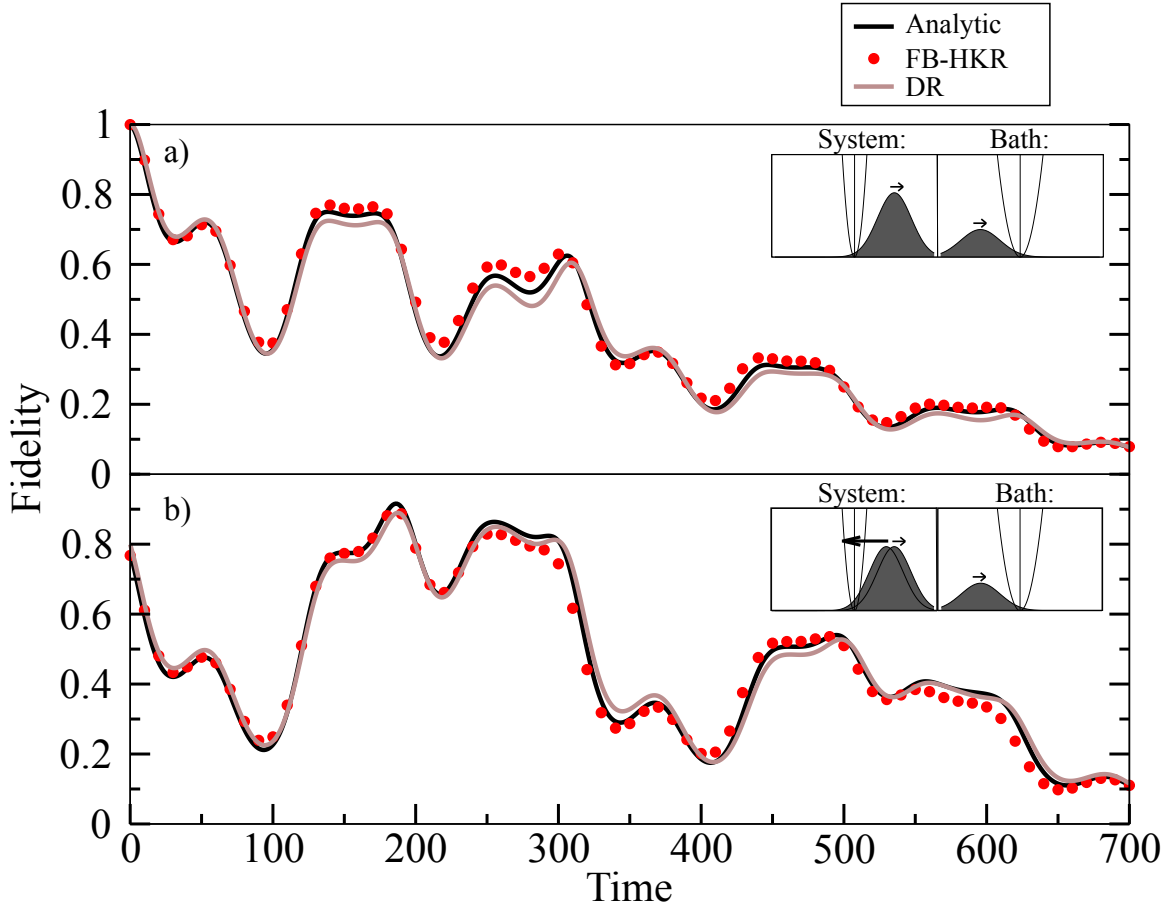
Figure 8.1: The initial states for the system and bath harmonic oscillators are Gaussian wave packets propagating under a bilinear coupling ($\epsilon q_{\mathrm{sys}} q_{\mathrm{bath}}$) with parameters $\epsilon = 10, \hbar = 1, \Delta t = 0.01,$ $t = 700\Delta t, m_{\mathrm{sys}} = 10, m_{\mathrm{bath}} = 2, \omega_{\mathrm{sys}} = 5, \omega_{\mathrm{bath}} = 3, \sigma_{\mathrm{sys}} = 0.3$ and $\sigma_{\mathrm{bath}} = 0.7$ where a) shows "diagonal fidelity" ($q_{\mathrm{sys}}^{\mathrm{init}} = p_{\mathrm{sys}}^{\mathrm{init}} = 0.5, q_{\mathrm{bath}}^{\mathrm{init}} = -1$ and $p_{\mathrm{bath}}^{\mathrm{init}} = 0.5$) and b) shows "off-diagonal fidelity" ($q_{\mathrm{sys} \text{'B'}}^{\mathrm{init}} = 0.4$ and $p_{\mathrm{sys} \text{'B'}}^{\mathrm{init}} = -1.5$). Inset: A cartoon of initial system and bath states.

number of numerical tests were performed on weakly coupled systems with two degrees of freedom (Figures 8.1-8.3) as well as many more degrees of freedom (Figure 8.5) which propagated freely of each other forward in time but were coupled when returning backward in time. What follows is a short summary of their behavior according to the DR.

8.3.1 Two Dimensional Systems

Figure 8.1 compares the fidelity of two rather different harmonic oscillators that are coupled bilinearly together. The DR agrees with the numerically analytic results very well. It is important to

91

differentiate the set-up that produced this result from those in prior studies where the DR was found to break down in harmonic oscillators with significantly different force constants [67]. Whereas Figure 8.1 shows two harmonic oscillators with different force constants which were propagated independently of each other forward in time but were coupled together backward in time, these previous studies dealt with cases where each harmonic oscillator had a different force constant going forward in time compared to backward in time. The situation presented here seems to be much more accurately reproduced by the DR, even for harmonic oscillators with very different force constants.

Figure 8.2 and the inset of figure 8.5 also show good agreement between the DR and numerically analytic results for the fidelity of a Morse oscillator coupled bilinearly to a significantly different harmonic oscillator.

A very similar expression to the DR has been derived somewhat heuristically using the Shadowing Theorem[57] which relies on the accuracy of trajectories that "shadow" exact trajectories. Only hyperbolic Hamiltonians have been shown to be capable of such shadowing for infinite time. It is perhaps for this reason that, in Figure 8.3, the DR shows great accuracy at reproducing the analytic fidelity of two bilinearly coupled hyperbolic systems.

Figure 8.4 shows good short-time agreement but poor long-time agreement with the numerically analytic results for the fidelity of two different quartic oscillators that are coupled together biquadratically. This is an interesting example because this system is integrable going forward in time, when the oscillators are uncoupled, but chaotic backward in time when they are coupled. The FB-HKR results diverge after a short-time due to monodromy matrix divergence, a common occurence in chaotic systems. There are methods to deal with this, some as simple as throwing away divergent trajectories[68].

In general it is found that the DR results for "diagonal" and "off-diagonal" cases of fidelity agree with analytic results for the same amount of time in any system studied. In each case, calculations were shown for only a single value of ϵ that produced interesting fidelity decay. Larger values of ϵ and DR calculations at longer times generally produce poorer agreement with analytic
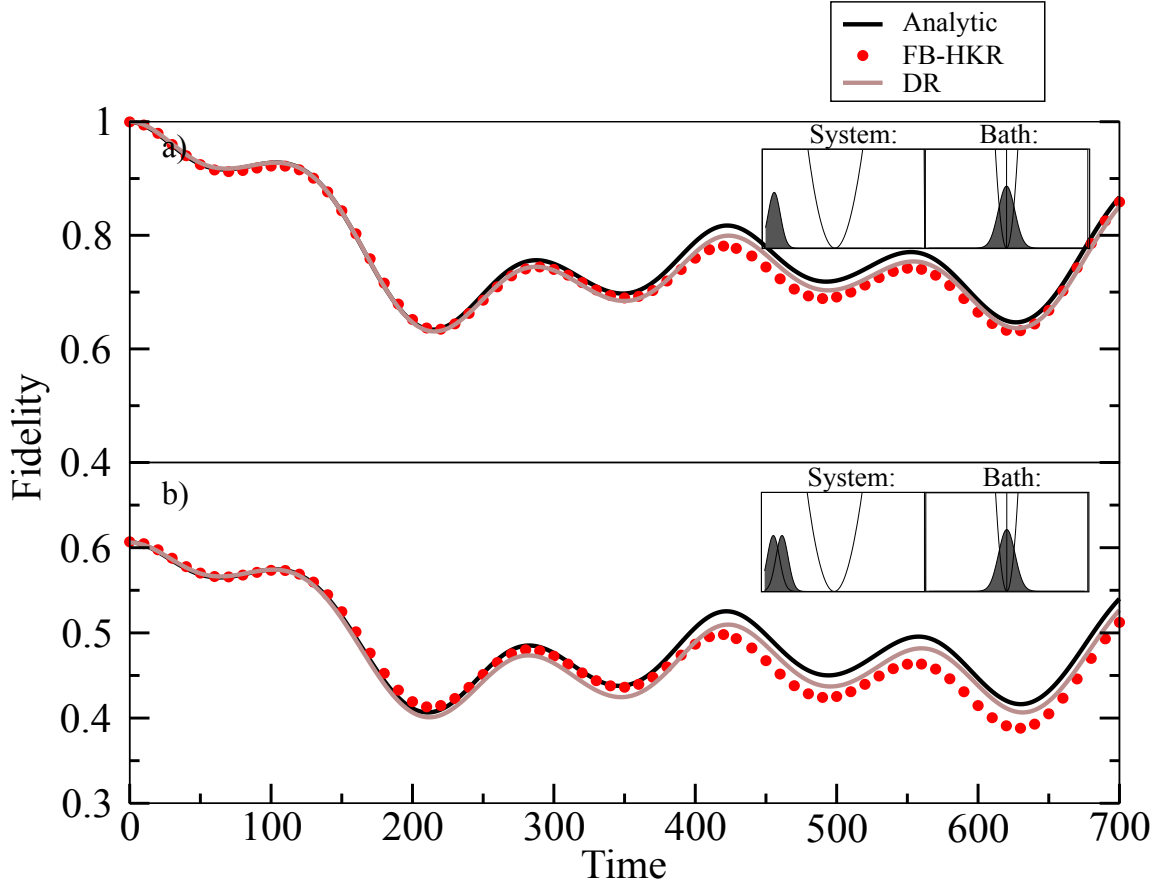
Figure 8.2: Initial state for the system Morse oscillator ($D(1 - e^{-\alpha(q_{bath} - q_e)})^2$) and bath harmonic oscillator are Gaussians coupled bilinearly ($\epsilon q_{sys} q_{bath}$) with parameters $\epsilon = 10$, $\hbar = 1$, $\Delta t = 0.001$, $t = 700\Delta t$, $m_{sys} = 10$, $m_{bath} = 8$, $D = 10000$, $\alpha = 0.1$, $qe = 3$, $\omega_{bath} = 3$, $\sigma_{sys} = 0.1$ and $\sigma_{bath} = 0.3$ where a) shows "diagonal fidelity" ($q_{sys}^{init} = 2.3$ and $p_{sys}^{init} = q_{bath}^{init} = p_{bath}^{init} = 0$) and b) shows "off-diagonal fidelity" ($q_{sys\,'B'}^{init} = 2.4$ and $p_{sys\,'B'}^{init} = 0.0$). Inset: A cartoon of initial system and bath states.
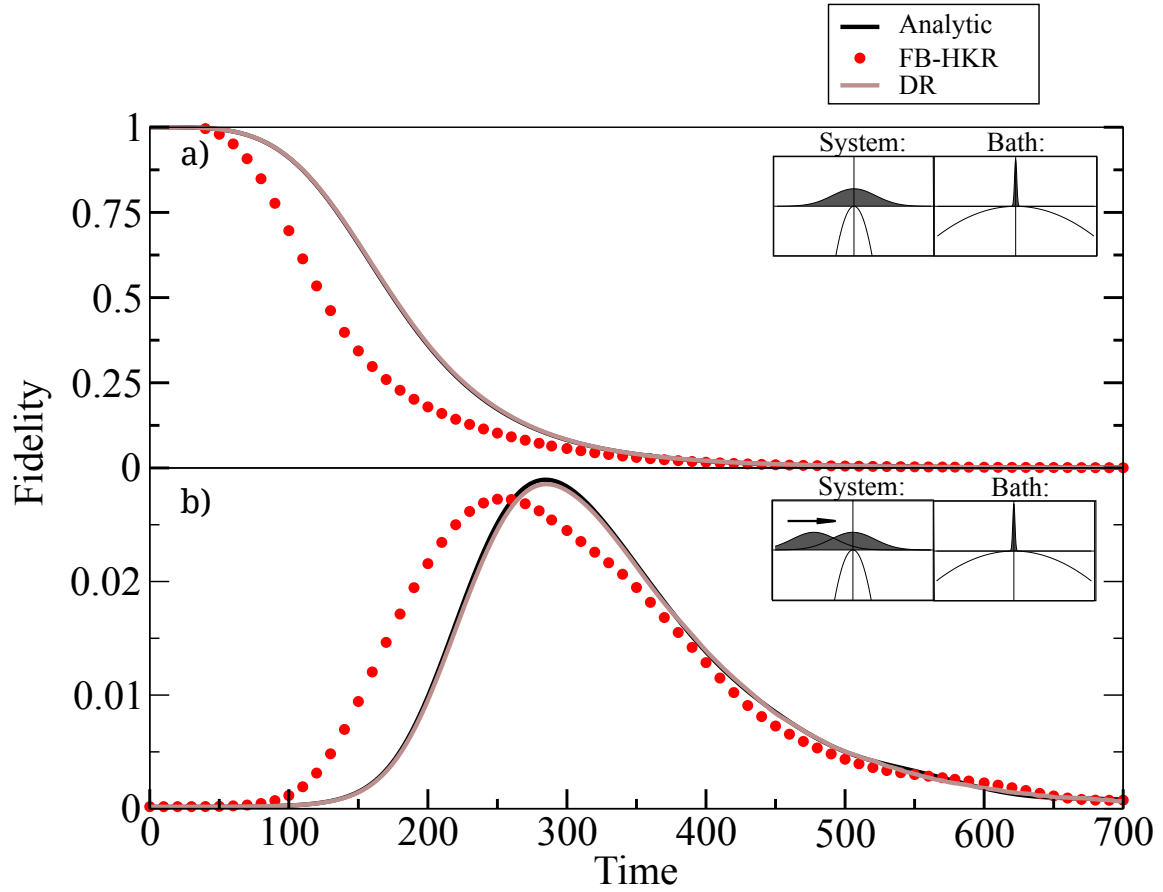
Figure 8.3: Initial state for the system and bath obeying the hyperbolic Hamiltonian are Gaussians coupled bilinearly ($\epsilon q_{\text{sys}} q_{\text{bath}}$) with parameters $\epsilon = 3$, $\hbar = 1$, $\Delta t = 0.001$, $t = 700\Delta t$, $m_{\text{sys}} = 2$, $m_{\text{bath}} = 0.1$, $\omega_{\text{sys}} = 3$, $\omega_{\text{bath}} = 0.6$, $\sigma_{\text{sys}} = 0.8$ and $\sigma_{\text{bath}} = 0.2$ where a) shows "diagonal fidelity ($q_{\text{sys}}^{\text{init}} = p_{\text{sys}}^{\text{init}} = q_{\text{bath}}^{\text{init}} = p_{\text{bath}}^{\text{init}} = 0$) and b) shows "off-diagonal fidelity" ($q_{\text{sys 'B'}}^{\text{init}} = -1$ and $p_{\text{sys 'B'}}^{\text{init}} = 5$). Inset: A cartoon of initial system and bath states.
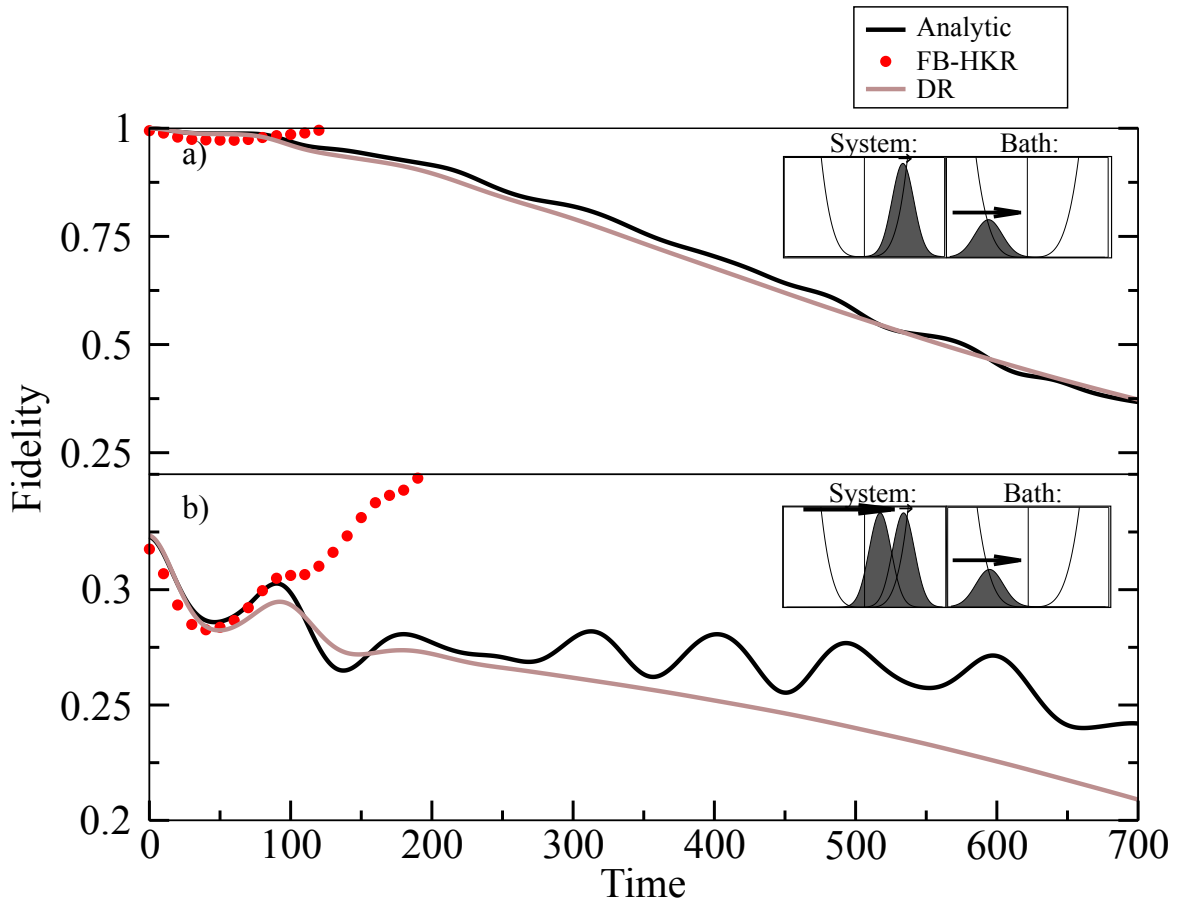
Figure 8.4: Initial state for the system and bath quartic oscillators are Gaussians coupled biquadratically ($\epsilon q_{\text{sys}}^2 q_{\text{bath}}^2$) with parameters $\epsilon = 2, \hbar = 1$, $\Delta t = 0.01$, $t = 700\Delta t$, $m_{\text{sys}} = 3$, $m_{\text{bath}} = 1$, $\omega_{\text{sys}} = 4.5$, $\omega_{\text{bath}} = 1.4$, $\sigma_{\text{sys}} = 0.2$ and $\sigma_{\text{bath}} = 0.5$ where a) shows "diagonal fidelity" ($q_{\text{sys}}^{\text{init}} = 0.5$, $p_{\text{sys}}^{\text{init}} = 0.1$, $q_{\text{bath}}^{\text{init}} = -1$ and $p_{\text{bath}}^{\text{init}} = 0.5$) and b) shows "off-diagonal fidelity" ($q_{\text{sys 'B'}}^{\text{init}} = 0.2$ and $p_{\text{sys 'B'}}^{\text{init}} = 0.6$). Inset: A cartoon of initial system and bath states.

calculations if the fidelity decay is slow or rephases. In particular, similar to the findings reported in many studies of the FBSD[69] and LSC-IVR[64], the DR performs well when the overall decay in fidelity is faster than its ability to include effects such as quantum coherence, and poor when this overall decay is slower. This is especially true in systems with many degrees of freedom where the prevalence and importance of rephasing is small.

8.3.2 Many Dimensional System: Caldeira-Leggett

To study the DRs scaling with dimensionality, the fidelity of a Caldeira-Leggett Hamiltonian[70] for I_2[71, 72, 73] was studied. This involved modelling one degree of freedom of the molecule, anharmonic stretching, through a Morse potential coupled to a harmonic oscillator (HO) bath. The Hamiltonian was,

$$
\begin{aligned}
H \;=\; & \frac{p^2}{2\mu} + D\left[1 - e^{-\alpha(q-q_e)}\right]^2 \\
& + \sum_{j=1}^{f-1}\left[\frac{P_j^2}{2} + \frac{\omega_j^2}{2}\left(Q_j + \frac{c_j}{\omega_j^2}(q - q_e)\right)^2\right]
\end{aligned}
\tag{8.10}
$$

with $D = 1.2547 \times 10^4$ cm^{-1}, $q_e = 2.6663$ Å, $\alpha = 1.8576$ Å^{-1} and μ equal to the reduced mass of I_2. The sum runs over the $(f-1)$ HOs in the bath.

Coupling to the bath was chosen to be dictated by the Ohmic spectrum (hereafter $\hbar = 1$),

$$
J(\omega) = \eta_{\text{sb}}\omega e^{-\frac{\omega}{\omega_c}},
\tag{8.11}
$$

where

$$
\omega_j = -\omega_c \ln\left[1 - \frac{j}{f-1}\left(1 - e^{-5}\right)\right]
\tag{8.12}
$$

are the individual HO frequencies and,

$$
c_j = \omega_j\sqrt{\frac{2\eta_{\text{sb}}\omega_c}{\pi(f-1)}(1 - e^{-5})}
\tag{8.13}
$$

are their corresponding coupling constants (otherwise equal to zero during forward time evolution). $\eta_{sb} = 0.25 \times 213.7\mu$ cm^{-1} is the system-bath coupling coefficient and $\omega_c = 20$ cm^{-1} is the characteristic bath frequency. Expressed in terms of the coherent state basis used in the FB-HKR,

$$\langle q \,|q_i, p_i \rangle = \left(\frac{\gamma}{\pi}\right)^{\frac{1}{4}} \exp\left[-\frac{\gamma}{2}(q - q_i)^2 + ip_i(q - q_i)\right], \tag{8.14}$$

(where γ is the width of the coherent state basis), the initial state of the Morse oscillator was selected to be in its ground state,

$$\begin{aligned} \Psi_{sys}(q, p) &= \exp\left[-\frac{\gamma}{4}(q - q_i)^2 - \frac{1}{4\gamma}(p - p_i)^2 \right. \\ &\quad \left. +\frac{i}{2}(p + p_i)(q - q_i)\right] \end{aligned} \tag{8.15}$$

with $q_i = 2.4$ Å (just to the left of the potential minimum), $p_i = 0.0$, and $\gamma = \sqrt{2D\mu a^2} \equiv \mu\Omega_s$, where $\Omega_s = 213.7$ cm^{-1} is the harmonic frequency of the Morse oscillator. The HO bath began as a thermalized state $\frac{e^{-\beta \hat{H}_B}}{Q_B}$ at 300 K[72],

$$\begin{aligned} \Psi_{bath} &(Q_j, P_j, Q'_j, P'_j) \\ &= (1 - e^{-\beta\omega_j}) \\ &\quad \times \exp\left\{ -\frac{\Gamma_j}{4}(Q_j^2 + Q'^2_j) - \frac{1}{4\Gamma_j}(P_j^2 + P'^2_j) \right. \\ &\quad +\frac{i}{2}(P_jQ_j - P'_jQ'_j) + \frac{1}{2}e^{-\beta\omega_j}\left[\Gamma_j Q_j Q'_j \right. \\ &\quad \left. \left. +\frac{1}{\Gamma_j}P_jP'_j + i(P'_jQ_j - P_jQ'_j)\right] \right\}. \end{aligned} \tag{8.16}$$

with $\gamma = \Gamma_j = \omega_j$ (where j is the HO bath index).

Figure 8.5 shows how the DR fares compared to FB-HKR with one to fifty HOs in the bath, though the latter method was only calculated with up to ten HOs. It has been shown that a minimum of twenty HOs are necessary to reproduce the Ohmic spectrum[72]. The DR-calculated
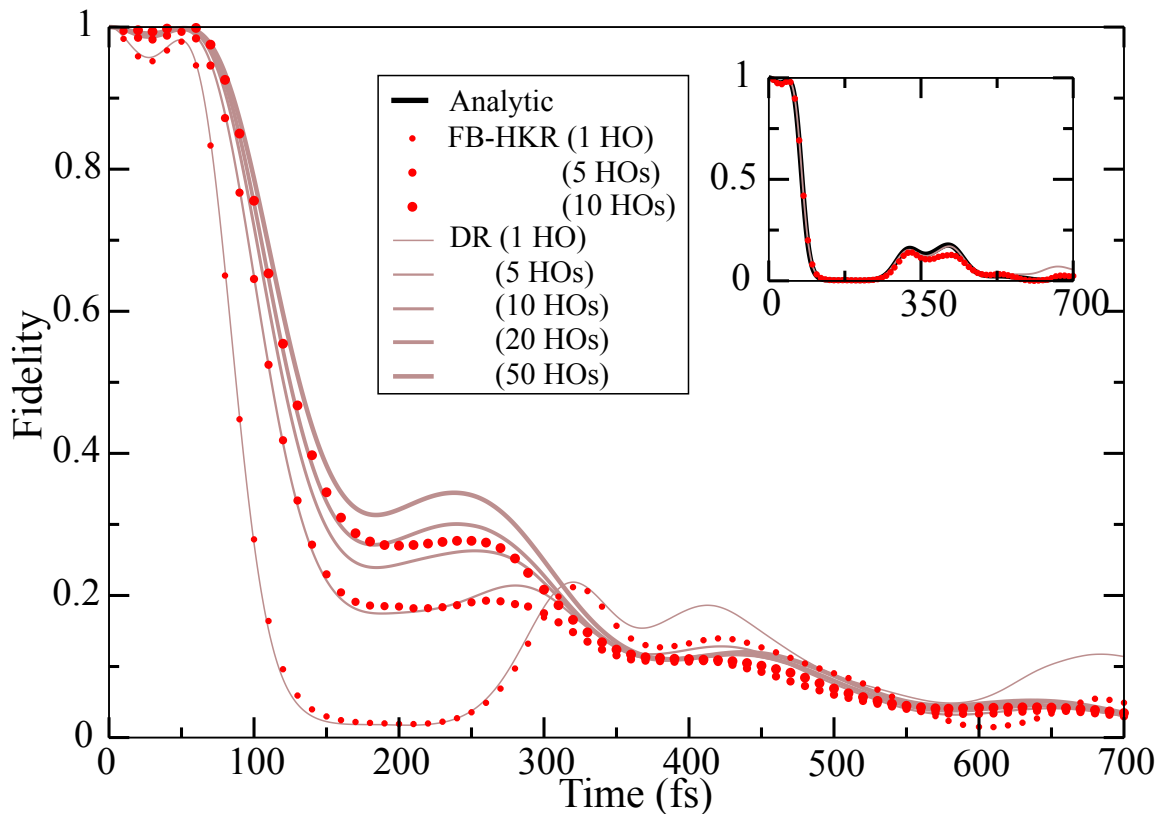
Figure 8.5: Calculation of the fidelity of a Morse oscillator (parametrized to fit a diiodide bond) coupled to a thermalized bath of various numbers of harmonic oscillators at 300 K via Ohmic coupling performed using the DR and FB-HKR. Inset: The same set-up but with only 1 HO in the bath in an excited pure state allowing for the calculation of an analytical numerical solution. It is likely the analytical solution is similar in the case of the thermalized bath and so is in comparable agreement with the DR and FB-HKR.

fidelity shows convergence at a similar number of HOs. Impressively, the DR exhibited superior computational scaling compared to the prefactor-laden FB-HKR.

8.4 Dephasing relation propagator

The DR can be implemented in the semiclassical propagation of any quantum state Ψ under the Hamiltonian H in the following general manner:

$$\langle \boldsymbol{q} | \Psi(t) \rangle = \langle \boldsymbol{q} | e^{-iHt/\hbar} | \Psi(0) \rangle \tag{8.17}$$

$$= \int d\boldsymbol{q}' \, \langle \boldsymbol{q} | e^{-iHt/\hbar} e^{iH^0 t/\hbar} | \boldsymbol{q}' \rangle \tag{8.18}$$

$$\times \langle \boldsymbol{q}' | e^{-iH^0 t/\hbar} | \Psi(0) \rangle$$

$$\approx \int d\boldsymbol{q}' \left(O_{\text{DR}}^{H^0, H}(\boldsymbol{q}, \boldsymbol{q}', t) \right)^* \langle \boldsymbol{q}' | e^{-iH^0 t/\hbar} | \Psi(0) \rangle . \tag{8.19}$$

The quantum propagator is split into two terms by the introduction of another Hamiltonian, H^0: a fidelity term and another term governed by free evolution under H^0. In Eq. 8.17 an identity operator is inserted producing a fidelity term in Eq. 8.18 that is subsequently simplified by substituting in the generalized DR. In particular, the left term in Eq. 8.19 is the complex conjugate of the position state representation of the DR for the forward Hamiltonian H and the backward Hamiltonian H^0. Without loss of generality, it is helpful as before to let

$$H \equiv H^0 + \epsilon V. \tag{8.20}$$

Expressed this way, it is clear that H^0 must be chosen wisely so that the DR term can be accurate. Furthermore, it is preferable to choose an H^0 such that the free evolution term can be calculated as easily as the DR-containing term. This can often be accomplished in weakly interacting many-body systems by letting H^0 be the Hamiltonian including only free-particle terms while ϵ governs the strength of V, the interparticle interactions. In such applications, the splitting introduced in Eq. 8.18 is similar, though not the same, as that introduced by the "interaction" representation.

This idea can be illustrated by considering the Hamiltonian,

$$H = \frac{1}{2}p^2 + \frac{1}{2}\omega^2 q^2 - aq^3 + bq^4 \tag{8.21}$$

with $\omega = \sqrt{2}$ and $a = b = 0.1$. This is a strongly anharmonic oscillator system that has often been used before to test the limitations of other Wigner-type linearized approximations[74, 75, 69, 64, 65, 60].

Figure 8.6 shows the average position of an initially shifted ground state with time. Most Wigner-type linearized approximations and FBSD decay to small oscillations by the 300 timestep mark[60]. Setting H^0 from Eq. 8.19 to be equal to $\frac{1}{2}p^2 + \frac{1}{2}\omega'^2 q^2$ simplifies the free-evolution term to the analytically solvable Feynman propagator for an HO. When $\omega' = \omega$ the DR-calculated average position is relatively poor in Figure 8.6a compared to the analytic result. This is because the anharmonic terms in the potential produce an initial effective frequency of oscillation that is faster than the harmonic frequency ω for the initial state. In other words, the free evolution term of Eq. 8.19 produces a curve with frequency ω that the DR term of the equation is unable to "dephase" effectively enough into the proper frequency. Increasing ω' to $1.05 \, \omega$ and $1.1 \, \omega$ reduces the work that the DR must do to "dephase" the free evolution term and produces better results, as demonstrated in Figs. 8.6b and c. Notice that even in the worst example of the DRs performance shown in Figure 8.6a, the DR propagator far outperforms other prefactorless semiclassical propagators since it is still oscillating after 300 timesteps (although the frequency of this oscillation is incorrect).

Using Eq. 8.20 as a building block, it is possible to generate DR-based propagation schemes for many general expressions of interest. For instance, the expression for the purity of a system, a
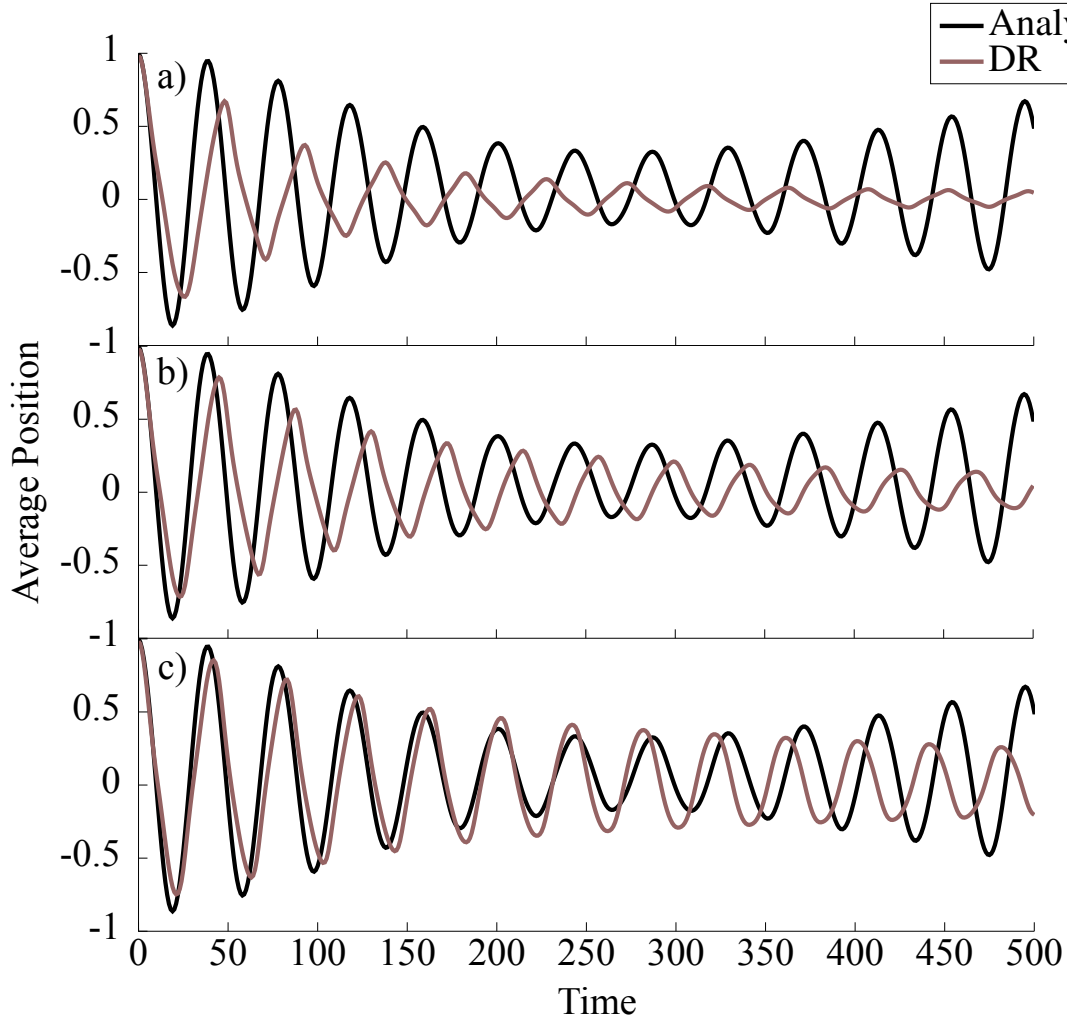
Figure 8.6: Average position plotted versus time of a displaced wavepacket oscillating under the highly anharmonic Hamiltonian $H = \frac{1}{2}p^2 + \frac{1}{2}\omega^2 q^2 - 0.1q^3 + 0.1q^4$ with $\omega = \sqrt{2}$. The DR curves where calculated from the expression $\int d\boldsymbol{x}' \left(O_{\mathrm{DR}}^{H^0,H}(\boldsymbol{q},\boldsymbol{q}',t) \right)^* \langle \boldsymbol{q}' | e^{-iH^0 t/\hbar} |\Psi(0)\rangle$ where $H^0 = \frac{1}{2}p^2 + \frac{1}{2}\omega'^2 q^2$ with a) $\omega' = \omega$, b) $\omega' = 1.05\,\omega$ and c) $\omega' = 1.1\,\omega$.

measure of decoherence from system-bath interaction, can be expressed as,

$$
\begin{aligned}
&\mathrm{Tr}(\rho_s^2) \\
&= \int d\boldsymbol{q}_s \int d\boldsymbol{q}_s' \int d\boldsymbol{q}_b \int d\boldsymbol{q}_b' \\
&\quad \int d\boldsymbol{q}_{os} \int d\boldsymbol{q}_{os}' \int d\boldsymbol{q}_{ob} \int d\boldsymbol{q}_{ob}' \\
&\quad \int d\boldsymbol{q}_{os}'' \int d\boldsymbol{q}_{os}''' \int d\boldsymbol{q}_{ob}'' \int d\boldsymbol{q}_{ob}''' \\
&\quad \times \langle \boldsymbol{q}_s \boldsymbol{q}_b | e^{-iHt/\hbar} e^{iH^0 t/\hbar} | \boldsymbol{q}_{os} \boldsymbol{q}_{ob} \rangle \\
&\quad \times \langle \boldsymbol{q}_{os}' \boldsymbol{q}_{ob}' | e^{-iH^0 t/\hbar} e^{iHt/\hbar} | \boldsymbol{q}_s' \boldsymbol{q}_b \rangle \\
&\quad \times \langle \boldsymbol{q}_s' \boldsymbol{q}_b' | e^{-iHt/\hbar} e^{iH^0 t/\hbar} | \boldsymbol{q}_{os}'' \boldsymbol{q}_{ob}'' \rangle \\
&\quad \times \langle \boldsymbol{q}_{os}''' \boldsymbol{q}_{ob}''' | e^{-iH^0 t/\hbar} e^{iHt/\hbar} | \boldsymbol{q}_s \boldsymbol{q}_b' \rangle \\
&\quad \times \rho^0(\boldsymbol{q}_{os}, \boldsymbol{q}_{ob}, \boldsymbol{q}_{os}', \boldsymbol{q}_{ob}', t) \\
&\quad \times \rho^0(\boldsymbol{q}_{os}'', \boldsymbol{q}_{ob}'', \boldsymbol{q}_{os}''', \boldsymbol{q}_{ob}''', t)
\end{aligned}
\tag{8.22}
$$

where $\boldsymbol{q}_s$, $\boldsymbol{q}_s'$, $\boldsymbol{q}_{os}$, $\boldsymbol{q}_{os}'$, $\boldsymbol{q}_{os}''$ and $\boldsymbol{q}_{os}'''$ are system phase space coordinates, $\boldsymbol{q}_b$, $\boldsymbol{q}_b'$, $\boldsymbol{q}_{ob}$, $\boldsymbol{q}_{ob}'$, $\boldsymbol{q}_{ob}''$ and $\boldsymbol{q}_{ob}'''$ are bath phase space coordinates, H is the full Hamiltonian, H^0 is the same Hamiltonian with the system-bath interactions turned off, and ρ^0 is the full time-dependant density matrix with interactions turned off (usually this is simple to calculate).

Applying such a splitting scheme using an ancillary Hamiltonian H^0 will always result in an integral with a "kernel", such as the terms with ρ^0 above, alongside expressions of fidelity that can be approximated with the DR. Again, this means that it is prudent to choose H^0 such that this procedure produces an easily computed and accurate kernel while allowing for the smallest effective perturbation for the DR to deal with.

8.5 Conclusion

In this chapter we extended the DR for fidelity to treat "off-diagonal" elements. Its performance was examined with integrable and chaotic systems that were perturbatively coupled to a bath with few to many degrees of freedom. In general, the DR was found to be surprisingly accurate and efficient.

Subsequently, a particular approach to using the DR as a semiclassical propagator for quantum states was introduced. By exploiting the DRs unique efficiency and accuracy, this methodology demonstrated the potential to be superior to many previous linearization methods, such as FBSD and LSC-IVR, granted that perturbative splitting with an ancillary Hamiltonian is possible. Particularly attractive is the DR propagator's ability to include quantum correlation effects. A simple calculation of the evolution of the average position of a wavepacket in a heavily anharmonic potential using the DR-based propagator was shown to produce better results.

The DR-based propagator has many promising applications, including serving as a more physically intuitive approach for calculating the purity of many-dimensional system-baths compared to the traditional master equation approach. Its derivation is vastly different from other linearized methods and its effectiveness as a quick and cheap tool for semiclassical propagation deserves evaluation.

8.6 Appendix

8.6.1 Forward-Backward Fidelity

Consider the two exponential operators in Eq. 8.1 as the single unitary operator $\hat{U} \equiv e^{\frac{iH^\epsilon t}{\hbar}} e^{-\frac{iH^0 t}{\hbar}}$ which is the time evolution via the time-dependent Hamiltonian,

$$\hat{H}(t) = \begin{cases} \hat{H}^0 & 0 \to t \\ \hat{H}^\epsilon & t \to 0. \end{cases} \tag{8.23}$$

A position basis representation for $\hat{U}(\boldsymbol{q}, \boldsymbol{q}')$,

$$
\begin{aligned}
&\langle \boldsymbol{q}' | \hat{U} | \boldsymbol{q} \rangle \\
&= \int d\boldsymbol{q}'' \langle \boldsymbol{q}' | e^{i\hat{H}^\epsilon t/\hbar} | \boldsymbol{q}'' \rangle \langle \boldsymbol{q}'' | e^{-i\hat{H}^0 t/\hbar} | \boldsymbol{q} \rangle && (8.24) \\
&\approx \int d\boldsymbol{q}'' e^{iS(\boldsymbol{q}', \boldsymbol{q}''; 0 \to t)/\hbar} e^{iS(\boldsymbol{q}'', \boldsymbol{q}; t \to 0)/\hbar} && (8.25)
\end{aligned}
$$

where the integral over $\boldsymbol{q}''$ was evaluated by the SPA in the second line and preexponential factors in this "primitive" semiclassical propagator were disregarded. The SPA condition for this integral is,

$$
\begin{aligned}
\frac{\partial S(\boldsymbol{q}', \boldsymbol{q}''; 0 \to t)}{\partial \boldsymbol{q}''} &= \frac{\partial S(\boldsymbol{q}'', \boldsymbol{q}; t \to 0)}{\partial \boldsymbol{q}''} && (8.26) \\
\boldsymbol{p}_t(\boldsymbol{q}', \boldsymbol{q}'') &= \boldsymbol{p}_t(\boldsymbol{q}'', \boldsymbol{q}) && (8.27)
\end{aligned}
$$

where the left hand side of the final expression is the momentum at time t after going forward in time and the right hand side is the momentum at time t before going backward in time. The same is manifestly true in this representation for the position at time t after going forward in time and before going backward in time since $\boldsymbol{q}_t \equiv \boldsymbol{q}''$.

Moreover, the overall phase is provided in this stationary phase approximated propagator and is equal to $e^{iS(\boldsymbol{q}', \boldsymbol{q})/\hbar}$ where

$$
S(\boldsymbol{q}', \boldsymbol{q}) = S(\boldsymbol{q_t}, \boldsymbol{q}; 0 \to t) + S(\boldsymbol{q}', \boldsymbol{q_t}; 0 \to t). \tag{8.28}
$$

Time-dependent Hamiltonians have the same HHKK propagator as their time-independent brethren and so Eq. 8.8 can be rewritten without one of its double phase space integrals as Eq. 8.9.

9 Graphene's Raman Spectrum

9.1 Introduction to Graphene

Graphene is a material that has proved to be a boon for study in the condensed matter community. Herein, we will focus on its unique electronic and vibrational properties that explain its novel Raman spectrum.

9.2 Graphene Lattice

Following Misra's *Physics of Condensed Matter*[76], graphene is a lattice of carbon atoms arranged in a hexagonal lattice such that every carbon has three nearest neighbors a distance $a = 1.42$ Å apart. The unit cell of graphene can be described as made up of two atoms, A and B, with the two lattice vectors $a_1 = \frac{3a}{2}\left(1, \frac{1}{\sqrt{3}}\right)$ and $a_2 = \frac{3a}{2}\left(1, -\frac{1}{\sqrt{3}}\right)$. These have corresponding reciprocal lattice vectors $b_1 = 2\pi\frac{a_2}{a_1 \cdot a_2} = \frac{2\pi}{3a}\left(1, \sqrt{3}\right)$ and $b_2 = 2\pi\frac{a_1}{a_2 \cdot a_1} = \frac{2\pi}{3a}\left(1, -\sqrt{3}\right)$.

The three nearest neighbors are $\delta_1 = \frac{a}{2}\left(1, \sqrt{3}\right)$, $\delta_2 = \frac{a}{2}\left(1, -\sqrt{3}\right)$, and $-a\left(1, 0\right)$ and the next nearest neighbors are at $\delta_1^{\pm} = a_1$, $\delta_2^{\pm} = \pm a_2$ and $\delta_3^{\pm} = \pm(a_2 - a_1)$.

9.2.1 Graphene's Electronic Dispersion

Graphene's electronic dispersion is shown in Figure 9.2.
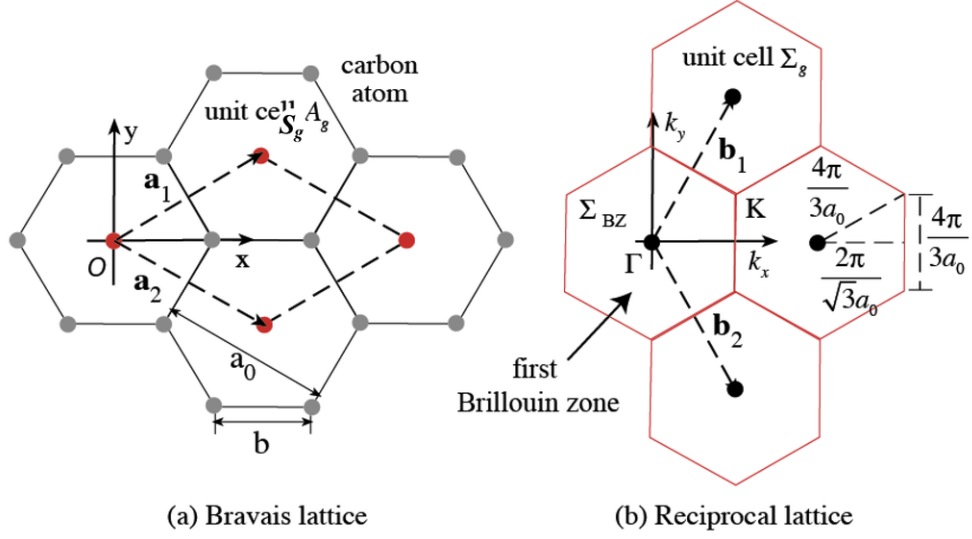
Figure 9.1:

This can be described by a tight-binding Hamiltonian[77] (using an orthonormalized π-orbital basis set):

$$H_{\vec{k}} = \begin{pmatrix} g(\vec{k}) & f(\vec{k}) \\ f^*(\vec{k}) & g(\vec{k}) \end{pmatrix},$$

(9.1)

where

$$f(\vec{k}) = t_1 \sum_{i=1,3} e^{i\vec{k}\cdot\vec{C}_i^1} + t_3 \sum_{i=1,3} e^{i\vec{k}\cdot\vec{C}_i^3} + t_4 \sum_{i=1,6} e^{i\vec{k}\cdot\vec{C}_i^4},$$

(9.2)

and

$$g(\vec{k}) = t_2 \sum_{i=1,6} e^{i\vec{k}\cdot\vec{C}_i^2} + t_5 \sum_{i=1,6} e^{i\vec{k}\cdot\vec{C}_i^5} = g^*(\vec{k}).$$

(9.3)

C^i corresponds to the ith nearest neighbors and t_i is the corresponding hopping parameter.

The eigenvectors of this matrix can be shown to be:

$$e_{\vec{k}}^{\pi^*} = g(\vec{k}) + |f(\vec{k})| \quad , \quad a_{\vec{k}}^{\pi^*} = \frac{1}{\sqrt{2}} \begin{pmatrix} 1 \\ \phi(\vec{k}) \end{pmatrix},$$

(9.4)

$$e_{\vec{k}}^{\pi} = g(\vec{k}) - |f(\vec{k})| \quad , \quad a_{\vec{k}}^{\pi} = \frac{1}{\sqrt{2}} \begin{pmatrix} 1 \\ -\phi(\vec{k}) \end{pmatrix},$$

(9.5)

106
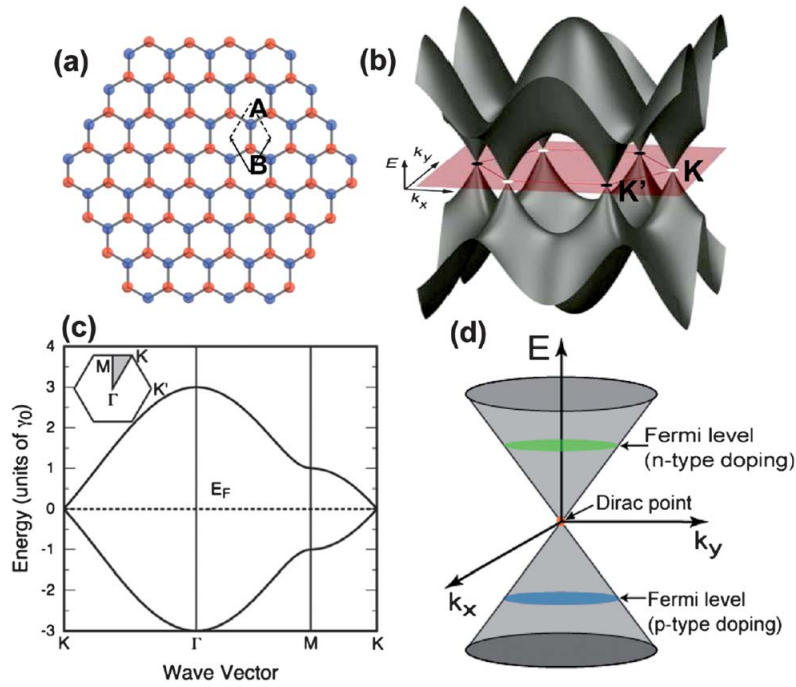
Figure 9.2: From [78].

where $\phi(\vec{k}) = \frac{f^*(\vec{k})}{|f(\vec{k})|}$.

9.2.2 Graphene's Phonon Dispersion

Graphene's phonon dispersion is shown in Figure 9.3. It can also be calculated by tight-binding, as many have done. We will rely on the method by [79]. Its most important modes are the zig-zag (G) modes and breathing (D) modes, which are shown in Figure 9.3b.
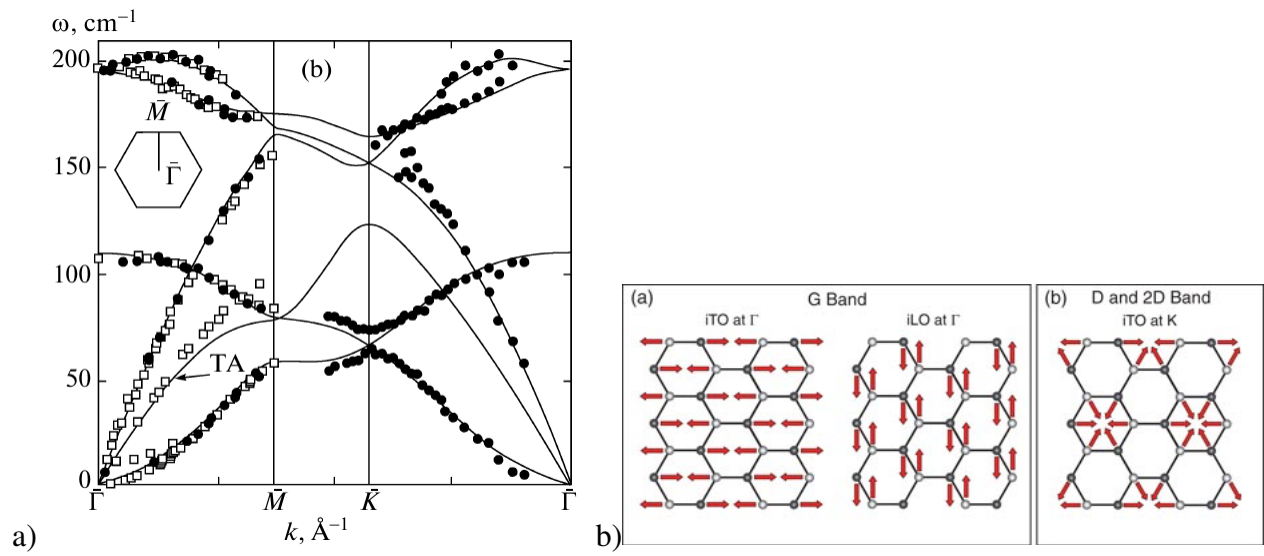
Figure 9.3: a) From [80]. b) From an unknown source.

9.3 Introduction to Raman Spectroscopy

Raman spectroscopy is a very useful and important two-photon spectroscopy. Normal absorption spectroscopy occurs in the I.R. region and corresponds to a one-photon process. Absorption occurs when the incident laser energy approaches that of a vibrational excitation. Raman spectroscopy, on the other hand, involves both incident light that excites electrons to intermediate virtual states (in non-resonant Raman) or excited electronic states (in resonant Raman) as well as emitted light when the electron relaxes back to its initial electronic state. If the final state is vibrationally excited compared to its initial state, the spectrum exhibits a Raman peak. If not, a Rayleigh peak is seen. Since it is always more common for this two-photon process to excite no vibrational degrees of freedom (as they do not depend on vibrational or phonon density of states), the latter Rayleigh peak is always far more intense than any Raman peak.

Raman peaks are usually symmetrically produced around the Rayleigh peak. One side corresponds to two-photon processes that relax vibrational modes, while the other corresponds to those that excite vibrational modes. The former is known as a Stokes process while the latter is anti-Stokes. Figure 9.4 sketches these different processes.

IR absorption peaks correspond to the excitation of modes whose dipole moment changes, while Raman peaks correspond to vibrational modes whose polarization changes. The reason for this can be seen in their scattering cross-sections: the former depends on the dipole moment between the initial and final state while the latter depends on the dipole moment between initial and intermediate states, and intermediate states and the final state. This will be shown presently.

9.4 Absorption and Emission Cross-Sections

The absorption and stimulated emission cross-sections can be shown[1] to be linearly dependent on ω_I and cubically dependent on ω_S respectively. The latter is due to the fact that stimulated emission
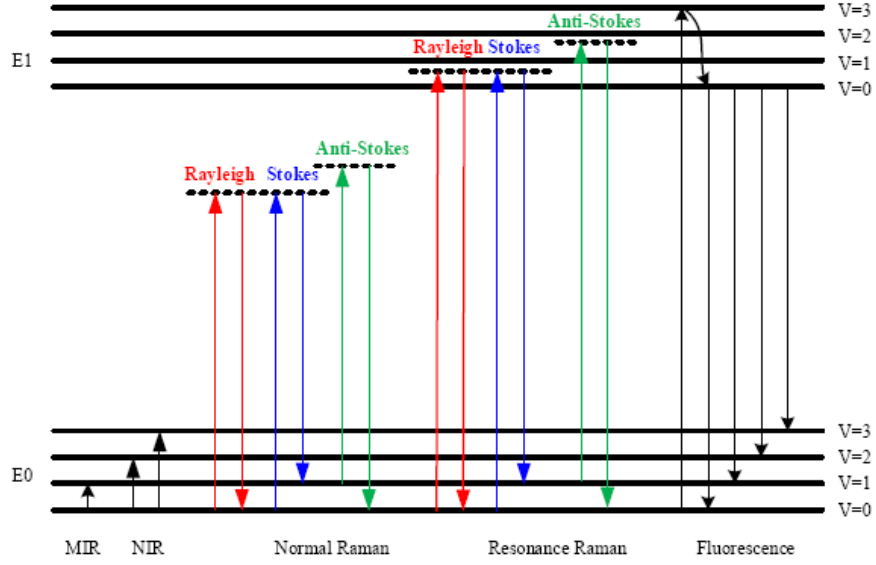
Figure 9.4: From [81].

depends on the free photon density. The absorption cross-section is:

$$\Sigma^{\rho}_{i\rightarrow n} = \frac{2\pi e \omega_I}{3hc} \sum_n |\alpha^{\rho}_{i,n}|^2,$$ (9.6)

where

$$\alpha^{\sigma}_{i,n} = \langle i| \boldsymbol{D}^{\dagger,\sigma} |n\rangle .$$ (9.7)

The emission cross-section is:

$$\Sigma^{\sigma}_{n\rightarrow f} = \frac{2\pi e^3 \omega_S^3}{hc^3} \sum_n |\alpha^{\sigma}_{n,f}|^2,$$ (9.8)

where

$$\alpha^{\sigma}_{n,f} = \langle f| \boldsymbol{D}^{\dagger,\sigma} |n\rangle .$$ (9.9)
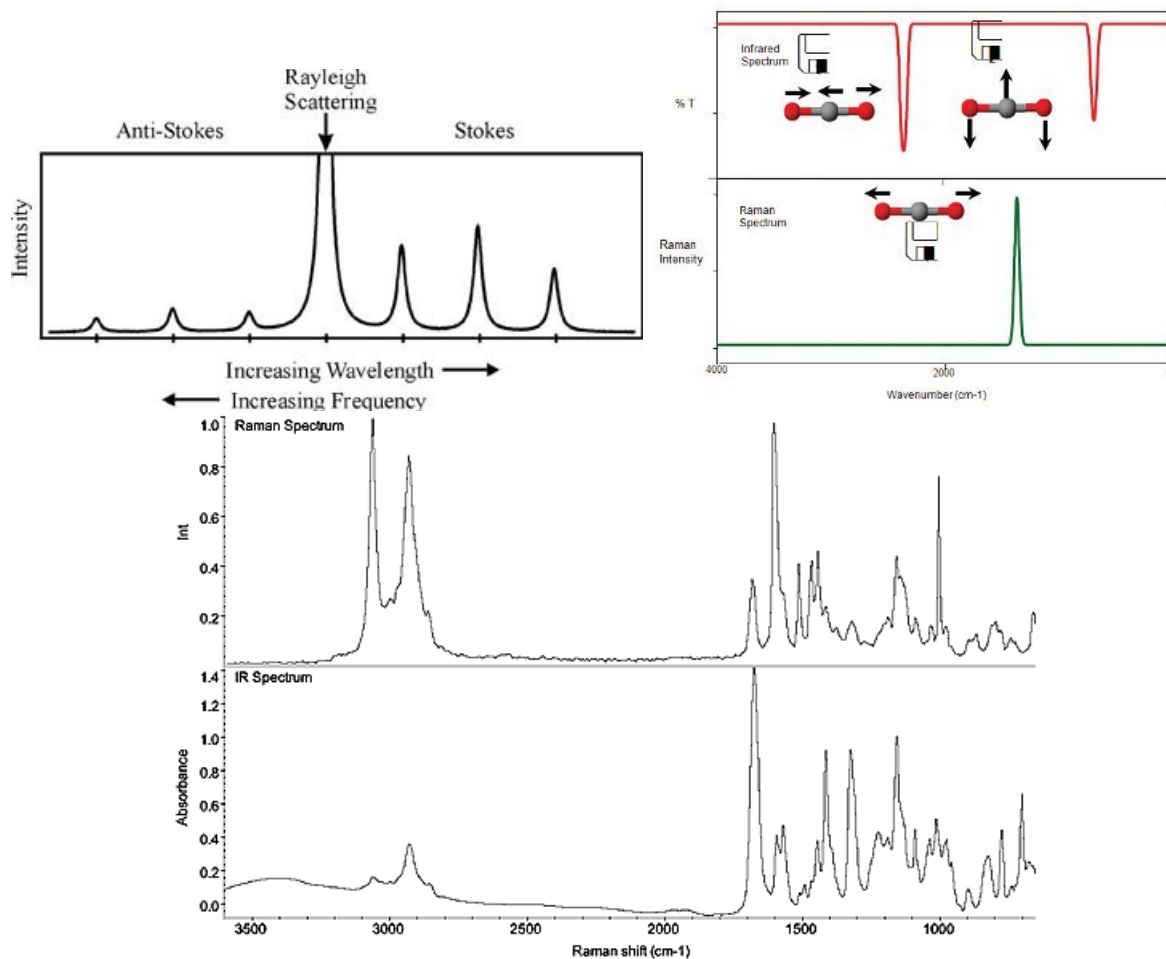
Figure 9.5: First figure from [82]. Second panel taken from [83]. Third from [84]

9.5 Graphene's Absorption Spectrum

Before we get to the Raman spectrum of graphene, let us briefly discuss its simpler absorption spectrum. Due to its periodicity and the Dirac cone crossing its Fermi energy, graphene differs from finite molecule samples' absorption spectra in that every laser energy is on scale with electronic transitions; every process is resonant. The experimentally observed spectrum is shown in Figure 9.6.
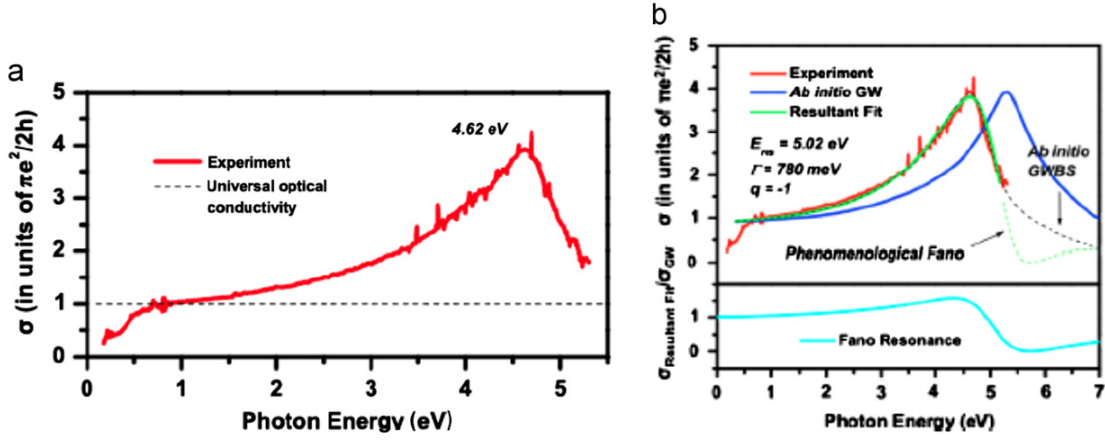
Figure 9.6: From [85].

The amplitude of graphene's absorption can be simplified by using the Hellman-Feynman identity to:

$$\sigma \propto \int d\vec{k} \left| \frac{e\vec{P} \cdot \left[(a_{\vec{k}}^{\pi*})^\dagger \vec{\nabla} H(\vec{k})(a_{\vec{k}}^{\pi}) \right]}{\epsilon_L} \right|^2 \rho, \tag{9.10}$$

9.5.1 Absorbance without Phonon Production

Within tight-binding, phononless absorption can be approximated by[77]:

$$\sigma \ \propto \ |\langle \vec{k}, \pi^* | \vec{D} | \vec{k}\pi \rangle|^2 \rho \tag{9.11}$$

$$= \ \int d\vec{k} \left| \frac{e\vec{P} \cdot \left[(a_{\vec{k}}^{\pi*})^\dagger \vec{\nabla} H(\vec{k})(a_{\vec{k}}^{\pi}) \right]}{\epsilon_L} \right|^2 \rho, \tag{9.12}$$

where $a_{\vec{k}}^{\pi/\pi^*}$ are the eigenvectors of the electronic T.B. Hamiltonian $H(\vec{k})$ and $\vec{P}$ is the polarization of the incident laser with energy ϵ_L.

The absorption spectrum from this formula is shown in Figure 9.7 and agrees qualitatively with the experimentally observed spectrum in Figure 9.6.
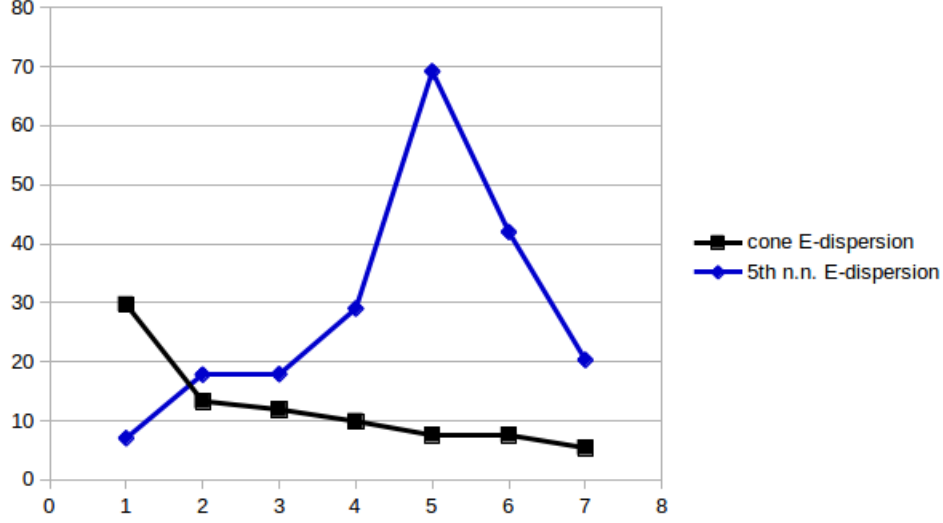
Figure 9.7: Rough tight-binding calculation of graphene absorption spectrum. The black curve corresponds to the unit universal optical conductivity due to the linear dispersion of the cone. The blue line actually takes into account the electronic dispersion of graphene to determine all phononless transitions using Eq. 9.12. We attribute the deviation from the black line from a constant line, especially at low energies, to insufficient k-space points close to the Dirac cone.

9.5.2 Absorbance with Phonon Production

Similarly, within tight-binding phonon-assisted absorption can be approximated by[77]:

$$
\frac{\partial \mu}{\partial \xi} \approx \left\langle \vec{k} + \vec{q}, \pi^* \left| \frac{\partial \vec{D}}{\partial \vec{\xi}_{\vec{q}}} \right| \vec{k}\pi \right\rangle \tag{9.13}
$$

$$
= \sqrt{\frac{\hbar}{2M\omega_{\vec{q},\nu}}} e\vec{P} \cdot \left[\sum_{s,c} \epsilon_{\vec{q},\nu}^{s,c} \left(a_{\vec{k}+\vec{q}}^{\pi^*} \right)^\dagger \left(\frac{\partial \Delta H_{\vec{k}+\vec{q},\vec{k}}^{s,c}}{\partial \vec{k}} \right) \left(a_{\vec{k}}^{\pi} \right) \right] \tag{9.14}
$$

where

$$
\frac{\partial \Delta H_{\vec{k}+\vec{q},\vec{k}}^{1,c}}{\partial \vec{k}} = \sqrt{3}\eta_1 \begin{pmatrix} 0 & \dot{h}_c(\vec{k}) \\ \dot{h}_c(\vec{k}+\vec{q}) & 0 \end{pmatrix}, \tag{9.15}
$$

$$
\frac{\partial \Delta H_{\vec{k}+\vec{q},\vec{k}}^{2,c}}{\partial \vec{k}} = -\sqrt{3}\eta_1 \begin{pmatrix} 0 & \dot{h}_c(\vec{k}+\vec{q}) \\ \dot{h}_c(\vec{k}) & 0 \end{pmatrix}, \tag{9.16}
$$

113

and

$$
\dot{h}_c(\vec{k}) = \begin{pmatrix} \sum_{i=1}^{3} iC_{i,x}^1 e^{i\vec{k}\cdot\vec{C}_i^1} \frac{C_{i,c}}{a_0} \\ \sum_{i=1}^{3} iC_{i,y}^1 e^{i\vec{k}\cdot\vec{C}_i^1} \frac{C_{i,c}}{a_0} \\ \sum_{i=1}^{3} iC_{i,z}^1 e^{i\vec{k}\cdot\vec{C}_i^1} \frac{C_{i,c}}{a_0} \end{pmatrix}. \tag{9.17}
$$

9.6   Raman Cross-Section: KHD

The K.H.D. formalism is simply second-order perturbation theory on the Born-Oppenheimer states with respect to light-matter interaction. The total Raman cross-section for incident light with energy ω_I, stimulated emission with energy ω_S is:

$$
\Sigma_{i\to f}^{\rho,\sigma} = \frac{8\pi e^4 \omega_S^3 \omega_I}{9c^4} |\alpha_{i,f}^{\rho,\sigma}|^2. \tag{9.18}
$$

Notice that it is rather close to an amalgamation of the cross-sections for absorption and stimulated emission, which is what Raman spectroscopy is.

The differential amplitude

$$
\alpha_{i,f}^{\rho,\sigma} = \frac{1}{\hbar} \sum_n \left[\frac{\langle f| \boldsymbol{D}^{\dagger,\sigma} |n\rangle \langle n| \boldsymbol{D}^\rho |i\rangle}{E_i - E_n + \hbar\omega_I - i\Gamma_n} + \frac{\langle f| \boldsymbol{D}^{\dagger,\sigma} |n\rangle \langle n| \boldsymbol{D}^\rho |i\rangle}{E_i + E_n + \hbar\omega_I + i\Gamma_n} \right]. \tag{9.19}
$$

E_i is the energy of the initial state i with decay Γ_n, E_n is the energy of the intermediate state n with decay Γ_n. $\boldsymbol{D}^\sigma$ is the dipole moment $\propto E\boldsymbol{r}^\sigma$.

Making this more explicit in terms of phonons and electrons, we let the phonon coordinates be $\boldsymbol{\xi}$ and electron coordinates be $\boldsymbol{r}$ and define:

$$
\begin{align}
|i\rangle &= \left|\psi_{m_i}^{\text{B.O}}(\boldsymbol{\xi},\boldsymbol{r})\right\rangle = |\chi(\boldsymbol{r};\boldsymbol{\xi})\rangle |\phi_{m_i}(\boldsymbol{\xi})\rangle, \tag{9.20} \\
|n\rangle &= \left|\psi_{q_v,q_c,m}^{\text{B.O}}(\boldsymbol{r},\boldsymbol{\xi})\right\rangle = |\chi_{q_v,q_c}(\boldsymbol{r};\boldsymbol{\xi})\rangle |\phi_{m_{vc}}(\boldsymbol{\xi})\rangle, \text{ and} \tag{9.21} \\
|f\rangle &= \left|\psi_{m_f}^{\text{B.O}}(\boldsymbol{\xi},\boldsymbol{r})\right\rangle = |\chi(\boldsymbol{r};\boldsymbol{\xi})\rangle |\phi_{m_f}(\boldsymbol{\xi})\rangle. \tag{9.22}
\end{align}
$$

The initial state $|i\rangle$ consists of a sea of electrons, but we focus on the momentum m_i of one in particular. The intermediate state $|n\rangle$ is characterized by an electron with momentum $q_v - q_c$ and

(for simplicity, considering only a one-phonon-per-transition process) an excited or relaxed phonon with momentum m_{vc}. Finally, the final state consists of the Fermi sea of electrons and excited (or relaxed) phonons with momenta m_f.

For a review of the Born-Oppenheimer approximation, see the Appendix.

9.6.1 The Transition Moment Operator

We rewrite

$$\langle n| \, \boldsymbol{D}^\rho \, |i\rangle = \langle \phi_{m_{vc}}(\boldsymbol{\xi})| \, \langle \chi_{q_v,q_c}(\boldsymbol{r};\boldsymbol{\xi})| \, D^\rho \, |\chi(\boldsymbol{r};\boldsymbol{\xi})\rangle \, |\phi_m(\boldsymbol{\xi})\rangle \tag{9.23}$$

as

$$\langle n| \, \boldsymbol{D}^\rho \, |i\rangle = \langle \phi_{m_{vc}}(\boldsymbol{\xi})| \, \mu^\rho_{q_c,q_v}(\boldsymbol{\xi}) \, |\phi_m(\boldsymbol{\xi})\rangle \tag{9.24}$$

with

$$\mu^\rho_{q_c,q_v}(\boldsymbol{\xi}) = \langle \chi_{q_c}(\boldsymbol{r};\boldsymbol{\xi})| \, \boldsymbol{D}^\rho(\boldsymbol{r}) \, |\chi_{q_v}(\boldsymbol{r};\boldsymbol{\xi})\rangle_{\boldsymbol{r}} \, . \tag{9.25}$$

The subscript $\boldsymbol{r}$ denotes an expectation value taken over electronic space (equivalently, an integral over all $\boldsymbol{r}$-space). $\mu^\rho_{q_c,q_v}$ is the ρth component of the transition moment between a valence electron with momentum q_v and a conduction electron with momentum q_c.

In terms of the transition moments, and using B.O. energies, the Raman amplitude reads

$$
\begin{aligned}
\alpha^{\rho,\sigma}_{m_v,m_f} &= \frac{1}{\hbar} \sum_{v,c,m} \left[\frac{\langle \phi_{m_f}(\boldsymbol{\xi})| \, \mu^\sigma_{q_v,q_c}(\boldsymbol{\xi})^\dagger \, |\phi_{m_{v,c}}(\boldsymbol{\xi})\rangle \, \langle \phi_{m_{v,c}}(\boldsymbol{\xi})| \, \mu^\rho_{q_c,q_v}(\boldsymbol{\xi}) \, |\xi_{m_i}(\boldsymbol{\xi})\rangle}{E_{m_i} - E_{v,c,m} + \hbar\omega_I - i\Gamma_{v,c,m}} \right] \tag{9.26} \\[2mm]
&= \frac{1}{\hbar} \sum_{v,c,m} \left[\frac{\langle \xi_{q_v,q_c,m_f}(\boldsymbol{\xi}) \, |\phi_{m_{v,c}}(\boldsymbol{\xi})\rangle \, \langle \phi_{m_{v,c}}(\boldsymbol{\xi})| \, \xi_{q_c,q_v,m_i}(\boldsymbol{\xi})\rangle}{E_{m_i} - E_{v,c,m} + \hbar\omega_I - i\Gamma_{v,c,m}} \right] \, . \tag{9.27}
\end{aligned}
$$

9.6.2 Transition Moment Coordinate Dependence

The transition moment is dependent on nuclear coordinates (equivalently, phonons) $\boldsymbol{\xi}$. This can be made explicit by expanding the transition moment around $\xi = 0$:

$$|\xi_{q_c,q_v,m_i}(\boldsymbol{\xi})\rangle \equiv \mu^\rho_{q_c,q_v}(\boldsymbol{\xi}) |\phi_{m_i}(\boldsymbol{\xi})\rangle \tag{9.28}$$

$$= \left(\mu^\rho_{q_c,q_v}(\boldsymbol{\xi}_0) + \sum_{j,k} \left. \frac{\partial \mu^\rho_{q_c,q_v}(\boldsymbol{\xi})}{\partial \xi_{j,k}} \right|_{\boldsymbol{\xi}_0} \cdot \xi_{j,k} + \dots \right) |\phi_{m_i}(\boldsymbol{\xi})\rangle \tag{9.29}$$

The first term is called the Albrecht A term while the second is the B term. The A term is responsible for phononless transitions while the the the B term affects one-phonon transitions (as can be seen by reexpressing $\boldsymbol{\xi}$ in terms of phonon annihilation and creation operators). Higher order expansion is unecessary for Raman. Note that this is not a perturbative expansion.

Inclusion of only the A term corresponds to the Condon approximation, which is generally sufficient for off-resonant Raman spectroscopy. Such an approximation is behind Placzek polarizability which is the go-to formalism to describe molecular Raman spectroscopy in chemistry. However, since in extended large systems the vibrational states of excited electronic surfaces are all equivalent, it is necessary to include the B term to describe Raman processes in condensed matter. Without the B term, electronic transitions could not be accompanied by vibrational excitation since the state's initial vibrational wavefunction would be orthogonal to any other intermediate and final vibrational state (see Figure 9.8).
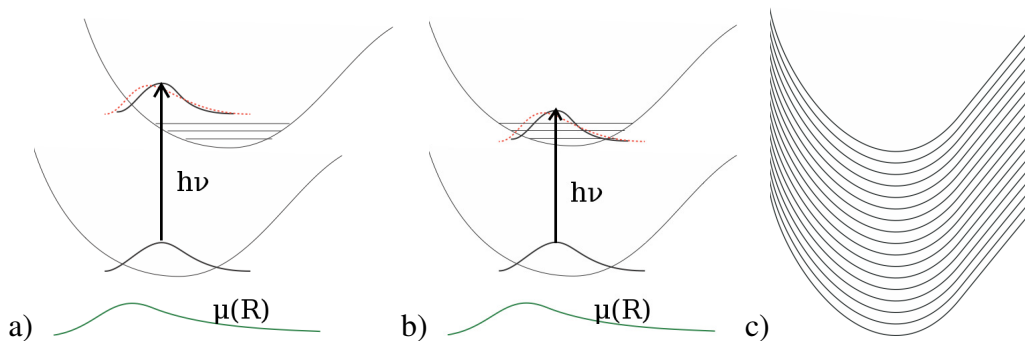

Figure 9.8:

9.7 KHD with the Albrecht Term

Including the transition moment to first order in $\boldsymbol{\xi}$,

$$
\alpha^{\rho,\sigma}_{m_v,m_f} \approx \frac{1}{\hbar} \sum_{v,c,m} \left[\frac{\langle \xi_{m_i}(\boldsymbol{\xi})| \left(\mu^\rho_{q_c,q_v}(\boldsymbol{\xi}_0) + \left. \frac{\partial \mu^\rho_{q_c,q_v}(\boldsymbol{\xi})}{\partial \boldsymbol{\xi}} \right|_{\boldsymbol{\xi}_0} \cdot \boldsymbol{\xi} \right) |\chi_m(\boldsymbol{\xi})\rangle}{E_{m_i} - E_{v,c,m} + \hbar\omega_I - i\Gamma_{q_c,m}} \right.
$$
$$
\left. \times \frac{\langle \chi_m(\boldsymbol{\xi})| \left(\mu^\rho_{q_c,q_v}(\boldsymbol{\xi}_0) + \left. \frac{\partial \mu^\rho_{q_c,q_v}(\boldsymbol{\xi})}{\partial \boldsymbol{\xi}} \right|_{\boldsymbol{\xi}_0} \cdot \boldsymbol{\xi} \right) |\xi_{m_i}(\boldsymbol{\xi})\rangle}{E_{m_i} - E_{v,c,m} + \hbar\omega_I - i\Gamma_{q_c,m}} \right].
$$

(9.30)

9.8 Graphene's Raman Spectrum

We now proceed to apply K.H.D. to graphene. Its Raman spectrum, as well as the corresponding phonon modes, are shown in Figure 9.9. Note that in Raman spectra, the frequency shift corresponds to the difference between the incident and emitted energies of light. Hence, they can be considered to directly correspond to the energies of the phonons that are excited in the process.
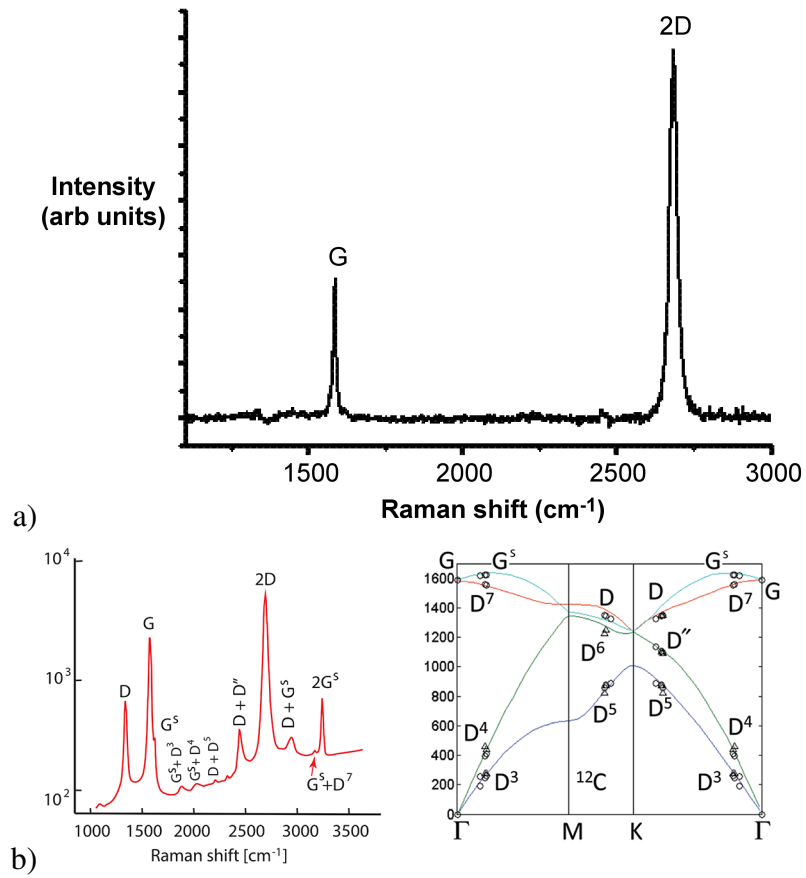
Figure 9.9: a) from [87] b) from [88]

9.8.1 G Peak

In terms of electronic transitions excited by light, the long wavelength of light compared to the (infinitely, relatively so,) periodic sample means that the only allowed electronic transitions are vertical and have the same k before and after excitation. This means that electrons with a particular k from a particular valence band jump to a free conduction band with the same k, leaving being a hole with momentum k. This is a momentum-conserving process and, in the simplest case, means that the electron must vertically relax back and recombine with its hole releasing light in the process. Indeed, these processes are what make up Rayleigh scattering in solid-state materials.

If we move on to the Raman spectrum of materials, we must now consider processes that are "phonon-assisted" at excitation and/or relaxation. Upon excitation with light, electrons jump from a valence state to a conduction state which no longer has the same vibrational quantum numbers. Again, this must be accomplished in such a way that conserves quasi-momentum, since that is a good quantum number in periodic systems. Since phonons have their own momentum q, this must be considered in the full process. Every step in the process must be momentum-conserving.

Therefore, upon excitation of an electron with momentum k, if the vibrational quantum numbers of the new conduction state correspond to a phonon with momentum q also being excited, this "phonon-assisted" step necessitates that the excited electron have momentum $k - q$ in order for it overall step to be momentum-conserving. It is of course important that such a conduction state exists in the material's spectrum. That is, the conduction state must have the correct total energy of electron and phonon to be matched with the incident light and the total momentum of the state $((k - q) + q)$ must be equal to the initial state's momentum $(= 0)$. Otherwise, this is a "virtual" state and is not on-shell. A similar calculus must be considered if more than one phonon is excited or, inversely, if phonons are relaxed. Two-phonon assisted transitions produce Raman peaks that are "overtones" of their one-phonon "fundamental"s.

In practice, it is often easiest to make the Born-Oppenheimer approximation to deal with such problems. One benefit of this approach is that the notions of electronic energies can be formalized

as the eigenenergies of

$$H_e(\boldsymbol{r}, \boldsymbol{R})\phi(\boldsymbol{r}; \boldsymbol{R}) = E_e\phi(\boldsymbol{r}; \boldsymbol{R}). \tag{9.31}$$
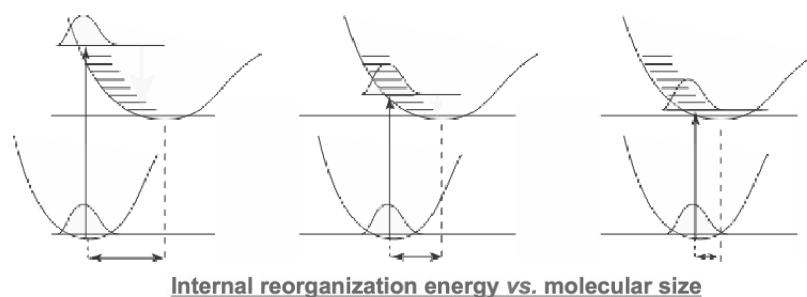
"Phonon energies" can then be found by mean-field or better correlated methods. We can then again appeal to the fact that the periodic structure can be considered to be infinitely long in the periodic directions. This means that the reorganization energy, also called the Huang-Reese factor, is zero in the related degrees of freedom. In other words, after an electron is excited from one electronic-vibrational state to another, it is unable to relax to a lower vibrational state because its new electronic character (delocalized over all space) has negligible impact on the nuclei (or equivalently, phonons, whose vibrations are delocalized over all space), as you might imagine to be the case when there are infinitely many such nuclei. In yet another way, this means that all the electronic Born-Oppenheimer surfaces are the same and so excitation of a vibrational eigenstate from one to another produces another steady-state (see Figure 9.10 for experimentally determined reorganization energies with respect to the length of a particular molecule.).

9.9   Internal Reorganization Energy

What this means for us is that we can deal with "electronic energies" and "phonon energies" as two separate things that don't affect each other. Electronic state A has the same phonon energies as electronic state B and so there is no need to ascribe a separate index on the vibrational eigenstates χ from the Born-Oppenheimer to indicate which electronic state they correspond to:

$$\overset{\text{ele. st. vib. st.}}{\sum_i \sum_j} [\phi_i(\boldsymbol{r}; \boldsymbol{\chi})\chi_{i,j}(\boldsymbol{\chi})] \rightarrow \left[\overset{\text{ele. st.}}{\sum_i} \phi_i(\boldsymbol{r}; \boldsymbol{\chi})\right]\left[\overset{\text{vib. st.}}{\sum_j} \chi_j(\boldsymbol{\chi})\right]. \tag{9.32}$$

In the condensed matter community, a starting assumption to treating this problem (which leads to the D.R. formulation for Raman scattering), is that the state is a direct product of electronic and vibrational states. As we can see, the two are thus equivalent starting points thanks to the zero reorganization energy in (large) periodic systems.
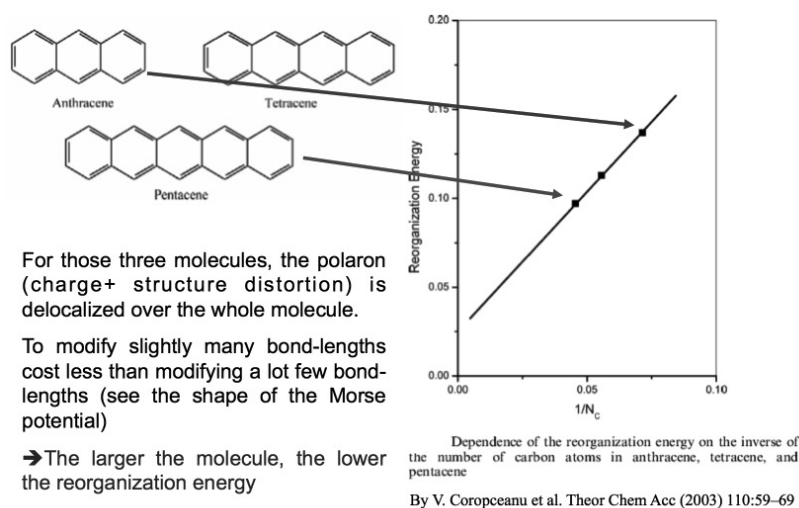
Figure 9.10: From [86].

Having thus established the validity of the separate treatment of electronic and vibrational energies, a given periodic system can be fully characterized by its electronic energy dispersion and its phonon energy dispersion. The electronic dispersion remains the same no matter what the state's current population is in terms of its phonon dispersion.

As an aside, note that the electronic dispersion is a fermionic energy spectrum while the phonon dispersion is for bosons. That means that the former's occupation is characterized by a Fermi energy (in the thermalized or zero temperature case) while the latter's states are always all occupied and are at least in their ground state.

With the electron and phonon energy dispersion of our material in hand, we now set out with the objective to find all possible on-shell pathways for, to begin with, one-phonon steps. Given an incident laser energy $\hbar\omega$, an electron with some momentum k and energy $E_{k,\nu}$ must make a

transition from an occupied valence band ν, assisted by a phonon with momentum q and energy $E_{q,\mu}$ from some phonon band μ, to an unoccupied conduction band ρ with energy $E_{k',\rho}$. Hence, the following two conditions must be satisfied:

$$E_{k,\nu} + \hbar\omega = E_{k',\nu} + E_{q,\mu}, \tag{9.33}$$
$$k = k' + q. \tag{9.34}$$

We will now detail how these are satisfied to produce the dominant peaks in Raman.

For a one-phonon process where the phonon has momentum k, the electron must be assisted either on the way up or on the way down. In either case, it must recombine with its hole. If it is phonon-assisted on the way up from the valence to the conduction band, it can only relax back to its hole via a vertical phonon emission process. Similarly, if it is phonon-assisted on the way down from the conduction band to the valence band, it must be initially vertically excited leaving behind a hole. In order to satisfy momentum conservation (Eq. 9.34) and make it back to its hole, this means that only $q = 0$ phonons can be excited - phonons with no quasimomentum modulation. In the two-atom case, this corresponds to the zig-zag mode, also called the G mode in reference to its Raman signature: the G peak. In the six-atom unit cell, this corresponds to the breathing mode. The former is Raman visible while the latter is symmetry-forbidden as we will discuss.

The G peak is produced in two ways. The first involves a phonon-assisted transition of an electron with momentum q from the valence band to the conduction band. In the excited state, it still has momentum q since the phonon it produced on the way up "cost" no momentum. On the other hand, the *energy* cost of exciting the phonon is finite and is partially paid for by the energy of the incident laser. The rest of the laser energy goes into the excited electron energy's difference with the valence state. This is clear in Figure 9.11 where the blue vertical line denotes the full laser energy while the red vertical line shows how much is left over after accounting for one G phonon excitation. Notice that if we consider energies on the scale of the linear Dirac cone, the red line

is necessarily displaced closer to the conical intersection in momentum space so that the transition remains on-shell.

The second way to produce the G peak is the reverse of the pathway already described: the phonon is excited from the valence band to the conduction band via the blue arrow, since it doesn't produce a phonon, and then relaxes by producing a phonon on the way down and emitting light with energy that corresponds to the rest of the electronic energy left to get to its original valence state.
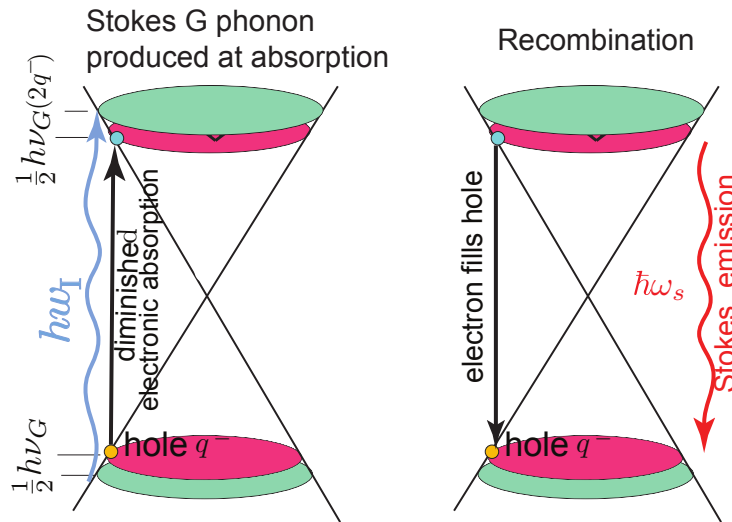
Figure 9.11:

There are two equivalent zig-zag G modes. This is clear in the two-atom unit cell phonon dispersion that is annotated in Figure 9.12. Therefore, the G peak is actually doubly-degenerate. The polarization of the light will generally favor excitation of one of the degenerate modes over the other, because of their different transition moments. However, there are few polarization-sensitive experimental studies out there that look at this so we won't either.

Like the zig-zag mode in the two-atom unit cell, the breathing mode is the $k = 0$ phonon mode in the six atom unit cell. Figure 9.13 shows the two-fold degeneracy of the breathing mode present in the six-atom unit cell phonon dispersion. These results were obtained by simply extending the nearest-neighbor tight-binding results of Sahoo *et. al.*[79] and so the plotted energies shouldn't be

taken seriously. The figure is meant to pedagogically show the possible modes in the six-atom unit cell only. As can be seen, the highest energy $k = 0$ phonon modes are still the doubly-degenerate zig-zag modes. Immediately below them, and absent in the two-atom phonon dispersion, are the breathing modes. They are also doubly-degenerate.
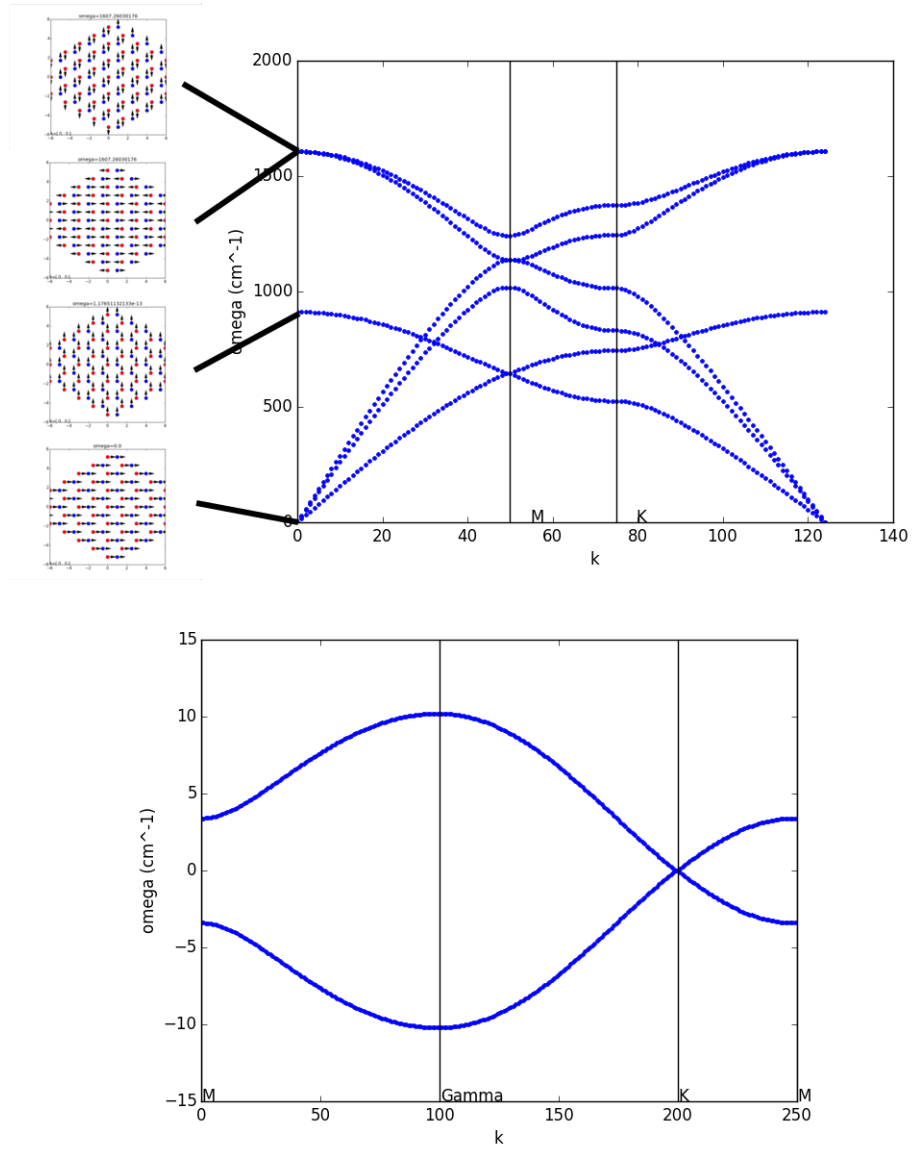
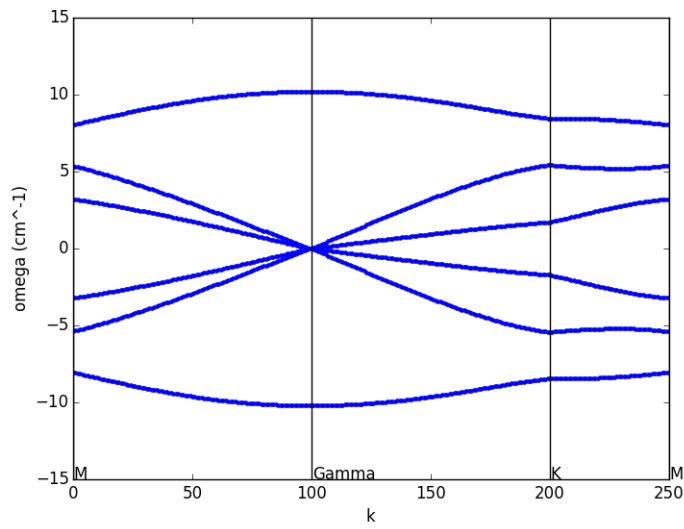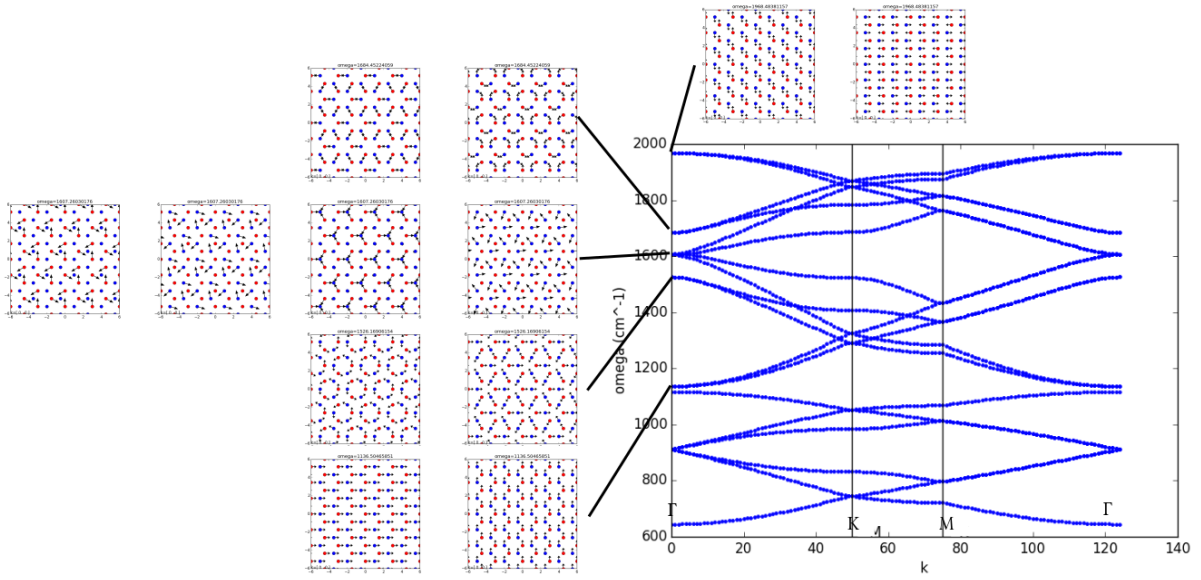Figure 9.12: Phonon from formalism in [79] and electronic from formalism in [77].

Figure 9.13: Phonon from formalism in [79] and electronic from formalism in [77].

One might expect a corresponding Raman peak to be present in experimental spectra. However, it is symmetry-forbidden. The atoms all moving away from each other mean that there is no net change in polarization. Indeed, calculations also show that it has a vanishing transition moment.

Similarly, all other one-phonon processes, corresponding to $k = 0$ phonons in larger unit cells, must have transition moments that are too small to produce Raman peaks.

9.9.1   Other Peaks ($k \neq 0$)

Now that we've discussed all possible one-phonon processes when momentum is a good quantum number, we move on to describe two-phonon processes where the $k = 0$ limitation is no longer necessary. This is because any displacement in the k-axis of the electron during its transition from the valence to conduction band from phonon production can now be reversed by exciting or relaxing a phonon with the opposite momentum on the electron's way back down to the valence band. This allows it to return and recombine with its hole.

The most prominent example of such a two-phonon process is an overtone to a finite-momentum breathing mode, often called the 2D process after its Raman peak. As explained earlier, zero-momentum breathing modes, be they fundamentals or overtones, are symmetry-forbidden and have zero transition moments. The symmetry of these transition moments is broken for finite-momentum breathing modes and so they are allowed. The reason we're focusing on this mode's finite-k overtone is that its transition moment is the greatest of all others. Indeed, in finite molecules where it is symmetry-allowed because its edges allow it to be polarizable, the breathing mode - which is sometimes referred to simply by its group symmetry A_1g - always produces the brightest peak.

9.9.2   Sliding

There is another reason that the 2D peak is so bright in graphene's Raman spectrum. This has to do with a pathway that we colloquially refer to as the "sliding transition". Since the energy scale of the incident laser used in Raman spectroscopy is in the regime of the Dirac cone, the linear
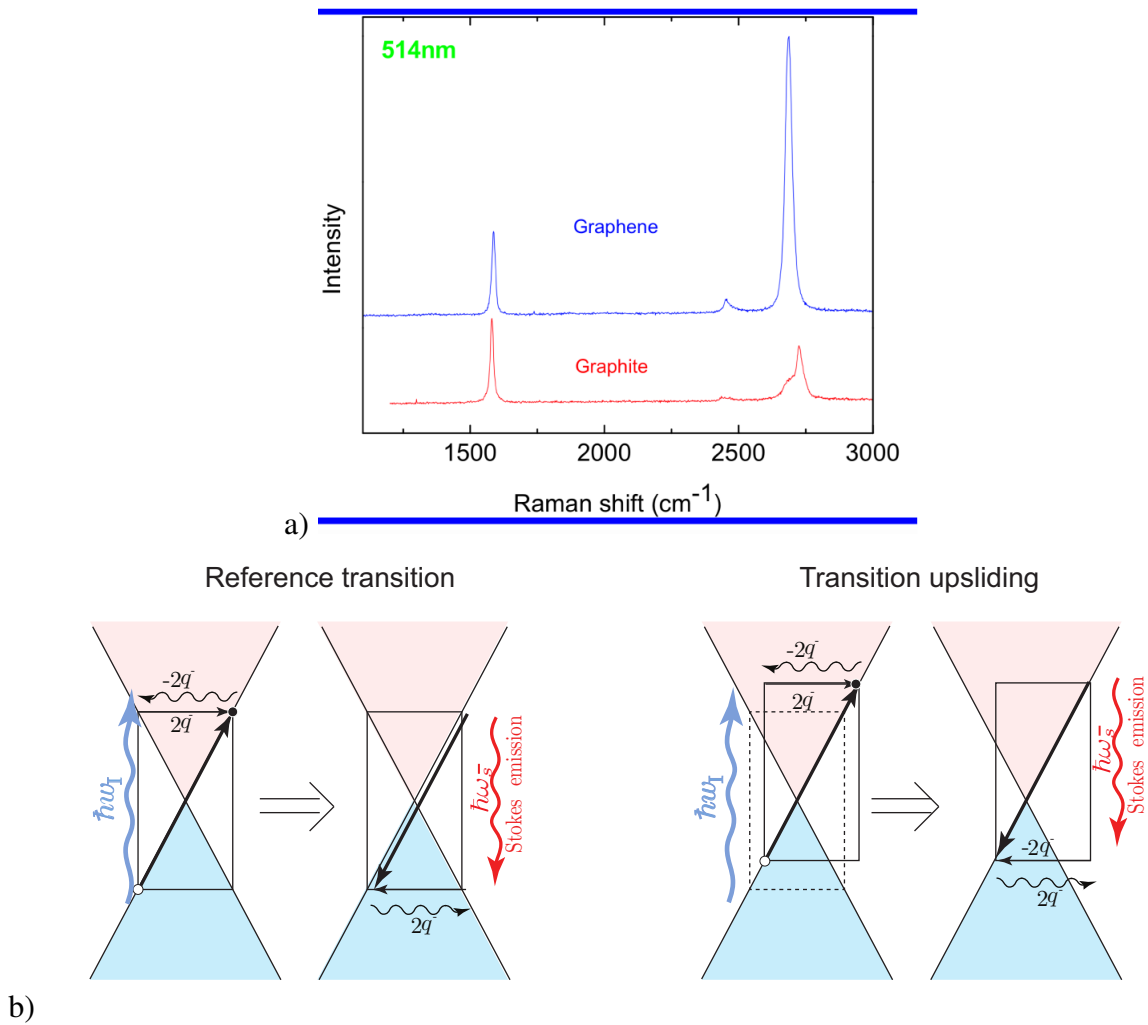
Figure 9.14: a) From [90, 91]

character of the electronic spectrum is dominant. This means that it is now possible to undergo the same vertical excitation and same horizontal k-displacement in a continuous interval of starting momenta, as sketched in Figure 9.14. The left panel of Figure 9.14c shows a reference transition with some energy δE across the cone δk. The right panel shows how the same transition is possible "above" or "below" this reference transition with the same δE and δk, hence the term "sliding transition".

Aside from the multitude of these transitions, the high peak intensity is also bolstered by the fact that such transitions add up coherently in the K.H.D. formalism:

$$\alpha_{m_v,m_f}^{\rho,\sigma} = \frac{1}{\hbar} \sum_{v,c,m} \left[\frac{\langle \phi_{q_v,q_c,m}(\boldsymbol{\xi}) | \chi_m(\boldsymbol{\xi}) \rangle \langle \chi_m(\boldsymbol{\xi}) | \phi_{q_c,q_v,m_i}(\boldsymbol{\xi}) \rangle}{E_{m_i} - E_{v,c,m} + \hbar\omega_I - i\Gamma_{q_c,m}} \right]. \tag{9.35}$$

The χ_m in the sum correspond to the same phonon for a sliding transition. They are summed up *and then* squared, allowing their coherence to (generally) increase their magnitude.
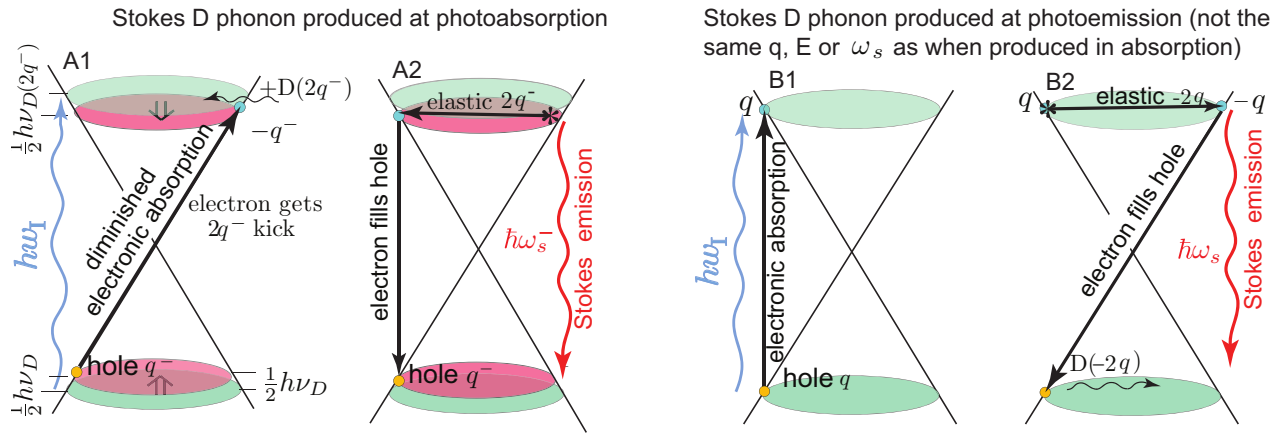
9.9.3 D Peak

Figure 9.15:

We finally consider the case in graphene when the sample is dirty, or small, such that quasimomentum formally ceases to be a good quantum number. In this case, as insinuated earlier, a new bright peak appears in the Raman spectrum, the D peak corresponding to the "finite-momentum" breathing mode that is the brightest peak in related molecules, such as benzene and its derivatives. Since it is a one-phonon process, it cannot benefit from sliding transitions. Therefore, its brightness can only come from the strength of its transition moment, which as we have indicated, is substantial.

D Dispersion

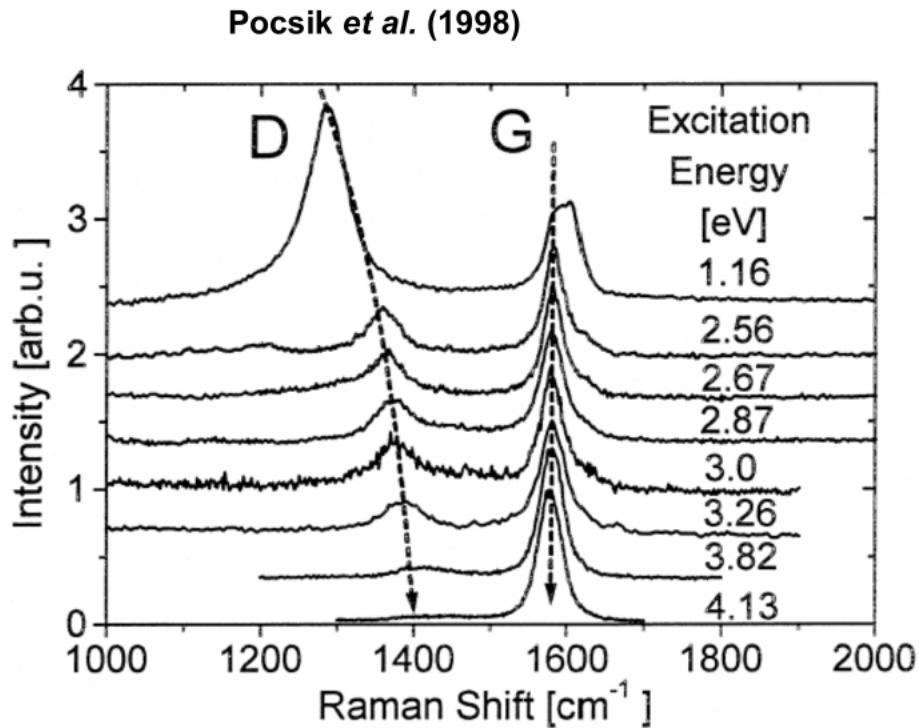The D peak exhibits a dispersion with respect to incident laser energy. This is shown in Figure 9.16.

Figure 9.16: From [92]

The reason for this dispersion has to do with the fact that, for instance, at larger laser frequencies, the resultant electronic momentum must increase with respect to the Dirac cone center and so a correspondingly larger momentum phonon is excited or destroyed. Since the phonons have a dispersion of their own, phonons with a different energy from before are excited. In particular for the D phonon, larger momentum modes cost more energy and so the resultant Raman shift of the D peak increases with increasing laser energy.

9.9.4 Stokes/Anti-Stokes Anomalies

The asymmetry in the Stokes versus anti-Stokes frequencies of the D and 2D bands are graphene Raman anomalies. In a small molecule, the Stokes and anti-Stokes bands measure the same vibrational state, and there cannot be any difference between the two: they are symmetrically

spaced across the Rayleigh line. For the graphene D band, the asymmetry is instead about 8 or $9\,\mathrm{cm}^{-1}$.
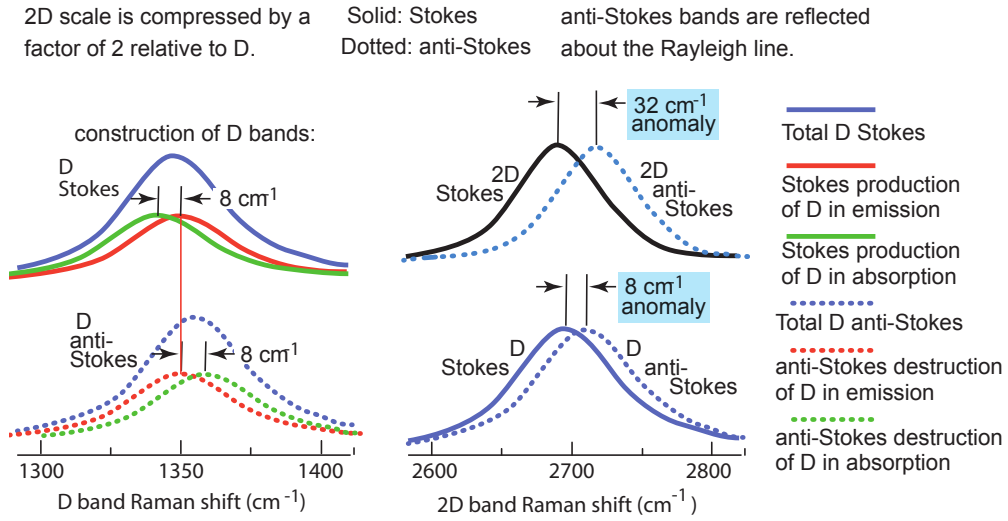
D and 2D Stokes, anti-Stokes anomalies

Figure 9.17:

The D mode Stokes band is an average of emission and absorption phonon production, with emission production unshifted. Production in absorption is shifted down 8 cm^{-1}, by the dispersion of D and the diminishment cause by energy conservation. The average of the two is 4 cm^{-1} closer to the Rayleigh line than the undiminished emission production alone would be (see Figure 9.17). Similarly, the D mode anti-Stokes production in absorption also consists of two bands, overall 4 cm^{-1} higher in energy and farther from the Rayleigh band. At 3.5 eV and 1350 cm^{-1}, the Stokes vs the anti-Stokes D phonons (reflected about the Rayleigh line for comparison) will differ by about 8.4 cm^{-1}. This is an anomalous Stokes, anti-Stokes asymmetry of about 8.4 wave numbers, in excellent agreement with experiment. Thus, the anomaly has a simple explanation in terms of phonon production in absorption vs emission.

9.10 DR "Theory"

Martin and Falicov[94] introduced a framework for resonant Raman scattering that was taken up by the condensed matter community in an attempt to describe the Raman spectrum of graphene. Unlike the second-order perturbation in K.H.D., their formulation relies on a fourth-order perturbation: two orders from light-matter interaction and two orders from electron-phonon scattering. The argument for why such a high-order treatment captures the dominant Raman processes lies in the fact that two out of the four are "on-shell" or resonant, so that their corresponding denominators have zero real part, hence the name of this formalism: double-resonance (D.R.). We will now use this acronym for the rest of this chapter and it is not to be confused with the dephasing relation discussed earlier in this thesis.

Mathematically, the differential amplitude in D.R. is:

$$\sum_f \left| \sum_{a,b,c} \frac{\mathcal{M}_{fc}\mathcal{M}_{cb}\mathcal{M}_{ba}\mathcal{M}_{ai}}{(E_i - E_c - i\frac{\gamma_c}{2})(E_i - E_b - i\frac{\gamma_b}{2})(E_i - E_A - i\frac{\gamma_a}{2})} \right|^2 \delta(E_i - E_f). \qquad (9.36)$$

The two outer matrix elements in the numerator $\mathcal{M}_{fc}$ and $\mathcal{M}_{ai}$ denote light-matter interaction, corresponding to excitation of an electron from an initial valence state i to a conduction band and

from the conduction band to a final valence state f respectively, while the inner two, $\mathcal{M}_{cb}$ and $\mathcal{M}_{ba}$, correpsond to electron-phonon scattering. The corresponding energies of all these states with respect to the starting energy is given in the denominator, as can be shown in perturbation theory. Since this is a differential amplitude, the energy that the derivative is taken with respect to is missing in the denominator.

More precisely, for the two electron-phonon scattering that contributes to the 2D peak in graphene, the intensity of the Raman spectrum is[77]:

$$I(\omega) = \frac{1}{N_q} \sum_{\boldsymbol{q},\nu,\mu} I_{\boldsymbol{q},\nu,\mu}^{pp} \delta(\omega_L - \omega - \omega_{-\boldsymbol{q}}^{\nu} - \omega_{\boldsymbol{q}}^{\mu})[n(\omega_{-\boldsymbol{q}}^{\nu}) + 1][n(\omega_{\boldsymbol{q}}^{\mu} + 1], \tag{9.37}$$

where

$$I_{\boldsymbol{q},\nu,\mu}^{pp} = \left| \frac{1}{N_k} \sum_{\boldsymbol{k},\beta} K_{\beta}^{pp}(\boldsymbol{k},\boldsymbol{q},\nu,\mu) \right|^2, \tag{9.38}$$

for

$$K_{ee1}^{pp}(\boldsymbol{k},\boldsymbol{q},\nu,\mu) = \frac{\langle \boldsymbol{k}\pi | D_{\text{out}} | \boldsymbol{k}\pi^* \rangle \langle \boldsymbol{k}\pi^* | \Delta H_{-\boldsymbol{q},\mu} | \boldsymbol{k}+\boldsymbol{q},\pi^* \rangle \langle \boldsymbol{k}+\boldsymbol{q},\pi^* | \Delta H_{\boldsymbol{q},\nu} | \boldsymbol{k},\pi^* \rangle \boldsymbol{k},\pi^* D_{\text{in}} | \boldsymbol{k}\pi \rangle}{(\epsilon_L - \epsilon_{\boldsymbol{k}}^{\pi^*} + \epsilon_{\boldsymbol{k}}^{\pi} - \hbar\omega_{-\boldsymbol{q}}^{\nu} - \hbar\omega_{\boldsymbol{q}}^{\mu} - i\frac{\gamma_{\boldsymbol{k}}^C}{2})(\epsilon_L - \epsilon_{\boldsymbol{k}+\boldsymbol{q}}^{\pi^*} + \epsilon_{\boldsymbol{k}}^{\pi} - \hbar\omega_{-\boldsymbol{q}}^{\nu} - i\frac{\gamma_{\boldsymbol{k}}^B}{2})(\epsilon_L - \epsilon_{\boldsymbol{k}}^{\pi^*} + \epsilon_{\boldsymbol{k}}^{\pi} - i\frac{\gamma_{\boldsymbol{k}}^A}{2})}. \tag{9.39}$$

The decision of the community to use this formalism seems to, at least partly, stem from the fact that some studies have shown that graphene's electronic properties are poorly captured within the Born-Oppenheimer approximation. This has to do with the Dirac cones where the Born-Oppenheimer surface cross each other signalling a breakdown of that adiabatic approximation. The added two orders of perturbation theory in electron-phonon scattering can be described as a diabatic correction to the Born-Oppenheimer K.H.D. formalism.

9.11   DR and the D Peak

Reich and coworkers[93] began with the expression from Falicov *et al.*[94] that is the transition amplitude from fourth order perturbation theory, and applied it around the region of graphene's

electronic linear Dirac cone:

$$K_{2f,10} = M_f \mathcal{M}_{ba} \mathcal{M}_{cb} M_0 \sum_{a,b,c} \frac{1}{(E_1 - E_{ai}^e - i\hbar\gamma)(E_1 - \hbar\omega_{\text{ph}} - E_{bi}^e - i\hbar\gamma)(E_1 - \hbar\omega_{\text{ph}} - E_{ci}^e - i\hbar\gamma)}.$$
$$(9.40)$$

E_1 is the starting energy of a valence electron, $E_{ai}^e = |k|(v_2 - v_1)$ is the energy difference between the electron state in the conduction band at point a and the valence band energy directly below it, $E_{bi}^e = \mp q v_{1/2}$ is the electron energy at point b in the conduction band after "colliding" with a phonon with energy $\hbar\omega_{\text{ph}}$ and with momentum q, and E_{ci}^e is the energy of the electron at point c after "elastically" backscattering. As Figure 9.18 illustrates, E_{ci}^e is shown to be off-shell or a "virtual" state with respect to the (unperturbed) electron energy-momentum dispersion of graphite (or graphene) which appears to serve as the zeroth-order eigenstate basis upon which the authors perform their perturbation expansion. Their perturbation is electron-phonon scattering. Their unperturbed system, according to the energies they use and this graph, is the Born-Oppenheimer Hamiltonian from which Figure 9.18's energies are obtained. Even if one uses tight-binding to obtain this spectrum, such treatments result in energy dispersions that agree exactly with Born-Oppenheimer since the Yang relaxation energy of graphene is almost zero, i.e. the electronic states of the system lie directly on top of one another (possessing unit Franck-Condon overlap).
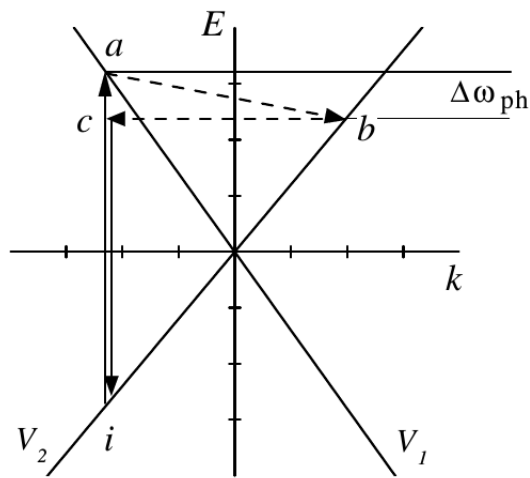

Figure 9.18: From [93]

The authors proceed to set $E_{ci}^e = |k|(v_2 - v_1)$. With this last step, they are able to reexpress their sum over a, b, and c as the integral:

$$K_{2f,10} = \frac{M_f \mathcal{M}_{ba} \mathcal{M}_{cb} M_0 (2\kappa_2 - q)}{(v_2 - v_1)^3 \left(\kappa_2 - q\frac{v_2}{v_2 - v_1}\right) \left(\kappa_2 + q\frac{v_1}{v_2 - v_1}\right)}$$
$$\times \int_0^\infty \frac{dk}{(\kappa_1 - k)(\kappa_2 - k)} \tag{9.41}$$

where $\kappa_1 = (E_1 - i\hbar\gamma)/(v_2 - v_1)$ and $\kappa_2 = (E_1 - \hbar\omega_{\mathrm{ph}} - i\hbar\omega)/(v_2 - v_1)$.

The evaluation of this integral leads to their main result:

$$K_{2f,10} = \frac{a M_f \mathcal{M}_{ba} \mathcal{M}_{cb} M_0}{\left(\kappa_2 - q\frac{v_2}{v_2 - v_1}\right) \left(\kappa_2 + q\frac{v_1}{v_2 - v_1}\right)}, \tag{9.42}$$

where $a = \ln(\kappa_2/\kappa_1)(2\kappa_2 - q)/[(v_2 - v_1)^2 \hbar\omega_{\mathrm{ph}}]$.

This means that during this whole path there exists a double resonance and that there exists a term in this fourth-order perturbation sum that diverges (goes to infinity) when

$$q = \frac{E_1 - \hbar\omega_{\mathrm{ph}}}{v_2} \text{ or } \frac{E_1 - \hbar\omega_{\mathrm{ph}}}{-v_1}. \tag{9.43}$$

There is at least one other work considered seminal on the D peak under the DR treatment[95].

9.12 Numerical Agreement of DR with Graphene's Raman Spectrum

The numerical agreement between a particular (approximate) implementation of DR and the experimentally-obtained spectrum was performed by Venezuela *et al*. The agreement can be seen in Figure 9.19.
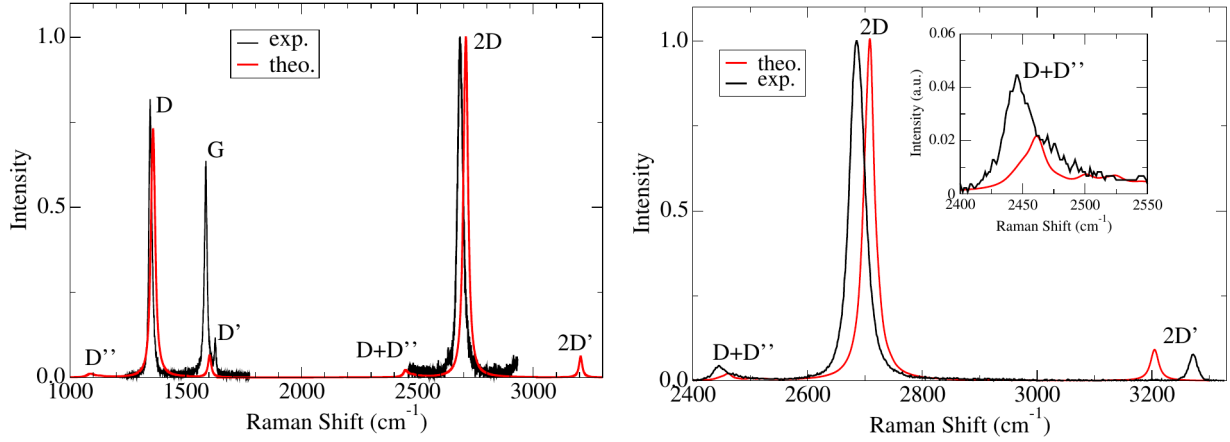
135

Figure 9.19: From [77].

9.13 Appendix

9.13.1 The Born-Oppenheimer Approximation

Consider

$$H = H_e + T_n \tag{9.44}$$

where in atomic units

$$H_e = -\sum_i \frac{1}{2} \frac{\partial^2}{\partial \boldsymbol{r}_i^2} - \sum_{i,A} \frac{Z_A}{r_{i,A}} + \sum_{i<j} \frac{1}{r_{i,j}} + \sum_{A>B} \frac{Z_A Z_B}{R_{A,B}} \tag{9.45}$$

and

$$T_n = -\sum_A \frac{1}{2M_A} \frac{\partial^2}{\partial \boldsymbol{R}_A^2}, \tag{9.46}$$

where $\boldsymbol{r}_i$ are the positions of the electrons, $\boldsymbol{R}_A$ are the positions of the nucleons, $r_{i,A} = |\boldsymbol{r}_i - \boldsymbol{R}_A|$, $R_{A,B} = |\boldsymbol{R}_A - \boldsymbol{R}_B|$, $r_{i,j} = |\boldsymbol{r}_i - \boldsymbol{r}_j|$, and M_A is the mass of nucleon A.

Let us write the eigenfunctions of this Hamiltonian

$$\Psi(R,r) = \sum_{k=1}^{K} \chi_k(\boldsymbol{r}; \boldsymbol{R}) \phi_k(\boldsymbol{R}), \tag{9.47}$$

such that

$$H_e \chi_k(\boldsymbol{r}; \boldsymbol{R}) = E_k(\boldsymbol{R}) \chi_k(\boldsymbol{r}; \boldsymbol{R}) \tag{9.48}$$

and

$$\langle \chi_{k'} | \chi_k \rangle_{\boldsymbol{r}} = \delta_{kk'} \tag{9.49}$$

for K electronic (eigen)states.

Note that $\chi_k \phi_k$ are a complete basis and we have made no approximation so far except, as we will show, it is necessary that χ_k is C^2.

The semicolon in $\chi_k(\boldsymbol{r}; \boldsymbol{R})$ is meant to denote that these electronic wavefunctions are "parametrized" by the nuclear coordinates $\boldsymbol{R}$, i.e. we only ever consider $\chi_k(\boldsymbol{r})$ at a particular (or "fixed") value of $\boldsymbol{R}$, but this is merely semantics and we can equally correctly write $\chi_k(\boldsymbol{r}, \boldsymbol{R})$.

$$\langle \chi_{k'} | H_e | \chi_k \rangle_{\boldsymbol{r}} \equiv H_{k',k}(\boldsymbol{R}) = \delta_{kk'} E_k(\boldsymbol{R}), \tag{9.50}$$

and is thus diagonal in k.

$$\langle \chi_{k'} | T_n | \chi_k \rangle_{\boldsymbol{r}} \equiv T_n(\boldsymbol{R})_{k',k}, \tag{9.51}$$

is not generally diagonal.

$$
\begin{aligned}
T_n(R)_{k,k'} &= \left\langle \Psi_{k'} \left| \sum_{A,\alpha} \frac{-1}{2M_A} \frac{\partial}{\partial \boldsymbol{R}_{A,\alpha}} \frac{\partial}{\partial \boldsymbol{R}_{A,\alpha}} \right| \chi_k \right\rangle_{\boldsymbol{r}} && (9.52) \\
&= \sum_{A,\alpha} \frac{-1}{2M_A} \langle \chi_{k'} | \chi_k \rangle_{\boldsymbol{r}} \frac{\partial^2}{\partial \boldsymbol{R}_{A,\alpha}} + \sum_{A,\alpha} \frac{-1}{M_A} \left\langle \chi_{k'} \left| \frac{\partial}{\partial \boldsymbol{R}_{A,\alpha}} \chi_k \right\rangle_{\boldsymbol{r}} \frac{\partial}{\partial \boldsymbol{R}_{A,\alpha}} && (9.53) \\
&\quad + \left\langle \chi_{k'} \left| \sum_{A,\alpha} \frac{-1}{2M_A} \frac{\partial^2}{\partial \boldsymbol{R}_{A,\alpha}^2} \chi_k \right\rangle_{\boldsymbol{r}} \\
&= \sum_{A,\alpha} \frac{-1}{2M_A} \frac{\partial^2}{\partial \boldsymbol{R}_{A,\alpha}} \delta_{kk'} + \underbrace{\sum_{A,\alpha} \frac{-1}{M_A} \left\langle \chi_{k'} \left| \frac{\partial}{\partial \boldsymbol{R}_{A,\alpha}} \chi_k \right\rangle_{\boldsymbol{r}} \frac{\partial}{\partial \boldsymbol{R}_{A,\alpha}}}_{\text{``B.O. off-diagonal correction''}} && (9.54) \\
&\quad + \underbrace{\left\langle \chi_{k'} \left| \sum_{A,\alpha} \frac{-1}{2M_A} \frac{\partial^2}{\partial \boldsymbol{R}_{A,\alpha}^2} \chi_k \right\rangle_{\boldsymbol{r}}}_{\text{B.O. diagonal correction}}.
\end{aligned}
$$

$$(9.55)$$

The last two terms denote the vibronic coupling and can be separated into the Born-Oppenheimer "off-diagonal" and "diagonal" corrections as indicated.

If we have time-reversal symmetry, i.e. there is no external magnetic field, then $\langle \chi_k(\boldsymbol{r}, \boldsymbol{R}) \rangle_{\boldsymbol{r}} \in \mathbb{R}^n$ and so the B.O. off-diagonal term $\propto \left\langle \chi_{k'} \left| \frac{\partial}{\partial \boldsymbol{R}_{A,\alpha}} \chi_k \right\rangle_{\boldsymbol{r}} = 0$, if $k = k'$.

We can rewrite this term as:

$$
\left\langle \chi_{k'} \left| \frac{\partial}{\partial \boldsymbol{R}_{A,\alpha}} \chi_k \right\rangle_{\boldsymbol{r}} = \frac{\left\langle \chi_{k'} \left| \left[\frac{\partial}{\partial \boldsymbol{R}_{A,\alpha}}, H_e \right] \right| \chi_k \right\rangle_{\boldsymbol{r}}}{E_k(\boldsymbol{R}) - E_{k'}(\boldsymbol{R})}. \tag{9.56}
$$

This makes it clear that this term is small when $E_k - E_{k'} \gg 0$ and big when $E_k - E_{k'} \ll \left\langle \chi_{k'} \left| \left[\frac{\partial}{\partial \boldsymbol{R}_{A,\alpha}}, H_e \right] \right| \chi_k \right\rangle_{\boldsymbol{r}}$ which corresponds to the cases when the B.O. states are far apart or crossing respectively.

Similarly, the B.O. "diagonal" term

$$
\propto \left\langle \chi_{k'} \left| \frac{\partial^2}{\partial \boldsymbol{R}_{A,\alpha}^2} \right| \chi_k \right\rangle_{\boldsymbol{r}} = \frac{\left\langle \chi_{k'} \left| \left[\frac{\partial^2}{\partial \boldsymbol{R}_{A,\alpha}^2}, H_e \right] \right| \chi_k \right\rangle_{\boldsymbol{r}}}{E_k(\boldsymbol{R}) - E_{k'}(\boldsymbol{R})}, \tag{9.57}
$$

exhibits similar behavior (but is also non-zero for $k = k'$).

If we neglect these two terms then we can solve the diagonal, uncoupled, set of nuclear motion equations,

$$\left[T_n + E_k(\boldsymbol{R})\right] \phi_k(\boldsymbol{R}) = E\phi_k(\boldsymbol{R}), \tag{9.58}$$

to get $\{\phi_{k,l}(\boldsymbol{R})\}_{l=1,2,\dots}$. Hence, the full wavefunction $\Psi(\boldsymbol{r}, \boldsymbol{R}) = \sum_{k,l} \chi_k(\boldsymbol{r}; \boldsymbol{R})\phi_{k,l}(\boldsymbol{R})$.

10

Asymptotic Equations for Zeros of Orthogonal Polynomials

I include here some short work on the asymptotic zeros of orthogonal polynomials from the W.K.B. quantization of finite systems. Most of the ideas here are a variant of W.K.B. results that are already well-known, though perhaps presented in a new way through the persepective of systems with finite-dimensional Hilbert spaces.

10.1 Hermite Polynomials from the Holstein-Primakoff Representation

Here we use the Holstein-Primakoff representation for spin systems to derive expressions with solutions that are conjectured to be the zeros of Hermite polynomials $H_n(x)$ as $n \to \infty$. This establishes a correspondence between the zeros of the Hermite polynomials and the boundaries of the position basis of finite-dimensional Hilbert spaces.

The Hermite polynomials are prevalent in many fields. They can be defined as

$$H_n(x) = (-1)^n e^{x^n} \frac{d^n}{dx^n} \left(e^{-x^2} \right). \tag{10.1}$$

In the physics community, they are perhaps best recognized as the Gaussian-weighted eigenfunctions (in position representation) of the quantum harmonic oscillator (with $\hbar = m =$

$\omega = 1$, a convention that will be used for the rest of the paper):

$$\frac{1}{2}\left(x^2 - \frac{d^2}{dx^2}\right)e^{-\frac{x^2}{2}}H_n(x) = \left(n + \frac{1}{2}\right)e^{-\frac{x^2}{2}}H_n(x), \tag{10.2}$$

As such, they are orthogonal over the Gaussian-weighted whole domain, $\int_{-\infty}^{\infty} H_m(x)H_n(x)e^{-x^2}dx = \sqrt{\pi}2^n n!\delta_{nm}$. This last property allows their use in Gaussian quadrature, a useful and popular numerical integration technique where $\int_{-\infty}^{\infty} f(x)dx$ is approximated as $\sum_{j=1}^{n} e^{-x_j^2}f(x_j)$ where x_j are the zeros of $H_n(x)$ and $f(x)$ is a well-behaved function. For this and many other reasons, an analytic formula for the asymptotic zeros of Hermite and other orthogonal polynomials has been a subject of much interest[96, 97, 98, 99, 100, 101, 102], especially in the applied mathematics community and the field of approximation theory.

In this chapter, we examine the position state representation of the eigenstates of finite dimensional S-spin systems, as expressed in the Holstein-Primakoff transformation. As $S \to \infty$, the system becomes the infinite dimensional harmonic oscillator. This association allows me to derive the simple main results presented in eqs 10.6 and 10.7, with solutions that we conjecture become the asymptotic zeros of the Hermite polynomials (as $n \to \infty$). Furthermore, we numerically show that this convergence is rather quick and so the expressions can frequently be used, in many instances of finite-precision application, as the effective zeros of $H_n(x)$ with finite n, such as in applications of Gaussian quadrature. In a more aesthetic sense, these results also establish a beautiful correspondence between the boundaries of equal area partitions of circles with radii that are increasing in a certain manner and the Hermite polynomial zeros.

Spin systems are defined by the fundamental commutation relations between operators $\hat{S}^z$, $\hat{S}^+$ and $\hat{S}^-$:

$$\left[\hat{S}^z, \hat{S}^+\right] = \hat{S}^+, \quad \left[\hat{S}^z, \hat{S}^-\right] = \hat{S}^-, \quad \left[\hat{S}^+, \hat{S}^-\right] = 2\hat{S}^z. \tag{10.3}$$

Associating a spin with a boson $c^\dagger$, Holstein and Primakoff showed that to satisfy these commutation relations, the operators can be expressed as[103]

$$\hat{S}^z = \hat{c}^\dagger \hat{c} - S, \tag{10.4}$$

$$\hat{S}^+ = \hat{c}^\dagger \sqrt{2S - \hat{c}^\dagger \hat{c}}, \text{ and } \hat{S}^- = \sqrt{2S - \hat{c}^\dagger \hat{c}}\, \hat{c}. \tag{10.5}$$

This is a very useful association and has found many applications in the condensed matter field's study of many-body spin systems. Each boson excitation represents the "ladder up" finitesimal excitation away from the spin's extremal S state. The Hilbert space is finite-dimensional and possesses $2S + 1$ states $\{-S, -S + 1, \ldots, S\}$. In fact, considering eq. 10.5 it is clear that the Hilbert space outside this defined space is not even Hermitian.

Transforming from the Holstein-Primakoff bosonic representation to position (and its conjugate momentum) space (using the relations $c^\dagger = \frac{1}{\sqrt{2}}(\hat{q} - i\hat{p})$ and $c = \frac{1}{\sqrt{2}}(\hat{q} + i\hat{p})$) reveals that the trivial Hamiltonian is the harmonic oscillator: $\hat{H} = \hat{S}_z = \frac{1}{2}(\hat{q}^2 + \hat{p}^2) - (S + \frac{1}{2})$. Moreover, transformation of the $\hat{S}^+$ and $\hat{S}^-$ in eq. 10.5 reveals that the Hilbert space spans the domain $r^2 \equiv p^2 + q^2 \leq \sqrt{4S + 1}$. Just as in the S_z representation, $2S$ states all with the same area must exist within this domain. Figure 10.1 sketches out what they look like for the $\{S = \frac{1}{2}, S = 1, S = \frac{3}{2}\}$-spin systems.

Figure 10.1: The q-basis representation of a) $S = \frac{1}{2}$, b) $S = 1$ and c) $S = \frac{3}{2}$ systems is shown. The radius of the Hilbert space's domain is equal to $\sqrt{4S + 1}$ and so grows along with the number of allowed basis elements.

For a particular S-spin system, the lowest eigenstate must have the same sign at all q-basis elements since it must be nodeless. On the other hand, the highest eigenstate must have $n - 1$ nodes and so the q-basis elements must alternate in sign such that the eigenfunction passes through zero between them. This latter behavior is sketched in fig. 10.1 in red by the Hermite polynomial $H_n(x)$ denoting the value of the overlying q-basis element for the highest eigenstate.

For $S \to \infty$, the Hilbert space becomes infinite-dimensional and the Hamiltonian becomes that of the harmonic oscillator defined over $(p, q) \in \mathbb{R}^2$ with the associated eigenfunctions proportional to $e^{-\frac{x^2}{2}} H_n(x)$. It therefore follows that as $S \to \infty$, the boundaries of the q-basis elements become

the zeros of the Hermite polynomial $H_n(x)$ where $n = 2S$ since the highest eigenstate must still have alternating sign with each q-basis element.

Hermite polynomial zeros x_j are real and symmetric around $x = 0$. To determine these boundary points, the $2S$-dimensional Hilbert space's circular shape in position space can be exploited. For even $2S$, the area of the all the q-basis elements up until the jth boundary (measuring from the origin) is $\pi r^2 \frac{2j-1}{n+1}$. For odd $2S$, the area is $\pi r^2 \frac{2j}{n+1}$. This is illustrated in fig. 10.2.
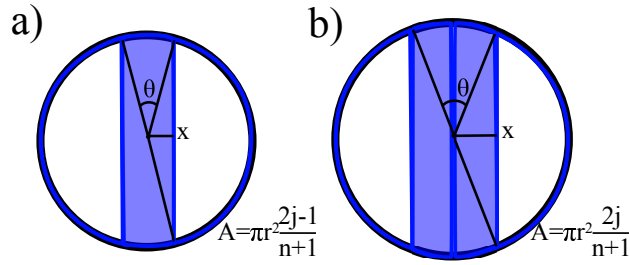

Figure 10.2: The area of the central a) $2j-1$ or b) $2j$ q-basis elements that approximately determine the jth zero of the Hermite polynomial $H_n(x)$ for n even and odd respectively is shaded in blue. The approximate jth zero is at the right boundary of these regions.

Using simple relations for the area of circle sectors and rectangles, it is possible to relate these q-basis element areas to x_j; The equation involving the approximate zeros of Hermite polynomials H_n with n even is:

$$\frac{(2j-1)\pi}{n+1} = \sin\theta + \theta, \tag{10.6}$$

while for odd n it is:

$$\frac{2j\pi}{n+1} = \sin\theta + \theta, \tag{10.7}$$

where $\theta = 2\sin^{-1}\frac{x_j}{r}$ and $r = \sqrt{2n+1}$.

Solving these equations for x_j yields the approximate jth zero for the nth Hermite polynomial. The results for the zeros of the first 50 Hermite polynomials are compared to the exact zeros in

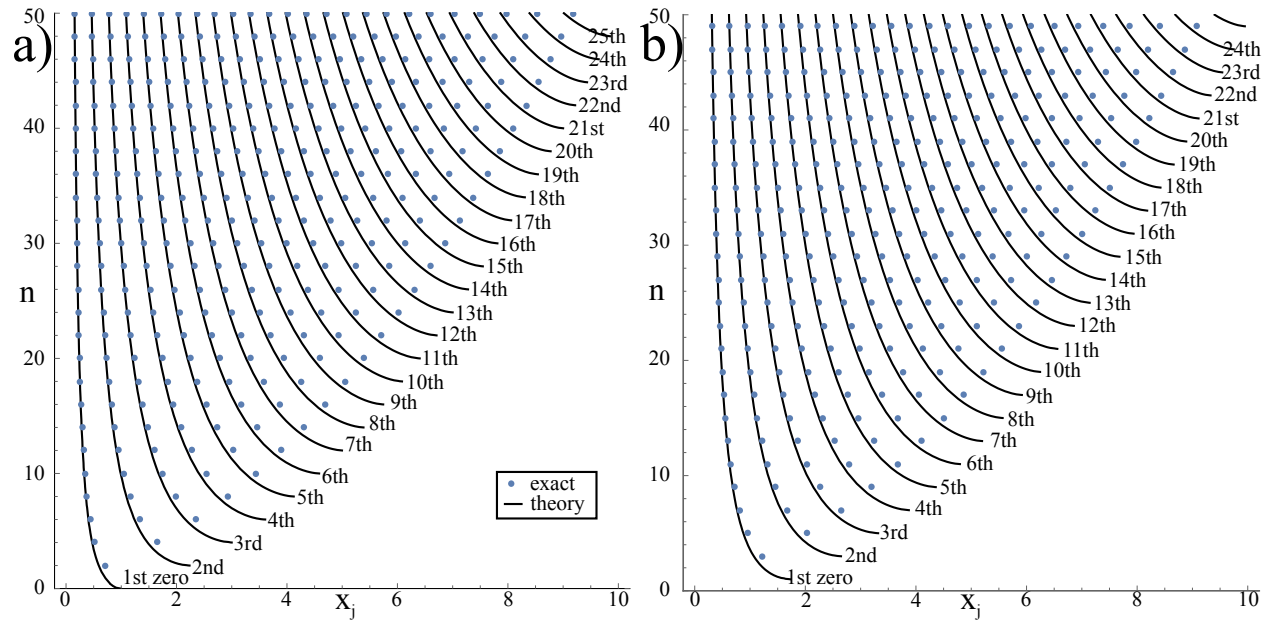fig. 10.3. In both cases, eqs. 10.6 and 10.7 converge to the zeros of the Hermite functions quite quickly[1].

Figure 10.3: Exact jth zeros of the Hermite polynomials $H_n(x)$ for n a) even and b) odd compared to those obtained from solving eqs. 10.6 and 10.7.

The finding that the boundaries of equal area partitions of growing circles correspond to the asymptotic zeros of the Hermite functions appears to be a novel one from a search of the literature. It is all the more surprising that the origin of this one-to-one correspondance stems from the Holstein-Primakoff representations for finite-dimensional spin systems. Furthermore, on a practical level, the apparently rapid convergence of these solutions suggests that they may be useful for more efficient determination of Hermite polynomial zeros for large-dimensional implementations of Gaussian quadrature.

---

[1]J. Katriel, through correspondence, showed that eqns 10.6 and 10.7 agree with the first asymptotic term from Dominici[101] for $n \to \infty$ for low j (not for maximal j). The latter result makes sense from the point of view that the maximal x_j is always close to the edge of the Hilbert space where the wavefunction goes to zero for any finite n whereas that of the harmonic oscillator decays forever. Eqs. 10.6 and 10.7 do not agree with higher order terms (w.r.t. $\frac{1}{n}$) in Dominici's asymptotic expansion.

10.2 Laguerre Polynomials

Associated Laguerre polynomials can be defined by the Rodrigues formula

$$L_n^{(\alpha)}(x) = \frac{x^{-\alpha}e^x}{n!} \frac{d^n}{dx^n}\left(e^{-x}x^{n+\alpha}\right),\tag{10.8}$$

and are solutions of the differential equation

$$xy'' + (\alpha + 1 - x)y' + ny = 0.\tag{10.9}$$

The Laguerre polynomials are proportional to the (appropriately scaled) eigenfunctions of the radial Hydrogen Hamiltonian as well as the 3d isotropic harmonic oscillator in position representation. They are also proportional to the eigenstates $e^{-\frac{x}{2}}x^{\frac{\alpha+1}{2}}L_{(E-2-2\alpha)/4}^{\alpha}(x)$ of:

$$x\left[-4\frac{d^2}{dx^2} + \left(1 + \frac{(\alpha-1)(\alpha+1)}{x^2}\right)\right],\tag{10.10}$$

with energies $\frac{E-2-2\alpha}{4}$ defined over $x \in (0,\infty)$ where $\hbar = m = 1$ (as adopted for the rest of the paper). This can be rewritten as the Hamiltonian

$$H = q\left[4p^2 + \left(1 + \frac{(\alpha-1)(\alpha+1)}{q^2}\right)\right],\tag{10.11}$$

where $E = 4N + 2 + 2\alpha$ for $N \in \mathbb{Z}^+$ in the quantum version.

We consider the simplest case, $\alpha = 1$, whose eigenfunctions in position space should be the associated Laguerre polynomials $L_{E/4-1}^{(1)}(q)$. The phase space picture of this Hamiltonian is shown in Figure 10.4.

We proceed in the same spirit as we did with the harmonic oscillator finite-dimensional Hilbert space in my recent communication[104]. The Hilbert space is symmetrical about $p = 0$ and energy is less than or equal to E when
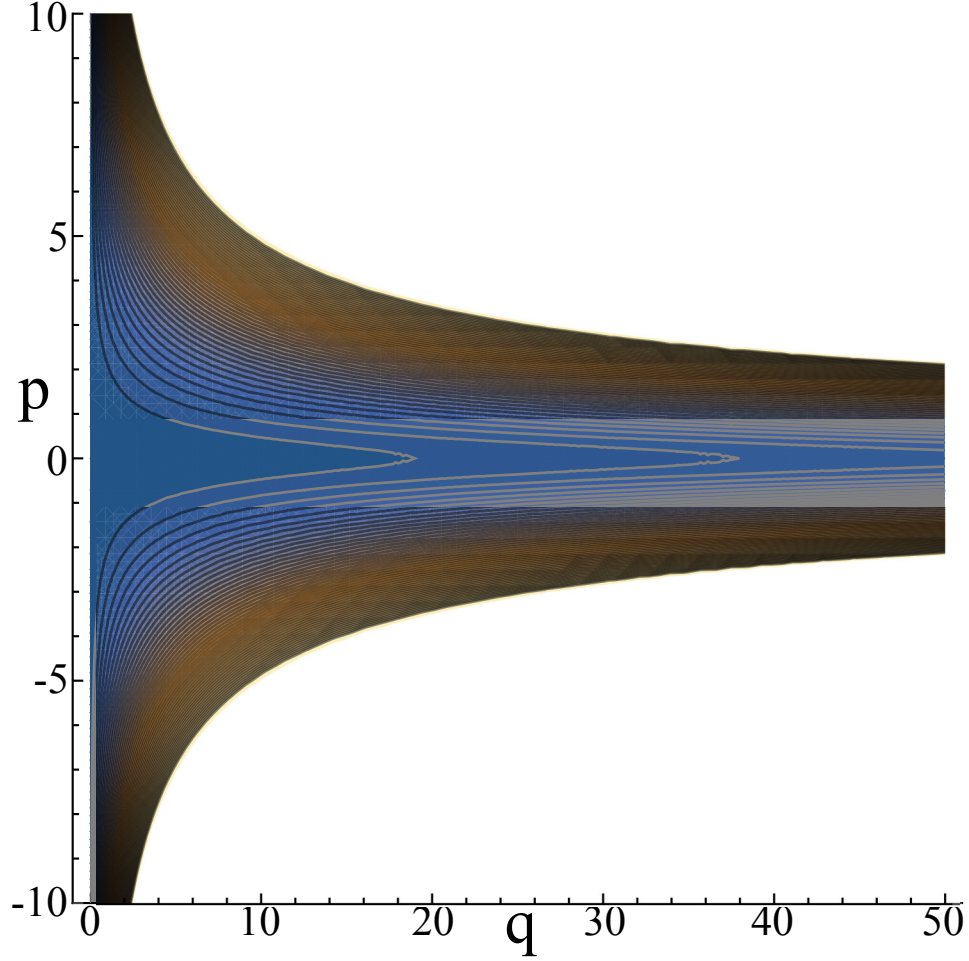
$$(1 + 4p^2)q \leq E.\tag{10.12}$$

Figure 10.4: The phase space of the Hamiltonian in eq. 10.11 with $\alpha = 1$. The contour lines correspond to isoenergy curves.

Moreover, at $p = 0$, the point in phase space with corresponding energy E is at $q = E$. It is thus simple to determine a system with dimension $N = \frac{E}{4} - 1$ has area $\frac{E\pi}{2} = 2(N+1)\pi$. The area within this region from $q = 0$ up to $q = x$ is

$$2\int_0^x \frac{\sqrt{E-q}}{2\sqrt{q}}dq = \sqrt{Ex\left(1 - \frac{x}{E}\right)} + E\sin^{-1}\left(\sqrt{\frac{x}{E}}\right). \tag{10.13}$$

Hence, for the jth root x_j,

$$2\pi j = \sqrt{N+1}\sqrt{x_j}\sqrt{4 - \frac{x_j}{N+1}} + 4(N+1)\sin^{-1}\left(\frac{\sqrt{x_j}}{\sqrt{4N+4}}\right), \tag{10.14}$$

which in the limit $N \to \infty$ is:

$$x_j = \left(\frac{\pi j}{2}\right)^2 \frac{1}{N}.$$ (10.15)

It is unclear if this agrees with any literature asymptotic value result.

The plot of eq 10.13 compared to the numerically calculated zeros is shown in Figure 10.5 and seems to converge near $q = 0$ as expected.
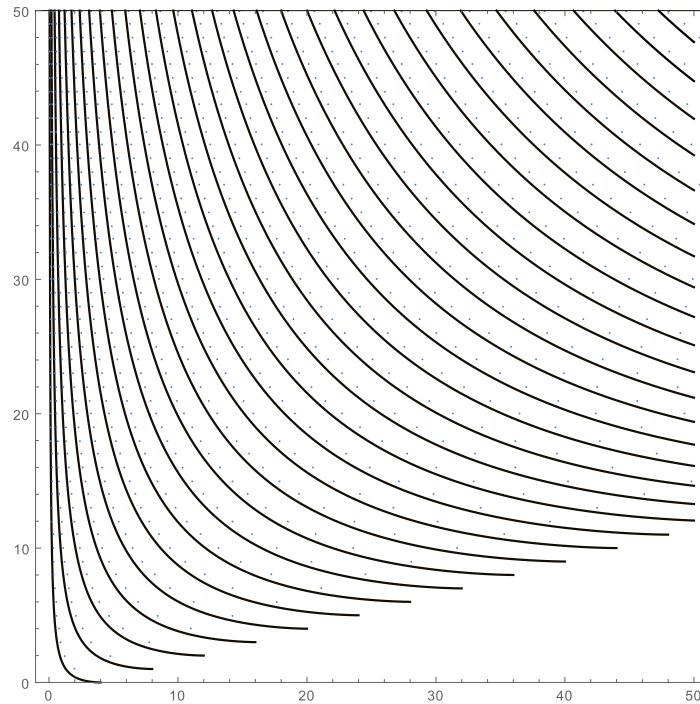

Figure 10.5: Eq. 10.13 compared to exact zeros of Laguerre polynomial $L^{(1)}_{E/4-1}(q)$.

Bibliography

[1] D.J. Tannor. *Introduction to Quantum Mechanics: A Time-dependent Perspective*. University Science Books, 2007.

[2] C Chester, B Friedman, and F Ursell. An extension of the method of steepest descents. In *Mathematical Proceedings of the Cambridge Philosophical Society*, volume 53, pages 599–611. Cambridge Univ Press, 1957.

[3] EJ Heller. Chaos and quantum physics. *Les Houches Summer School Session I, II*, 1991.

[4] Eric J. Heller. Time dependent approach to semiclassical dynamics. *The Journal of Chemical Physics*, 62(4):1544–1555, 1975.

[5] E.J. Heller. Time-dependent variational approach to semiclassical dynamics. *Journal of Chemical Physics*, 64:63, 1976.

[6] E. J. Heller. The semiclassical way to molecular spectroscopy. *Acc. Chem. Res.*, 14:368 – 375, 1981.

[7] Edward Kluk, Michael F. Herman, and Heidi L. Davis. Comparison of the propagation of semiclassical frozen gaussian wave functions with quantum propagation for a highly excited anharmonic oscillator. *The Journal of Chemical Physics*, 84(1):326–334, 1986.

[8] Eric J. Heller. Frozen gaussians: A very simple semiclassical approximation. *The Journal of Chemical Physics*, 75(6):2923–2931, 1981.

[9] Eric J. Heller. Cellular dynamics: A new semiclassical approach to time-dependent quantum mechanics. *The Journal of Chemical Physics*, 94(4):2723–2729, 1991.

[10] Haobin Wang, David E. Manolopoulos, and William H. Miller. Generalized filinov transformation of the semiclassical initial value representation. *The Journal of Chemical Physics*, 115(14):6317–6326, 2001.

[11] Steven Tomsovic and Eric J. Heller. Semiclassical dynamics of chaotic motion: Unexpected long-time accuracy. *Phys. Rev. Lett.*, 67:664–667, Aug 1991.

[12] I. M. Suarez Barnes, M. Nauenberg, M. Nockleby, and S. Tomsovic. Semiclassical theory of quantum propagation: The coulomb potential. *Phys. Rev. Lett.*, 71:1961–1964, Sep 1993.

[13] E. J. Heller. Guided gaussian wave packets. *Accounts of Chemical Research*, 39(2):127–134, 2006.

[14] William H Miller. An alternate derivation of the herman—kluk (coherent state) semiclassical initial value representation of the time evolution operator. *Molecular Physics*, 100(4):397–400, 2002.

[15] I M Suarez Barnes, M Nauenberg, M Nockleby, and S Tomsovic. Classical orbits and semiclassical wavepacket propagation in the coulomb potential. *Journal of Physics A: Mathematical and General*, 27(9):3299, 1994.

[16] Williams Thomas, Kelley Colin, and many others. Gnuplot 4.6: an interactive plotting program, September 2012.

[17] Harinder Pal, Manan Vyas, and Steven Tomsovic. Generalized gaussian wave packet dynamics: Integrable and chaotic systems. *Phys. Rev. E*, 93:012213, Jan 2016.

[18] R.P. Feynman and A.R. Hibbs. *Quantum Mechanics and Path Integrals: Emended Edition*. Dover Publications, Incorporated, 2012.

[19] L.S. Schulman. *Techniques and Applications of Path Integration*. Dover Books on Physics. Dover Publications, 2012.

[20] John H Van Vleck. The correspondence principle in the statistical interpretation of quantum mechanics. *Proceedings of the National Academy of Sciences of the United States of America*, 14(2):178, 1928.

[21] Cécile Morette. On the definition and approximation of feynman's path integrals. *Physical Review*, 81(5):848, 1951.

[22] Martin C Gutzwiller. Phase-integral approximation in momentum space and the bound states of an atom. *Journal of Mathematical Physics*, 8(10):1979–2000, 1967.

[23] IM Suarez Barnes, M Nauenberg, M Nockleby, and S Tomsovic. Semiclassical theory of quantum propagation: The coulomb potential. *Physical review letters*, 71(13):1961, 1993.

[24] Steven Tomsovic and Eric J Heller. Semiclassical dynamics of chaotic motion: unexpected long-time accuracy. *Physical review letters*, 67(6):664, 1991.

[25] Y Weissman. On the stationary phase evaluation of path integrals in the coherent states representation. *Journal of Physics A: Mathematical and General*, 16(12):2693, 1983.

[26] Michael F Herman and Edward Kluk. A semiclasical justification for the use of non-spreading wavepackets in dynamics calculations. *Chemical physics*, 91(1):27–34, 1984.

[27] John R Klauder. Path integrals and stationary-phase approximations. *Physical Review D*, 19(8):2349, 1979.

[28] Eric J Heller. Generalized theory of semiclassical amplitudes. *The Journal of Chemical Physics*, 66(12):5777–5785, 1977.

[29] Yitzhak Weissman. Semiclassical approximation in the coherent states representation. *The Journal of Chemical Physics*, 76(8):4067–4079, 1982.

[30] Michel Baranger, Marcus AM de Aguiar, Frank Keck, Hans-Jürgen Korsch, and Bernd Schellhaaß. Semiclassical approximations in phase space with coherent states. *Journal of Physics A: Mathematical and General*, 34(36):7227, 2001.

[31] Daniel Huber and Eric J Heller. Generalized gaussian wave packet dynamics. *The Journal of chemical physics*, 87(9):5302–5311, 1987.

[32] Daniel Huber, Eric J Heller, and Robert G Littlejohn. Generalized gaussian wave packet dynamics, schrödinger equation, and stationary phase approximation. *The Journal of chemical physics*, 89(4):2003–2014, 1988.

[33] Niels E Henriksen and Eric J Heller. Quantum dynamics for vibrational and rotational degrees of freedom using gaussian wave packets: Application to the three-dimensional photodissociation dynamics of icn. *The Journal of Chemical Physics*, 91(8):4700–4713, 1989.

[34] Marius Wehrle, Miroslav Šulc, and Jiří Vaníček. On-the-fly ab initio semiclassical dynamics: Identifying degrees of freedom essential for emission spectra of oligothiophenes. *The Journal of chemical physics*, 140(24):244114, 2014.

[35] Eric J Heller. Frozen gaussians: a very simple semiclassical approximation. *The Journal of Chemical Physics*, 75(6):2923–2931, 1981.

[36] Kenneth G Kay. Integral expressions for the semiclassical time-dependent propagator. *The Journal of chemical physics*, 100(6):4377–4392, 1994.

[37] Kenneth G Kay. Numerical study of semiclassical initial value methods for dynamics. *The Journal of chemical physics*, 100(6):4432–4445, 1994.

[38] Haobin Wang, David E. Manolopoulos, and William H. Miller. Generalized filinov transformation of the semiclassical initial value representation. *The Journal of Chemical Physics*, 115(14):6317–6326, 2001.

[39] Michael Spanner, Victor S Batista, and Paul Brumer. Is the filinov integral conditioning technique useful in semiclassical initial value representation methods? *The Journal of chemical physics*, 122(8):084111, 2005.

[40] Frank Grossmann and Ademir Luis Xavier Jr. From the coherent state path integral to a semiclassical initial value representation of the quantum mechanical propagator. *Physics Letters A*, 243(5):243–248, 1998.

[41] KP Huber and G Herzberg. *Constants of Diatomic Molecules*, volume 4. Van Nostrand Reinhold Co., 1979.

[42] P. Atkins and J. de Paula. *Physical Chemistry*. W. H. Freeman, 2002.

[43] IA Watson, BR Henry, and IG Ross. Local mode behavior: The morse oscillator model. *Spectrochimica Acta Part A: Molecular Spectroscopy*, 37(10):857–865, 1981.

[44] L Halonen and MS Child. Local mode vibrations in tetrahedral molecules. *Computer physics communications*, 51(1):173–193, 1988.

[45] L Halonen and MS Child. Model stretching overtone eigenvalues for sf6, wf6, and uf6. *The Journal of Chemical Physics*, 79(2):559–570, 1983.

[46] M. V. Berry. Quantum scars of classical closed orbits in phase space. *Proceedings of the Royal Society of London. A. Mathematical and Physical Sciences*, 423(1864):219–231, 1989.

[47] Shaul Mukamel. On the semiclassical calculation of molecular absorption and fluorescence spectra. *The Journal of Chemical Physics*, 77(1):173–181, 1982.

[48] Qiang Shi and Eitan Geva. A comparison between different semiclassical approximations for optical response functions in nonpolar liquid solutions. *The Journal of Chemical Physics*, 122(6):064506, 2005.

[49] Porscha L. McRobbie, Gabriel Hanna, Qiang Shi, and Eitan Geva. Signatures of nonequilibrium solvation dynamics on multidimensional spectra. *Accounts of Chemical Research*, 42(9):1299–1309, 2009. PMID: 19552404.

[50] Zhiming Li, Jian-Yun Fang, and Craig C. Martens. Simulation of ultrafast dynamics and pump–probe spectroscopy using classical trajectories. *The Journal of Chemical Physics*, 104(18):6919–6929, 1996.

[51] S. A. Egorov, Eran Rabani, and B. J. Berne. Vibronic spectra in condensed matter: A comparison of exact quantum mechanical and various semiclassical treatments for harmonic baths. *The Journal of Chemical Physics*, 108(4):1407–1422, 1998.

[52] S. A. Egorov, Eran Rabani, and B. J. Berne. Nonradiative relaxation processes in condensed phases: Quantum versus classical baths. *The Journal of Chemical Physics*, 110(11):5238–5248, 1999.

[53] Norah E. Shemetulskis and Roger F. Loring. Semiclassical theory of the photon echo: Application to polar fluids. *The Journal of Chemical Physics*, 97(2):1217–1226, 1992.

[54] J M Rost. Analytical total photo cross section for atoms. *Journal of Physics B: Atomic, Molecular and Optical Physics*, 28(19):L601, 1995.

[55] Jiří Vaníček and Eric J. Heller. Semiclassical evaluation of quantum fidelity. *Phys. Rev. E*, 68:056208, Nov 2003.

[56] Jiří Vaníček. Dephasing representation: Employing the shadowing theorem to calculate quantum correlation functions. *Phys. Rev. E*, 70:055201, Nov 2004.

[57] Jiří Vaníček. Dephasing representation of quantum fidelity for general pure and mixed states. *Phys. Rev. E*, 73:046204, Apr 2006.

[58] Cesare Mollica and Jiří Vaníček. Beating the efficiency of both quantum and classical simulations with a semiclassical method. *Physical Review Letters*, 107(21):214101, 2011.

[59] Eduardo Zambrano, Miroslav Sulc, and Jiri VaniCek. Improving the accuracy and efficiency of time-resolved electronic spectra calculations: Cellular dephasing representation with a prefactor. *The Journal of Chemical Physics*, 139(5):054109, 2013.

[60] Jiushu Shao and Nancy Makri. Forward–backward semiclassical dynamics without prefactors. *The Journal of Physical Chemistry A*, 103(39):7753–7756, 1999.

[61] Jiushu Shao and Nancy Makri. Forward–backward semiclassical dynamics with linear scaling. *The Journal of Physical Chemistry A*, 103(47):9479–9486, 1999.

[62] William H. Miller. Spiers memorial lecture quantum and semiclassical theory of chemical reaction rates. *Faraday Discuss.*, 110:1–21, 1998.

[63] Xiong Sun and William H. Miller. Forward–backward initial value representation for semiclassical time correlation functions. *The Journal of Chemical Physics*, 110(14):6635–6644, 1999.

[64] Jian Liu and William H. Miller. Using the thermal gaussian approximation for the boltzmann operator in semiclassical initial value time correlation functions. *The Journal of Chemical Physics*, 125(22):224104, 2006.

[65] Jian Liu and William H. Miller. Real time correlation function in a single phase space integral beyond the linearized semiclassical initial value representation. *The Journal of Chemical Physics*, 126(23):234110, 2007.

[66] Eduardo Zambrano and Alfredo M. Ozorio de Almeida. Initial-value representation for the loschmidt echo. *Phys. Rev. E*, 84:045201, Oct 2011.

[67] Miroslav Sulc, Henar Hernandez, Todd J. Martinez, and Jiri VaniCek. Relation of exact gaussian basis methods to the dephasing representation: Theory and application to time-resolved electronic spectra. *The Journal of Chemical Physics*, 139(3):034112, 2013.

[68] Kenneth G. Kay. Semiclassical propagation for multidimensional systems by an initial value method. *The Journal of Chemical Physics*, 101(3):2250–2260, 1994.

[69] Nicholas J. Wright and Nancy Makri. Forward–backward semiclassical dynamics for condensed phase time correlation functions. *The Journal of Chemical Physics*, 119(3):1634–1642, 2003.

[70] A.O. Caldeira and A.J. Leggett. Path integral approach to quantum brownian motion. *Physica A: Statistical Mechanics and its Applications*, 121(3):587 – 616, 1983.

[71] Christoph-Marian Goletz and Frank Grossmann. Decoherence and dissipation in a molecular system coupled to an environment: An application of semiclassical hybrid dynamics. *The Journal of Chemical Physics*, 130(24):244107, 2009.

[72] Haobin Wang, Michael Thoss, Kathy L. Sorge, Ricard Gelabert, Xavier Gimenez, and William H. Miller. Semiclassical description of quantum coherence effects and their quenching: A forward–backward initial value representation study. *The Journal of Chemical Physics*, 114(6):2562–2571, 2001.

[73] Yossi Elran and Paul Brumer. Decoherence in an anharmonic oscillator coupled to a thermal environment: A semiclassical forward-backward approach. *The Journal of Chemical Physics*, 121(6):2673–2684, 2004.

[74] Eric Jezek and Nancy Makri. Finite temperature correlation functions via forward−backward semiclassical dynamics†. *The Journal of Physical Chemistry A*, 105(12):2851–2857, 2001.

[75] Michael Thoss, Haobin Wang, and William H. Miller. Generalized forward–backward initial value representation for the calculation of correlation functions in complex systems. *The Journal of Chemical Physics*, 114(21):9220–9235, 2001.

[76] Prasanta Misra. *Physics of condensed matter*. Academic Press, 2011.

[77] Pedro Venezuela, Michele Lazzeri, and Francesco Mauri. Theory of double-resonant raman spectra in graphene: intensity and line shape of defect-induced and two-phonon bands. *Physical Review B*, 84(3):035433, 2011.

[78] Jun Yao, Yu Sun, Mei Yang, and Yixiang Duan. Chemistry, physics and biology of graphene-based nanomaterials: new horizons for sensing, imaging and medicine. *Journal of Materials Chemistry*, 22(29):14313–14329, 2012.

[79] Rasmita Sahoo and Rashmi Ranjan Mishra. Phonon dispersion of graphene revisited. *Journal of Experimental and Theoretical Physics*, 114(5):805–809, 2012.

[80] H Yanagisawa, T Tanaka, Y Ishida, M Matsue, E Rokuta, S Otani, and C Oshima. Analysis of phonons in graphene sheets by means of hreels measurement and ab initio calculation. *Surface and interface analysis*, 37(2):133–136, 2005.

[81] Zhiyun Li, M Jamal Deen, Shiva Kumar, and P Ravi Selvaganapathy. Raman spectroscopy for in-line water quality monitoring—instrumentation and potential. *Sensors*, 14(9):17275–17303, 2014.

[82] 4.4 la spettroscopia raman, 2016.

[83] Michael Donahue, Edita Botonjic-Sehic, David Wells, and Chris W Brown. Raman-understanding infrared and raman spectra of pharmaceutical polymorphs. *American Pharmaceutical Review*, 14(2):104, 2011.

[84] Jill Hochlowski, David Whittern, Jeff Pan, and Rolf Swenson. Applications of raman spectroscopy to combinatorial chemistry. *Drugs of the Future*, 24(5):539, 1999.

[85] Kin Fai Mak, Long Ju, Feng Wang, and Tony F Heinz. Optical spectroscopy of graphene: from the far infrared to the ultraviolet. *Solid State Communications*, 152(15):1341–1349, 2012.

[86] V Coropceanu, JM André, M Malagoli, and JL Brédas. The role of vibronic interactions on intramolecular and intermolecular electron transfer in π-conjugated oligomers. *Theoretical Chemistry Accounts*, 110(2):59–69, 2003.

[87] Zheng Yan and Andrew R. Barron. Raman spectrum of graphene, 2016.

[88] S Bernard, E Whiteway, V Yu, DG Austing, and M Hilke. Probing the experimental phonon dispersion of graphene using 12 c and 13 c isotopes. *Physical Review B*, 86(8):085409, 2012.

[89] Stephanie Reich, Janina Maultzsch, Christian Thomsen, and Pablo Ordejon. Tight-binding description of graphene. *Physical Review B*, 66(3):035412, 2002.

[90] Robert John Nemanich and SA Solin. First-and second-order raman scattering from finite-size crystals of graphite. *Physical Review B*, 20(2):392, 1979.

[91] RP Vidano, DB Fischbach, LJ Willis, and TM Loehr. Observation of raman band shifting with excitation wavelength for carbons and graphites. *Solid State Communications*, 39(2):341–344, 1981.

[92] Istvan Pócsik, Martin Hundhausen, Margit Koós, and Lothar Ley. Origin of the d peak in the raman spectrum of microcrystalline graphite. *Journal of Non-Crystalline Solids*, 227:1083–1086, 1998.

[93] C Thomsen and S Reich. Double resonant raman scattering in graphite. *Physical Review Letters*, 85(24):5214, 2000.

[94] RM Martin and LM Falicov. Resonant raman scattering. In *Light scattering in Solids I*, pages 79–145. Springer, 1983.

[95] J Kürti, V Zólyomi, A Grüneis, and H Kuzmany. Double resonant raman phenomena enhanced by van hove singularities in single-wall carbon nanotubes. *Physical Review B*, 65(16):165433, 2002.

[96] Paul G Nevai and Jesús S Dehesa. On asymptotic average properties of zeros of orthogonal polynomials. *SIAM Journal on Mathematical Analysis*, 10(6):1184–1192, 1979.

[97] Joseph L Ullman et al. Orthogonal polynomials associated with an infinite interval. *The Michigan Mathematical Journal*, 27(3):353–363, 1980.

[98] HN Mhaskar and EB Saff. Extremal problems for polynomials with exponential weights. *Transactions of the American Mathematical Society*, 285(1):203–234, 1984.

[99] Andrei Aleksandrovich Gonchar and Evguenii Andreevich Rakhmanov. Equilibrium measure and the distribution of zeros of extremal polynomials. *Sbornik: Mathematics*, 53(1):119–130, 1986.

[100] Wolfgang Gawronski. On the asymptotic distribution of the zeros of hermite, laguerre, and jonquiere polynomials. *Journal of approximation theory*, 50(3):214–231, 1987.

[101] Diego Dominici. Asymptotic analysis of the hermite polynomials from their differential–difference equation. *Journal of Difference Equations and Applications*, 13(12):1115–1128, 2007.

[102] Arpad Elbert and Martin E Muldoon. Approximations for zeros of hermite functions. *Contemporary Mathematics*, 471:117–126, 2008.

[103] T. Holstein and H. Primakoff. Field dependence of the intrinsic domain magnetization of a ferromagnet. *Phys. Rev.*, 58:1098–1113, Dec 1940.

[104] Lucas Kocia. Asymptotic equation for zeros of hermite polynomials from the holstein-primakoff representation. *arXiv preprint arXiv:1506.00541*, 2015.

[105] Michael Spanner, Victor S. Batista, and Paul Brumer. Is the filinov integral conditioning technique useful in semiclassical initial value representation methods? *The Journal of Chemical Physics*, 122(8):–, 2005.

[106] Manuscript in preparation.

[107] M. Šulc, H. Hernández, T. J. Martínez, and J. Vaníček. "Relation of exact Gaussian basis methods to the dephasing representation: Theory and application to time-resolved electronic spectra". June 2013.

[108] Jörg Tatchen and Eli Pollak. Semiclassical on-the-fly computation of the s0→ s1 absorption spectrum of formaldehyde. *The Journal of chemical physics*, 130(4):041103, 2009.

[109] E. Zambrano, M. Sulc, and J. Vanicek. Improving the accuracy and efficiency of time-resolved electronic spectra calculations: Cellular dephasing representation with a prefactor. June 2013.

[110] Cesare Mollica, Tomáš Zimmermann, and Jiří Vaníček. Efficient sampling avoids the exponential wall in classical simulations of fidelity. *Phys. Rev. E*, 84:066205, Dec 2011.

[111] Lucas Kocia and Eric J Heller. Communication: Hk propagator uniformized along a one-dimensional manifold in weakly anharmonic systems. *The Journal of chemical physics*, 141(18):181102, 2014.

[112] Sybil M Anderson, Daniel Neuhauser, and Roi Baer. Trajectory-dependent cellularized frozen gaussians, a new approach for semiclassical dynamics: Theory and application to he–naphtalene eigenvalues. *The Journal of chemical physics*, 118(20):9103–9108, 2003.

[113] Zhe-xian Wang and Eric J Heller. Semiclassical investigation of the revival phenomena in a one-dimensional system. *Journal of Physics A: Mathematical and Theoretical*, 42(28):285304, 2009.

[114] Kenneth G Kay. Semiclassical propagation for multidimensional systems by an initial value method. *The Journal of chemical physics*, 101(3):2250–2260, 1994.